NASA CR-144784

WIDEBAND 1.064 MICROMETER DETECTOR EVALUATION

(NASA-CR-144784) WIDEBAND 1.064 MICROMETER DETECTOR EVALUATION Final Report (McDonnell-Douglas Astronautics Co.) 151 p HC $6.75 CSCL 14B

N76-27539

Unclas G3/35 46616

S. I. Green

MCDONNELL DOUGLAS ASTRONAUTICS COMPANY - EAST
P.O. BOX 516
ST. LOUIS, MISSOURI 63166

SEPTEMBER 1975

FINAL REPORT

NAS5-20616

Prepared For:

Goddard Space Flight Center
Greenbelt, Maryland 20771

THIS REPORT WAS PREPARED BY MCDONNELL DOUGLAS ASTRONAUTICS COMPANY-EAST, ST. LOUIS, MISSOURI UNDER CONTRACT NUMBER NAS5-20616.

TABLE OF CONTENTS

		Page
1.	INTRODUCTION AND PROGRAM SUMMARY	1
2.	RCA REACH-THROUGH SILICON AVALANCHE PHOTODIODE	5
	2.1 Description	5
	2.2 Bit Error Rate Tests	6
	2.3 Unit Tests	11
	2.3.1 Single Wafer Detector F1	11
	2.3.2 Single Wafer Detector F2	15
	2.3.3 Dual Wafer Detector DF1	24
	2.3.4 Dual Wafer Detector DF2	24
	2.3.5 Heated Detector HF2	34
	2.3.6 Heated Detector HF3	34
	2.4 Discussion of Performance	44
3.	VARIAN PHOTOMULTIPLIER	52
	3.1 Description	52
	3.2 Bit Error Rate Tests	53
	3.3 Unit Tests	58
	3.3.1 Five Stage Photomultiplier S/N 027	58
	3.3.2 Five Stage Photomultiplier S/N 028	58
	3.3.3 Six Stage Photomultiplier S/N 029	64
	3.3.4 Six Stage Photomultiplier S/N 031	64
	3.3.5 Six Stage Photomultiplier S/N 035	68
	3.4 Noise Measurements	68
	3.4.1 S/N 031 Signal Induced Noise	73
	3.4.2 S/N 035 Signal Induced Noise	73
	3.5 Discussion of Performance	78
4.	ROCKWELL HYBRID DETECTOR	79
	4.1 Description	79
	4.2 Bit Error Rate Tests	80
	4.3 Unit Tests	85
	4.3.1 GaAsSb APD M15-7	85
	4.3.2 Hybrid Detector M-4	92
	4.3.3 Hybrid Detector M-5	92
	4.3.4 Hybrid Detector M-7a	102
	4.3.5 Hybrid Detector M-7b	107
	4.3.6 Hybrid Detector M-8a	107
	4.3.7 Hybrid Detector M-8b	107

TABLE OF CONTENTS (Continued)

		Page
4.4	Discussion of Performance	113
4.4.1	Avalanche Current Gain	113
4.4.2	MESFET 1/f Noise	113
4.4.3	Gain and Bandwidth	115
4.4.4	Comparison with Expected Results	115
5.	BIT ERROR RATE TESTING	117
5.1	Measurement Equipment	117
5.2	Measurement Procedure	125
6.	UNIT TESTING	127
6.1	Dark Current	127
6.2	Scanning	127
6.3	Output Waveforms	129
6.4	Noise Equivalent Input Power	130
6.5	Noise Equivalent Input Power Versus Photocurrent	134
6.5.1	RCA Avalanche Photodiodes	134
6.5.2	Varian Photomultipliers	141

LIST OF FIGURES

Figure No.	Title	Page
1	Best Communication System Bit Error Rate Data	4
2	RCA Silicon APD Bit Error Rate Data	9
3	Heated Silicon APD Bit Error Rate Data	10
4	RCA Silicon APD F1 Current-Voltage Characteristics	12
5A	RCA Silicon APD F1 1.064 μm Photoresponse Scans	13
5B	RCA Silicon APD F1 1.064 μm Photoresponse Scans	14
6	RCA Silicon APD F1 Output Waveform	16
7	RCA Silicon APD F1 Impulse Response	17
8	RCA Silicon APD F2 Noise Equivalent Input Power	18
9	RCA Silicon APD F2 Current-Voltage Characteristics	19
10A	RCA Silicon APD F2 1.064 μm Photoresponse Scans	20
10B	RCA Silicon APD F2 1.064 μm Photoresponse Scans	21
11	RCA Silicon APD F2 Output Waveform	22
12	RCA Silicon APD F2 Impulse Response	23
13	RCA Silicon APD F2 Noise Equivalent Input Power	25
14	RCA Silicon APD DF1 Current-Voltage Characteristics	26
15A	RCA Silicon APD DF1 1.064 μm Photoresponse Scans	27
15B	RCA Silicon APD DF1 1.064 μm Photoresponse Scans	28
16	RCA Silicon APD DF1 Output Waveform	29
17	RCA Silicon APD DF1 Impulse Response	30
18	RCA Silicon APD DF1 Noise Equivalent Input Power	31
19	RCA Silicon APD DF2 Current-Voltage Characteristics	32
20	RCA Silicon APD DF2 1.064 μm Photoresponse Scans	33
21	RCA Silicon APD DF2 Output Waveform	35
22	RCA Silicon APD DF2 Impulse Response	36
23	RCA Silicon APD DF2 Noise Equivalent Input Power	37
24	RCA Silicon APD HF2 Current-Voltage Characteristics	38
25	RCA Silicon APD HF2 1.064 μm Photoresponse Scans	39
26	RCA Silicon APD HF2 Output Waveform	40
27	RCA Silicon APD HF2 Impulse Response	41
28	RCA Silicon APD HF2 Noise Equivalent Input Power	42
29	RCA Silicon APD HF3 Current-Voltage Characteristics	43
30A	RCA Silicon APD HF3 1.064 μm Photoresponse Scans	45
30B	RCA Silicon APD HF3 1.064 μm Photoresponse Scans	46
31	RCA Silicon APD HF3 Output Waveform	47
32	RCA Silicon APD HF3 Impulse Response	48
33	RCA Silicon APD HF3 Noise Equivalent Input Power	49
34	VPM 152A Operation with External Divider	54
35	VPM 152A Bit Error Rate Data	56
36	VPM 152A S/N 031 Bit Error Rate Data	57
37	VPM 152A S/N 035 Bit Error Rate Data	59
38	APM 152A Gain Reduction with Dynode 1 Potential	60
39	VPM 152A S/N035 Bit Error Rate Data	61
40	VPM 152A S/N027 Output Waveforms	62
41	VPM 152A S/N028 1.064 μm Photoresponse Scans	63
42	VPM 152A S/N028 Output Waveforms	65
43	VPM 152A S/N029 Output Waveforms	66
44	VPM 152A S/N 031 1.064 μm Photoresponse Scans	67
45	VPM 152A S/N031 Waveform Showing Signal Induced Noise at High Gain	69
46	VPM 152 S/N 031 Impulse Response	70

LIST OF FIGURES (Continued)

Figure No.	Title	Page
47	VPM 152A S/N035 1.064 μm Photoresponse Scans	71
48	VPM 152A S/N035 Waveform (Inverted)	72
49	Signal Induced Noise Pulse Measurement Setup	74
50	VPM 152A S/N 031 Signal Induced Noise Pulse Profile	75
51	VPM 152A S/N 031 Noise Pulse Delay	76
52	VPM 152A S/N 035 Signal Induced Noise Pulse Profile	77
53	Rockwell Hybrid Detector Unity Gain Bit Error Rate Data	83
54	Rockwell Hybrid Detector Optimum Gain Bit Error Rate Data	84
55	Rockwell Hybrid Detector M-7b Bit Error Rate Data	86
56	Rockwell GaAsSb APD M15-7 Dark Current	87
57A	Rockwell GaAsSb APD M15-7 Photoresponse Scans	88
57B	Rockwell GaAsSb APD M15-7 Photoresponse Scans	89
58	Rockwell GaAsSb M15-7 Impulse Response	90
59	Rockwell GaAsSb APD M15-7 Waveforms	91
60	Rockwell GaAsSb APD M15-7 Noise Equivalent Input Power	93
61	Rockwell Hybrid Detector M-4 APD Dark Current	94
62A	Rockwell Hybrid Detector M-4 Photoresponse Scans	95
62B	Rockwell Hybrid Preamp M-4 Photoresponse Scans	96
63	Rockwell Hybrid Detector M-4 Output Waveform	97
64	Rockwell Hybrid Detector M-4 Impulse Response	98
65	Rockwell Hybrid Detector M-4 Noise Equivalent Input Power	99
66	Rockwell Hybrid Detector M-5 APD Dark Current	100
67	Rockwell Hybrid Detector M-5 Photoresponse Scans	101
68	Rockwell Hybrid Detector M-5 Output Waveform	103
69	Rockwell Hybrid Detector M-5 Impulse Response	103
70	Rockwell Hybrid Detector M-5 Noise Equivalent Input Power	104
71	Rockwell Hybrid Detector M-7a Photoresponse Scans	105
72	Rockwell Hybrid Detector M-7a Output Waveform	106
73	Rockwell Hybrid Detector M-7b Dark Current	108
74	Rockwell Hybrid Detector M-7b Photoresponse Scans	109
75	Rockwell Hybrid Detector M-7b Impulse Response	110
76	Rockwell Hybrid Detector M-7b Noise Equivalent Input Power	111
77	Rockwell Hybrid Detector M-8a Output Waveform	112
78	Rockwell Hybrid Detector M-8a Impulse Response	112
79	Rockwell Hybrid Detector M-7b Noise Spectrum	114
80	Communication System	118
81	63 Bit 400 Mbps PGBM Transmitter Waveform	119
82	Receiver and Error Measurement System	120
83	Gated High Speed Threshold Detector Circuit	122
84	Photoresponde Scanner	128
85	Reference Impulse Signal for Response Measurements	131
86	1.064 μm Noise Equivalent Input Power Measurement	133
87	RCA Silicon APD F1 NEIP Versus Background Photocurrent	135
88	RCA Silicon APD F2 NEIP Versus Background Photocurrent	136
89	RCA Silicon APD DF1 NEIP Versus Background Photocurrent	137
90	RCA Silicon APD DF2 NEIP Versus Background Photocurrent	138
91	RCA Silicon APD HF2 NEIP Versus Background Photocurrent	139
92	RCA Silicon APD HF3 NEIP Versus Background Photocurrent	140
93	VPM 152A S/N 028 NEIP Versus Background Photocurrent	142
94	VPM 152A S/N 031 NEIP Versus Background Photocurrent	143
95	VPM 152A S/N 035 NEIP Versus Background Photocurrent	144

LIST OF TABLES

Table No.	Title	Page
I	GFE Detectors	2
II	Summary of Best 400 Mbps PGBM Communication System Test Results	3
III	RCA Silicon APD Manufacturer Data	7
IV	RCA Silicon APD 400 Mbps PGBM Communication System Test Results	8
V	RCA Silicon APD Detector Performance Comparison	50
VI	Varian LSE VPM 152A Manufacturer Data	53
VII	Varian VPM 152A 400 Mbps PGBM Communication System Test Results	54
VIII	Rockwell Hybrid Detector Manufacturer Data	81
IX	Rockwell Detector 400 Mbps PGBM Communication System Test Results	82
X	Rockwell Hybrid Detector Unity Gain Performance Comparison	116

1. INTRODUCTION AND PROGRAM SUMMARY

The purpose of this program was to evaluate the performance of several candidate detectors for use as communications detectors in a 400 Mbps 1.064 μm laser communication system. The detector types supplied as GFE by NASA/GSFC, included:

a) The RCA (Montreal) silicon avalanche photodiode with a reach through structure.
b) The Varian LSE electrostatic photomultiplier.
c) The Rockwell International hybrid detector with gallium arsenide antimonide avalanche photodiode and integral transresistance preamplifier.

For each detector type, characterization testing included:

a) Scans of cathode photoresponse uniformity.
b) Photograph of output waveform showing response time.
c) Measurement of dark current.
d) Measurement of noise equivalent input power.
e) Measurement of bit error rate performance in a 400 Mbps Pulse Gated Binary Modulation (PGBM) laser communication system test bed.

The measurement of communication system bit error rate (BER) performance is the ultimate measure of detector capability in communication applications. The results of communication system BER testing for the best detector of each type are summarized in the remainder of this section. Complete testing data of each type detector is presented in Sections 2, 3, and 4. The 400 Mbps 1.064 μm communication system receiver test bed is described in Section 5. The remaining unit testing procedures are described in Section 6.

A list of the GFE detectors tested during this program and the designation code for each used throughout this report is shown in Table I.

The best communication system results for each detector type are summarized in Table II. Performance comparisons are made at 10^{-6} BER, the specification level chosen for satellite laser communication links. The

TABLE I

GFE Detectors

Manufacturer	Model	Designation	Type
RCA (Montreal)	C30817	F1	Single Wafer Si APD
	(Modified)	F2	Single Wafer Si APD
		DF1	Dual Wafer Si APD
		DF2	Dual Wafer Si APD
		HF2	Heated Single Wafer Si APD
		HF3	Heated Single Wafer Si APD
Varian LSE	VPM 152A	S/N 027	5 Stage Electrostatic PMT
		S/N 028	5 Stage Electrostatic PMT
		S/N 029	6 Stage Electrostatic PMT
		S/N 031	6 Stage Electrostatic PMT
		S/N 035	6 Stage Electrostatic PMT
Rockwell Int.		M15-7	GaAsSb APD
(Science Center)	Mark IA	M-4	GaAsSb APD and Hybrid Preamp
	Mark IA	M-5	GaAsSb APD and Hybrid Preamp
	Mark II	M-7	GaAsSb APD and Hybrid Preamp
	Mark III	M-8	GaAsSb APD and Hybrid Preamp

data is presented in two groups. The first indicates the best performance levels that can be expected in normal space laser communication system operation. The second cites the best performance levels which can be achieved by focusing the signal to diffraction limited spots on the photosensitive area. The complete BER curves are presented in Figure 1. Although very good performance can be achieved by using a very small spot, these latter measurements would not be achievable under realistic system constraints.* The best full area performance with the Rockwell detectors with optimum gain probably lies midway between the unity gain results and the focused spot results. However, these latter figures indicate possible future capability with improvements in device materials and technology.

TABLE II

SUMMARY OF BEST 400 Mbps PGBM COMMUNICATION SYSTEM TEST RESULTS

DETECTOR	FOR 10^{-6} BIT ERROR RATE		COMMENTS
	1.064 μm Power	Photons/Pulse	
	BEST NORMAL OPERATION		
RCA DF2	100 nW	2675	gain = 100
Varian S/N 035	213 nW	5704	-20°C gain = 1040
Rockwell M-7A	199 nW	5324	unity gain
	BEST SMALL FOCUSED SPOT		
RCA DF2	59 nW	1581	gain = 100 lens 16 mm f8
Rockwell M-5	57 nW	1537	bias 115.1 V lens 16 mm f3.2

* The requirement of diffraction limited optics seriously impacts the weight and cost of the system. A substantial improvement in pointing and tracking accuracy is also required.

FIGURE 1 BEST COMMUNICATION SYSTEM BIT ERROR RATE DATA

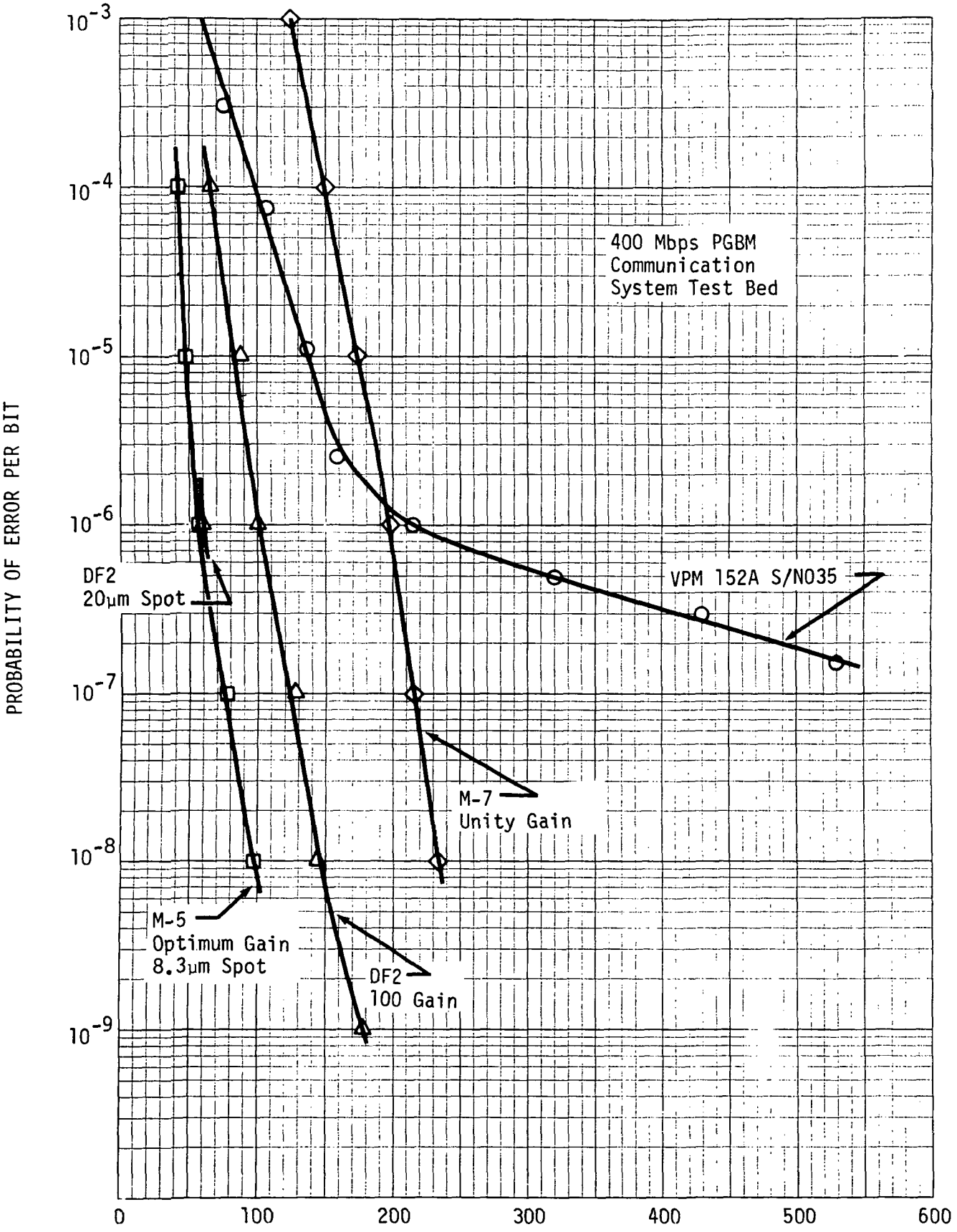

2. RCA REACH-THROUGH SILICON AVALANCHE PHOTODIODE

2.1 DESCRIPTION

The Silicon Avalanche Photodiode (APD) fabricated by RCA (Montreal) has a reach through structure[1] which separates the depletion region into a wide drift region where photons are absorbed and a narrow region where avalanche multiplication occurs. Quantum efficiency of these devices is proportional to device thickness since silicon becomes nearly transparent at 1.064 μm. Absorbtivity is only 13 cm^{-1}. Speed of these devices is not limited by RC risetime. It is limited by the transit time of carriers through the depletion region, which is virtually the full thickness of the wafer. Thus speed of response is directly traded off against quantum efficiency. In order to achieve the speed required for 400 Mbps, these devices were made 75 μm thick compared to the standard RCA product (C30817) which is 100 μm thick and has correspondingly higher quantum efficiency.

The RCA detectors were fabricated in three configurations, and two samples of each type were furnished for evaluation.

Two devices, designated F1 and F2, were each 75 μm thick diodes with 1 mm circular apertures. The rear surface of the diode wafer was mirrored (80% reflection) so that the input optical signal made a double pass through the diode wafer to maximize quantum efficiency. The quantum efficiency of these devices was estimated at 15.5%, and they operated at a gain of ∿300 with applied biases of -413V and -436V respectively.

Two devices, designated DF1 and DF2, were each made with two diode wafers optically in cascade and electrically in parallel. Since speed of response was limited by the transit time rather than the RC product, the speed of these devices was essentially the same as that of the single diode wafer detectors. The rear surface of the rear diode was mirrored so that optical signal passed

[1] P. P. Webb, R. J. McIntyre, J. Conradi, "Properties of Avalanche Photodiodes," RCA Review, Vol. 35, June 1974.

through both wafers in each direction to maximize absorption. The quantum efficiency of these dual devices was estimated at 25.6%. Current gain of ∿200 was achieved at -396V and -409V respectively.

Two devices, designated HF2 and HF3, were single diode detectors with heater and temperature regulator circuitry on the back side of the ceramic substrate to which the diode wafer was affixed. These detectors are identical to F1 and F2 with the exception of the heater. Operation at an elevated temperature of 80°C shifted the energy band edge in silicon which increased the absorption and therefore the quantum efficiency. Estimated quantum efficiency of these detectors rose from 15.5% at room temperature to 25.6% at 80°C. Current gain of ∿300 was achieved at -445V and -440V respectively. Avalanche breakdown potential and dark current were both higher than at room temperature.

A compilation of data provided by the manufacturer appears in Table III. The surface leakage component of the dark current was not multiplied and increased proportionally with applied bias voltage. The bulk leakage component of the dark current was multiplied by avalanche gain and increased rapidly with bias at high gain. Multiplied bulk current was the dominant contribution to detector noise. Photocurrent could not be measured directly with this diode structure, since photoresponse ceased with decreasing bias while avalanche gain was relatively high. The QE figures cited are manufacturer's estimates based on the performance of PIN diodes made with the same material and dimensions.

2.2 BIT ERROR RATE TESTS

Communication system bit error rate test data for the RCA detectors is summarized in Table IV. Measured responsivity varies widely about the predicted values. This is possibly due to a change in quantum efficiency with position due to interference effects between the faces of the silicon wafer. The bit error rate curves for all six detectors in normal operation are shown in Figure 2. When the optical input signal was focused to a very small spot on the best detector, a 2.3 dB improvement was observed. Only the data point at 10^{-6} BER was taken. The bit error rate curves for the heated detectors are shown in Figure 3 for operation at room temperature and at 80°C.

TABLE III

RCA SILICON APD MANUFACTURER DATA

Diode	Temperature	QE	Voltage	Responsivity	Surface Dark Current	Bulk Dark Current	Gain	QE
F1	23°C	15.5%	-413V	40 A/W	95 nA	<118 pA	300	15.5%
F2	23°C	15.5%	-436V	40 A/W	165 nA	<55 pA	300	15.5%
DF1	23°C	25.6%	-396V	44 A/W	195 nA	<350 pA	200	25.6%
DF2	23°C	25.6%	-409V	44 A/W	200 nA	<315 pA	200	25.6%
HF2	80°C	25.6%	-445V	66 A/W	4.15 μA	<1.5 nA	300	25.6%
HF3	80°C	25.6%	-440V	66 A/W	4.12 μA	<0.76 nA	300	25.6%

Of the detector types tested, the RCA detectors were the simplest to use beacuse they had a large active area and relatively uniform performance. Avalanche gain changed slowly and controllably with diode bias up to maximum gain. For best operation, several shielding beads were slipped onto the detector bias lead to eliminate the pick-up of interfering signals. A 1 dB to 3 dB improvement in communication system performance was achieved in this manner.

Detector DF2 was the best overall detector seen on this program. All of the RCA detectors had sufficient gain to overcome preamplifier noise. This was determined by adding a 6 dB attenuator pad between the detector and the preamplifier in addition to the 2 dB pad which served as a broadband dc path. An additional 0.8 dB of optical input signal power was typically required to restore the same system BER performance. If the detection performance had been amplifier noise limited, a full 3 dB increase in input signal power would have been required to compensate for the loss of the 6 dB pad.

TABLE IV

RCA SILICON APD 400 Mbps PGBM COMMUNICATION SYSTEM TEST RESULTS

DETECTOR	QE	FOR 10^{-6} BIT ERROR RATE			MEASUREMENT CONDITIONS			COMMENTS
		1.064 μm	PHOTONS PER PULSE	PHOTOELECTRONS PER PULSE	DIODE SIGNAL CURRENT	BIAS VOLTAGE	RESPONSIVITY	
F1	*15.5%	169 nW	4521	701	5.5 μA	-413V	32.6 A/W	
F2	*15.5%	160 nW	4288	665	10.0 μA	-436	62.5	
DF1	*25.6%	105 nW	2807	718	10.3 μA	-395	98.3	
DF2	*25.6%	100 nW	2675	684	4.0 μA	-400	40.0	
		59 nW	1581	404	3.3 μA	-400	55.9	Best Focused Spot
HF2	*25.6%	137 nW	3664	937	7.0 μA	-438	51.2	4.0 μA Leakage @ +80°C
	*15.5%	180 nW	4831	749	4.7 μA	-356	26.1	23°C
HF3	*25.6%	116 nW	3117	797	5.9 μA	-432	50.7	3.4 μA Leakage @ +80°C
	*15.5%	198 nW	5305	822	6.9 μA	-341	34.9	23°C

* Estimated by manufacturer based on measurements of PIN diodes made with the same material and dimensions as the APD units.

FIGURE 2 RCA SILICON APD BIT ERROR RATE DATA

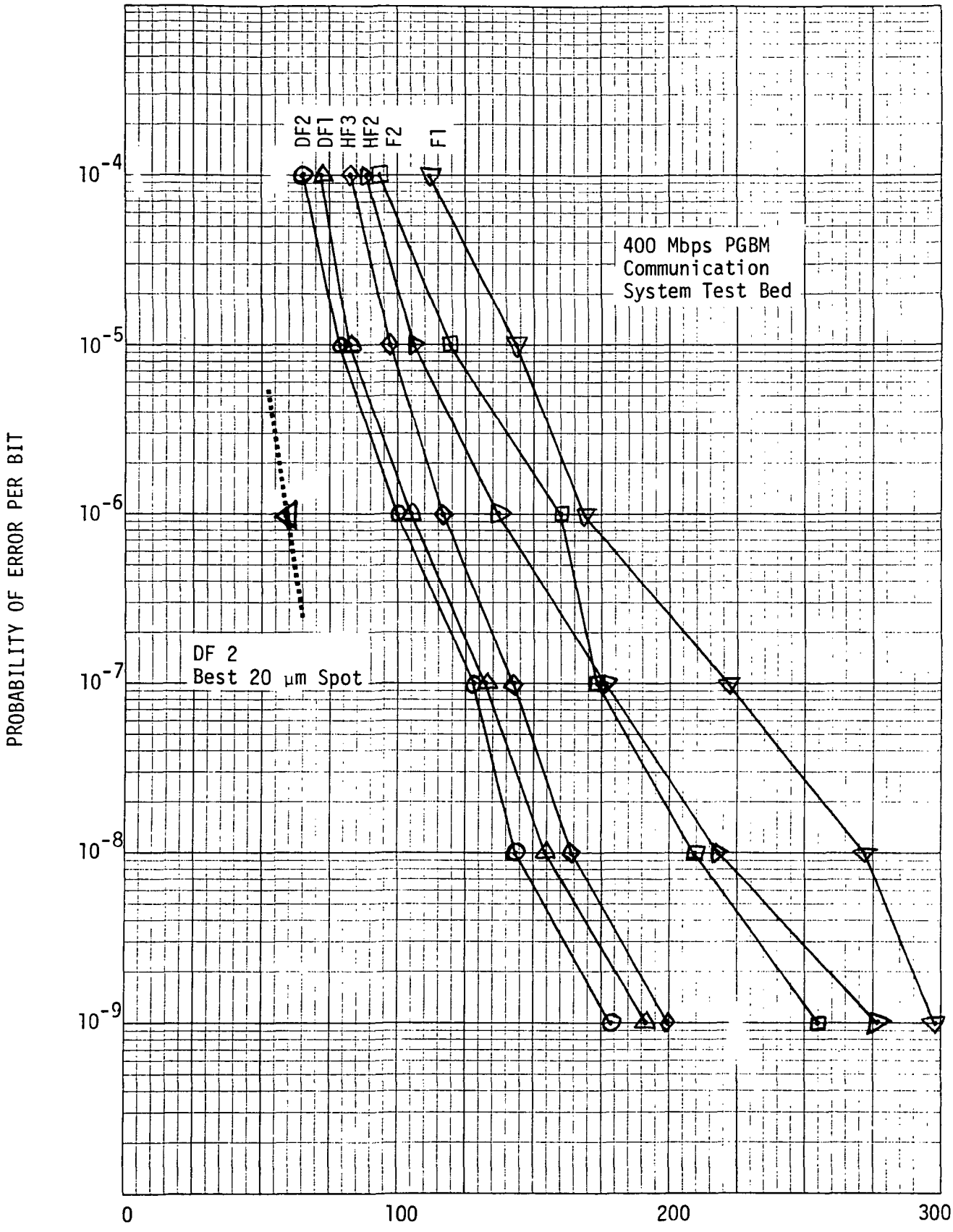

Figure 3 Heated Silicon APD Bit Error Rate Data

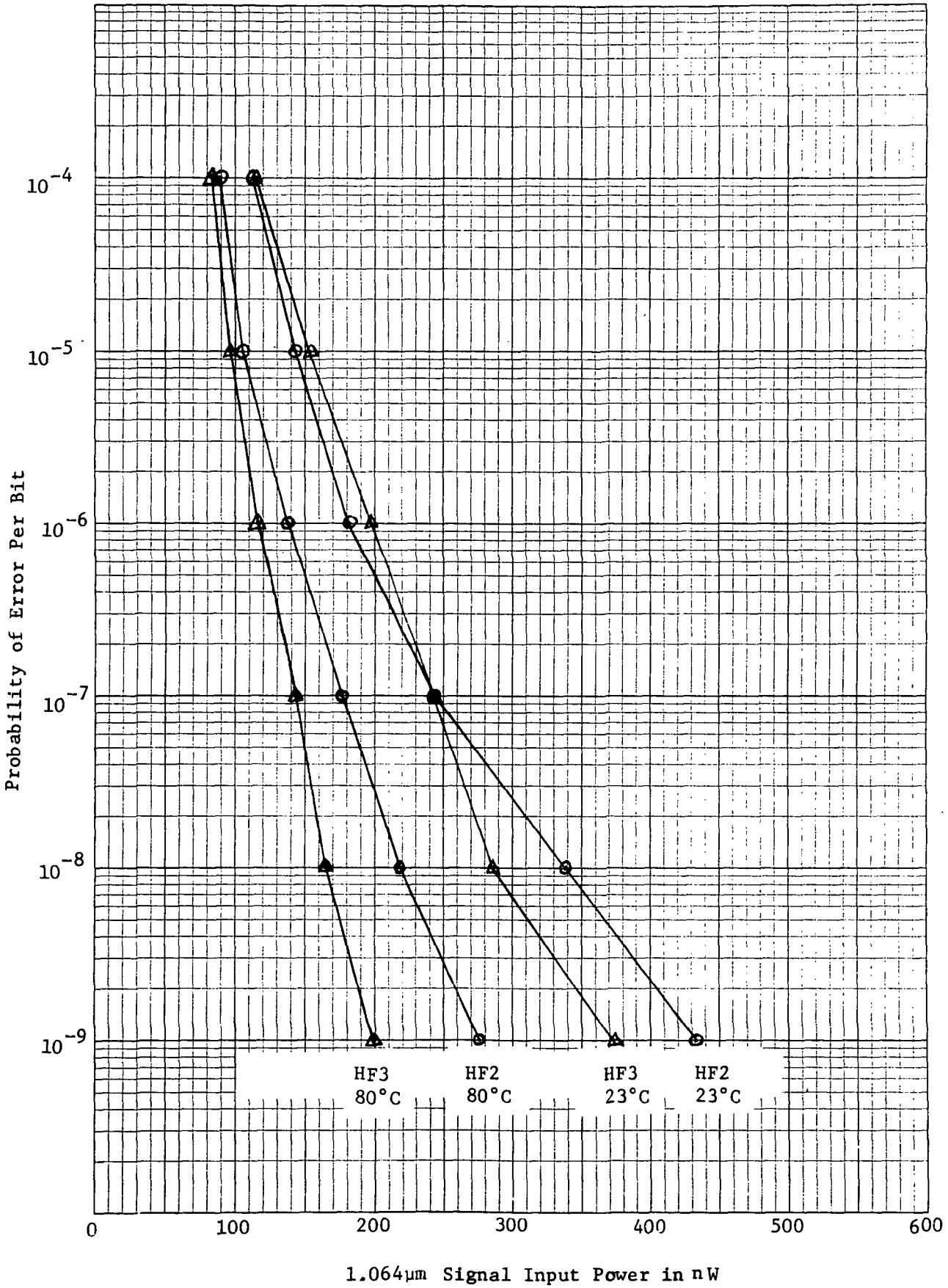

The dual wafer detectors were superior due to the increased quantum efficiency over the single wafer detectors. The heated detectors fell in between. Quantum efficiency increased at elevated temperature but dark current also increased. The heated detectors were operated only at the manufacturers recommended heater voltage level. It is likely that performance may be improved by optimizing the detector temperature by varying the heater reference current.

Inadvertently, the antireflection coatings on all front silicon surfaces were omitted during fabrication. The standard RCA coating would have reduced reflections at the air-silicon interface from 30% to 5% for incoming signals. The estimated improvement expected by antireflection coating the front surfaces is 11.5% for the single wafer detectors and 17.4% for the dual wafer detectors [2]. The adjacent inner faces of the two dual detectors were the only antireflection coated surfaces among the delivered detectors. The windows of the detector package were also uncoated and have a measured transmission of 87%. The superior dual wafer diodes would perform as tested with only 74.1% of the optical signal power measured above if the silicon wafer was antireflection coated and the window was eliminated (the Rockwell APD has no window) or made of improved material and antireflection coated.

2.3 UNIT TESTS.

2.3.1 Single Wafer Detector F1.

The current-voltage characteristics of detector F1 are plotted in Figure 4 for the conditions of no illumination and with ~0.1 μW of incident 1.064 μm radiation. The difference between the two curves is the responsivity of the detector as a function of applied bias.

Figure 5 shows the scanned photoresponse of detector F1. Displacement from the baseline is proportional to detected current at each point. The 1.064 μm input signal is modulated at 200 MHz. Scans of detected photo current and scans of the 200 MHz component of the photocurrent (amplified, filtered, and square law detected) are shown. Below 130V bias, normal operation of the diode ceased as the depletion region no longer "reached through" into the drift

[2] P. P. Webb Private Communication

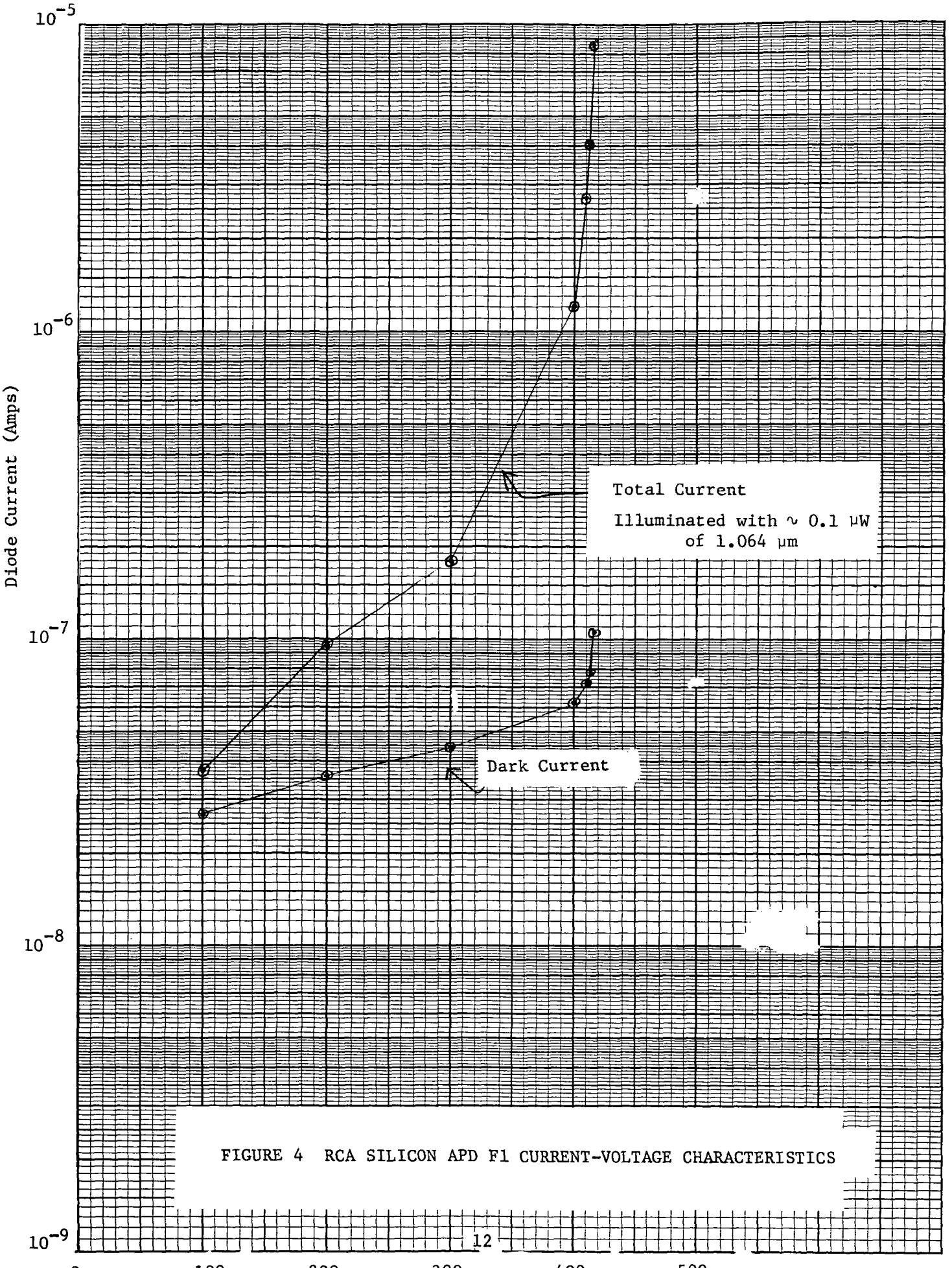

FIGURE 4 RCA SILICON APD F1 CURRENT-VOLTAGE CHARACTERISTICS

REPRODUCIBILITY OF THE
ORIGINAL PAGE IS POOR

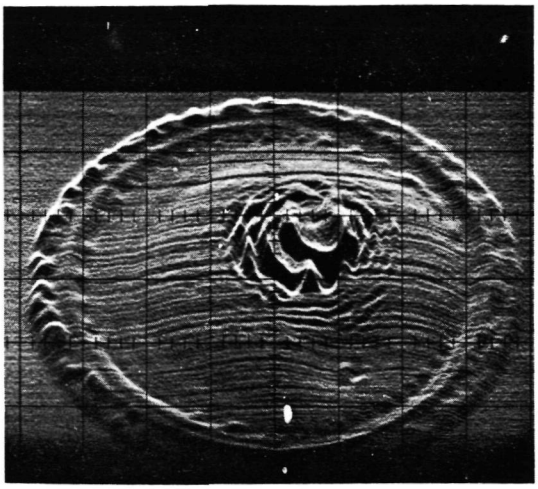

10 μw
–100V

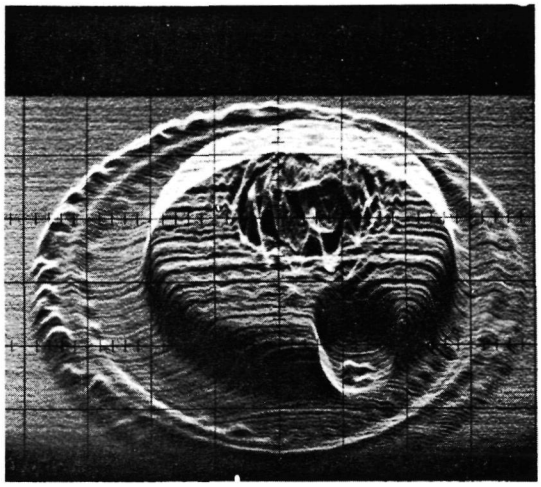

10 μw
–120V

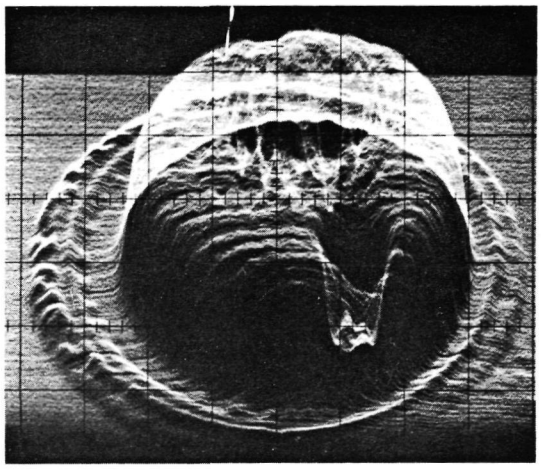

10 μw
–200V

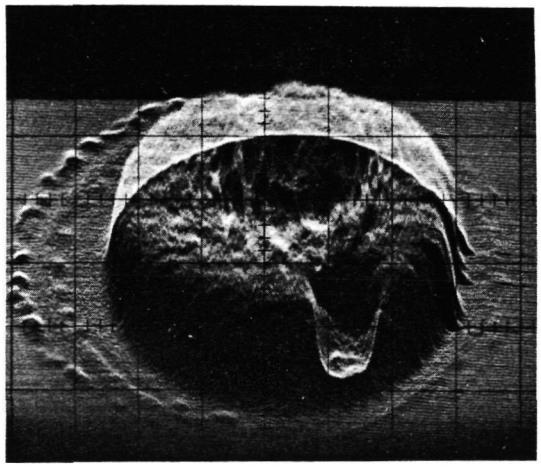

DC

200 MHz

FIGURE 5A RCA SILICON APD F1 1.064 μm PHOTORESPONSE SCANS

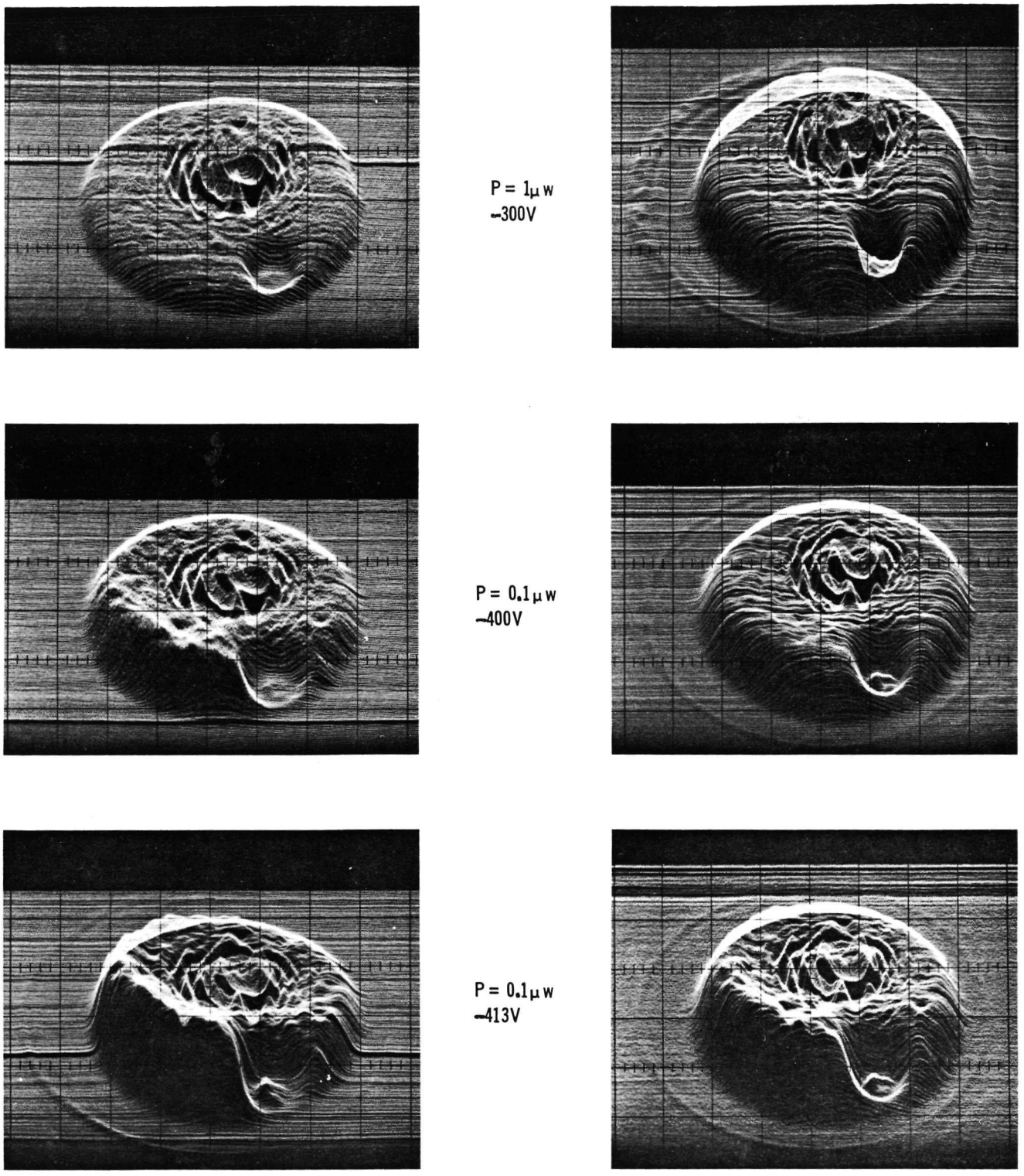

FIGURE 5B RCA SILICON APD F1 1.064 μm PHOTORESPONSE SCANS

REPRODUCIBILITY OF THE
ORIGINAL PAGE IS POOR

region. Extremely good uniformity was observed up to maximum gain, and the response at 200 MHz was identical to the response at baseband.

Figure 6 shows the output waveform of detector F1 in response to the modulated laser communication system transmitter signal. The response was sufficiently fast to return to the baseline between adjacent transmitted "1" pulses spaced 2.5 ns apart. Figure 7 shows the response of detector F1 to a narrow pulse (180 ps at 10% of maximum) from a Nd:YAG laser. Pulse width at the base was 2.5 ns, sufficiently fast for 400 Mbps.

Figure 8 shows a plot of noise equivalent input power (NEIP) versus applied bias voltage for detector F1. NEIP decreased with increasing gain until noise from the multiplied bulk leakage current became significant, and then increased again. Optimum bias was -413V.

2.3.2 Single Wafer Detector F2

The current-voltage characteristics of detector F2 are plotted in Figure 9 for the conditions of no illumination and with ~0.1μW of incident 1.064 μm radiation. The dark current rose more abruptly at high gain than that of detector F1 because of the significantly lower bulk leakage current as indicated in Table III. Total dark current equaled surface leakage current plus current gain times bulk leakage current. In each case comparing detectors of similar types, the unit with lower dark bulk leakage current had better system performance.

Figure 10 shows the scanned photoresponse of detector F2. Scans of the photocurrent and of the 200 MHz component of the photocurrent are shown. Response was uniform at a gain of 50. At a gain of 300, there was a 4 to 1 variation in response over the photosensitive area. Baseband response was identical to 200 MHz response.

Figure 11 shows the output waveform of detector F2 in response to the modulated transmitter signal. The response was sufficiently fast to return to the baseline between adjacent pulses. Figure 12 shows the impulse response of detector F2. Pulse width at the base was 2.5 ns.

FIGURE 6 RCA SILICON APD F1 OUTPUT WAVEFORM

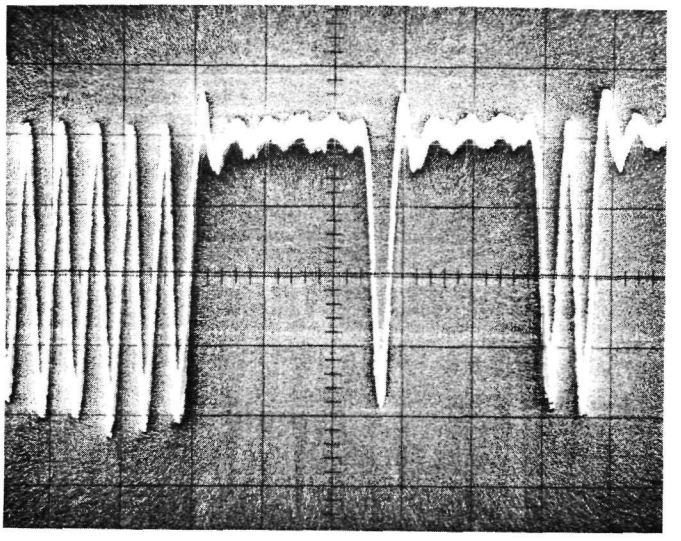

5 nsec/div
−413V BIAS
10 μA AVERAGE

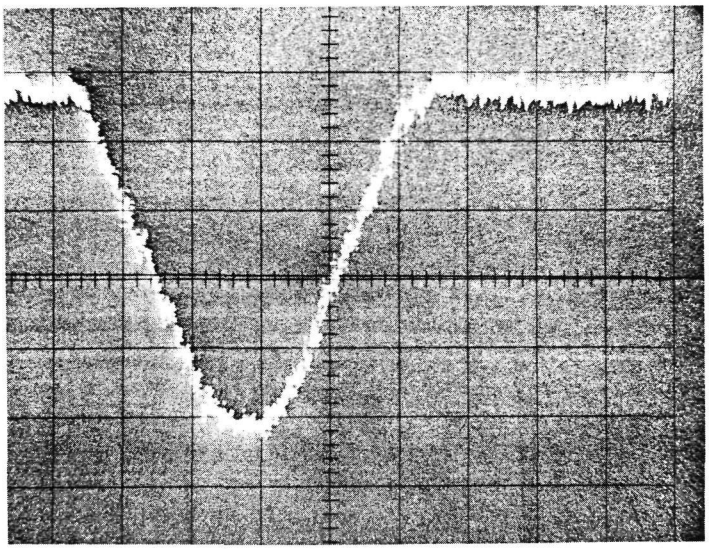

-400V

Horizontal 500 ps/div
Vertical 1 mV/div

Figure 7 RCA Silicon APD F1 Impulse Response

FIGURE 8 RCA SILICON APD F2 NOISE EQUIVALENT INPUT POWER

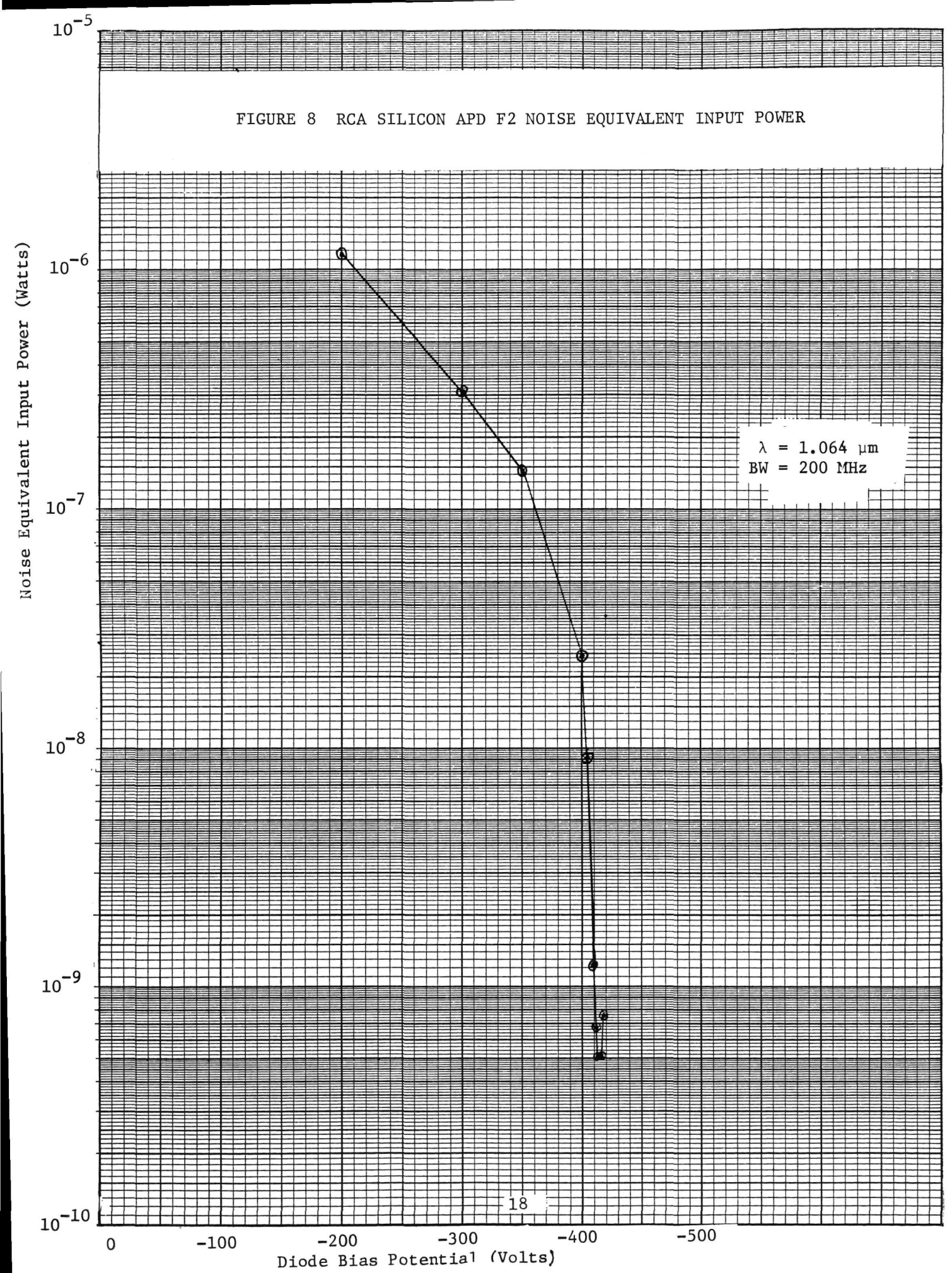

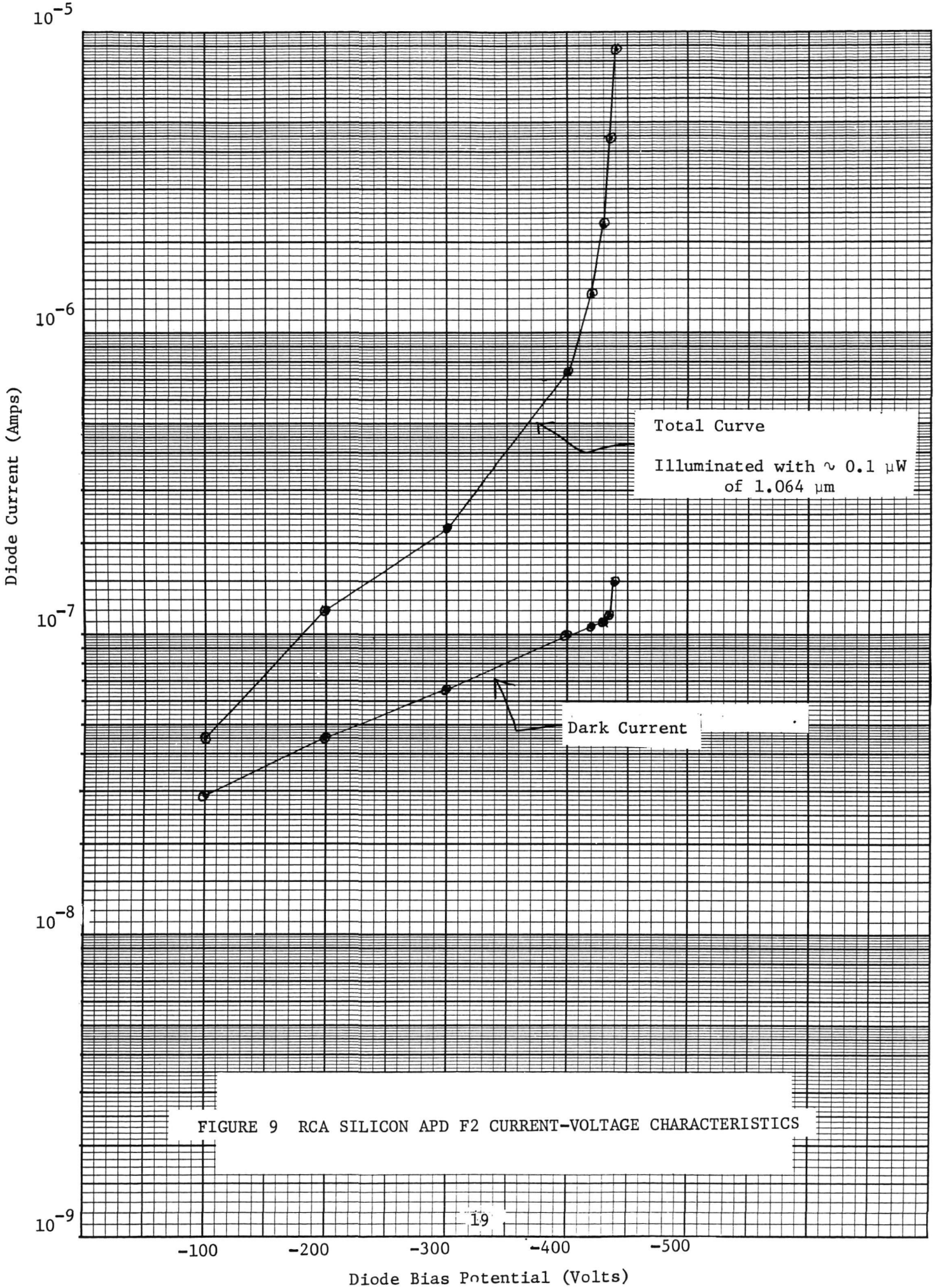

FIGURE 9 RCA SILICON APD F2 CURRENT-VOLTAGE CHARACTERISTICS

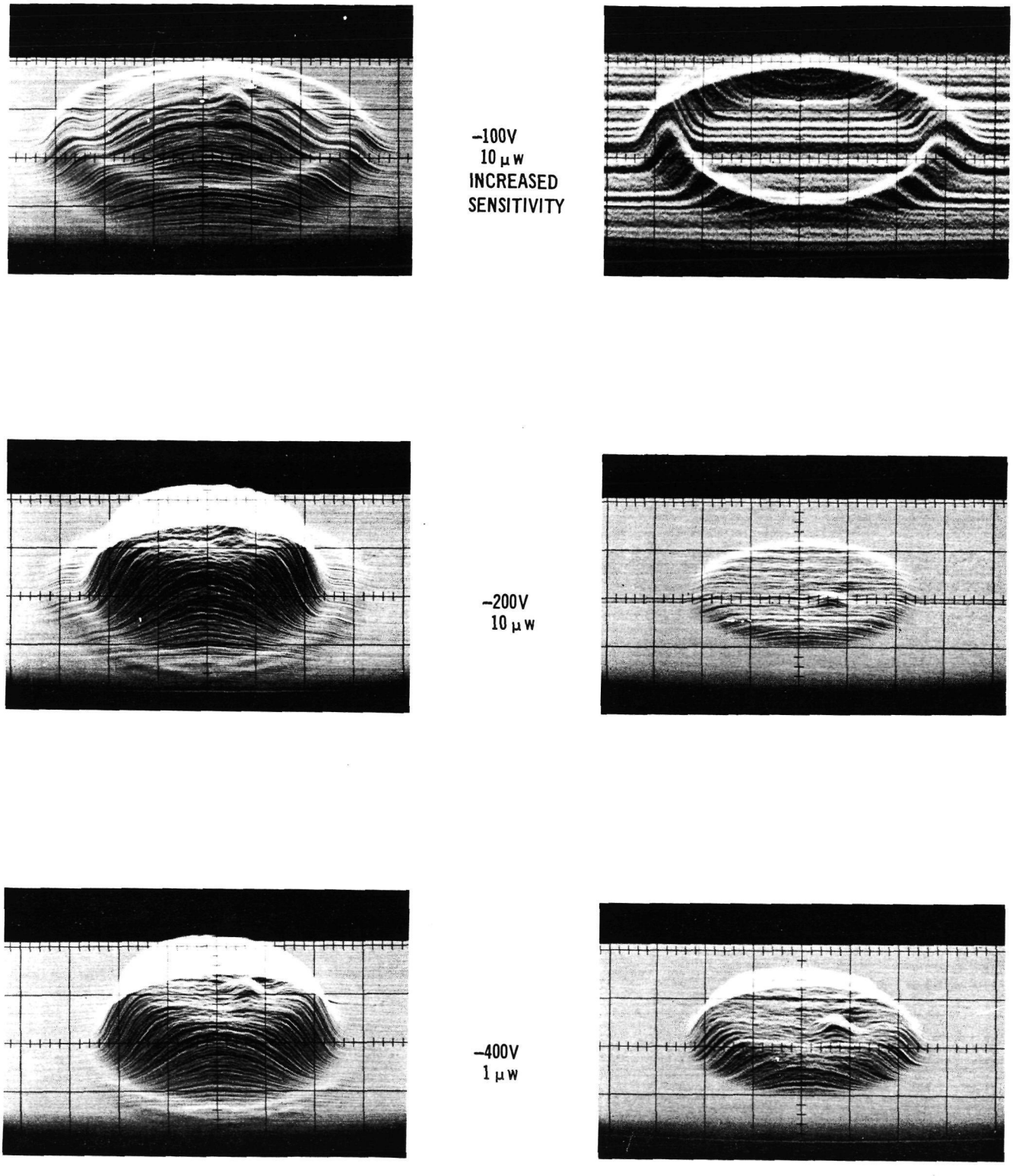

FIGURE 10A RCA SILICON APD F2 1.064 μm PHOTORESPONSE SCANS

REPRODUCIBILITY OF THE
ORIGINAL PAGE IS POOR

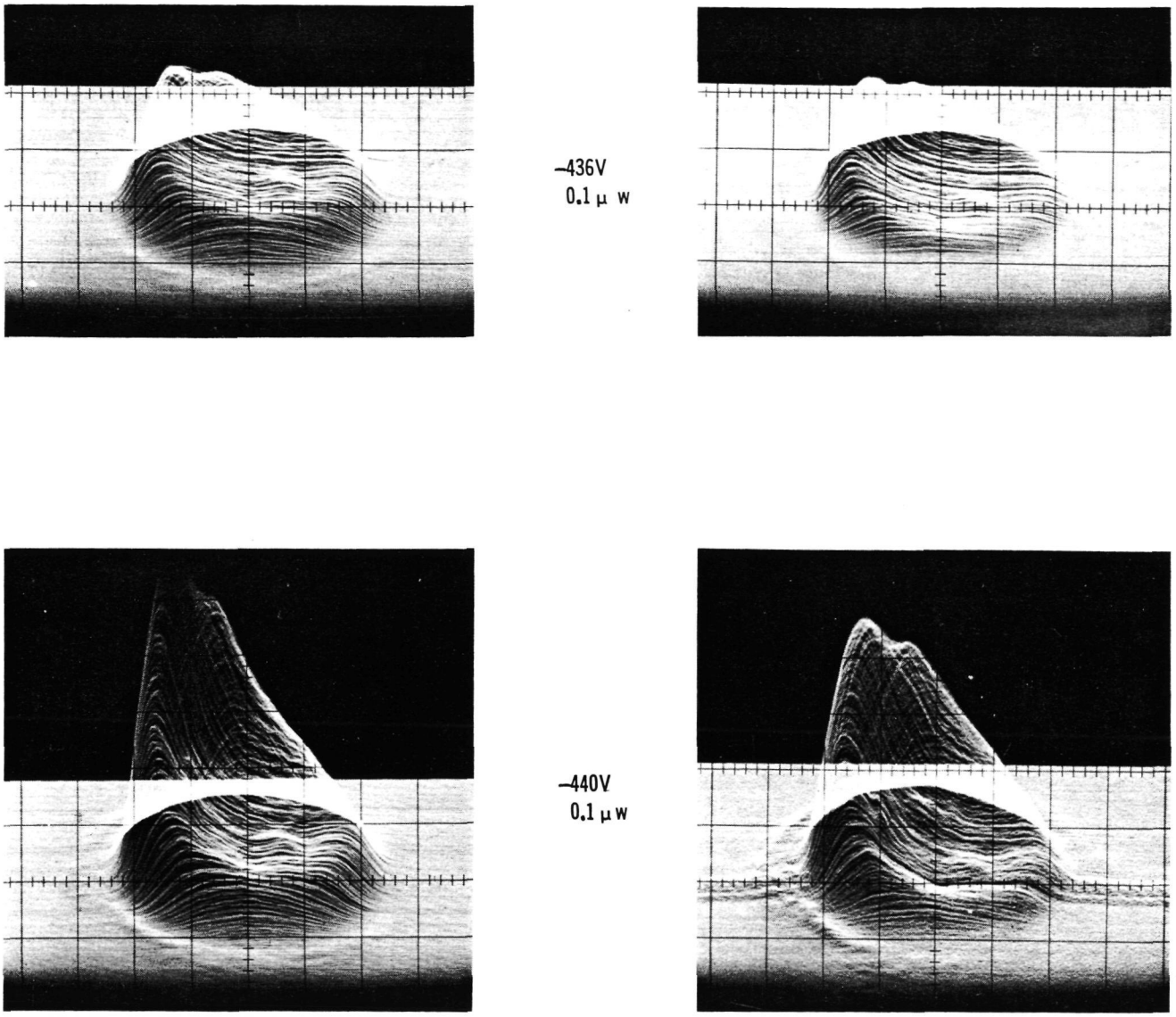

FIGURE 10B RCA SILICON APD F2 1.064 μm PHOTORESPONSE SCANS

FIGURE 11 RCA SILICON APD F2 OUTPUT WAVEFORM

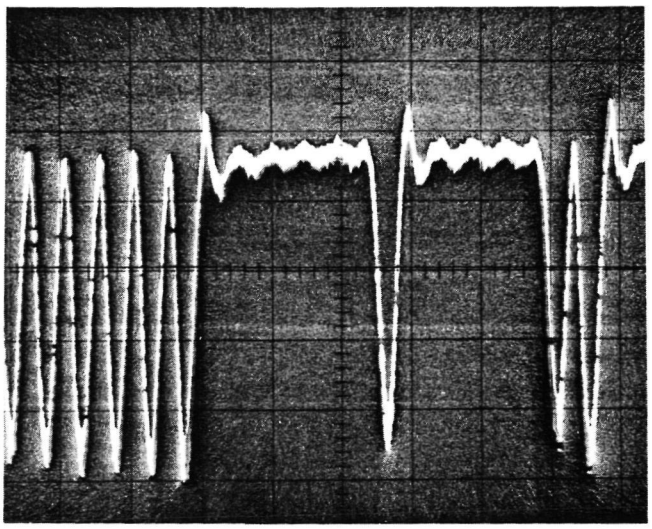

5 nsec/div
−436V BIAS
10 μA AVERAGE

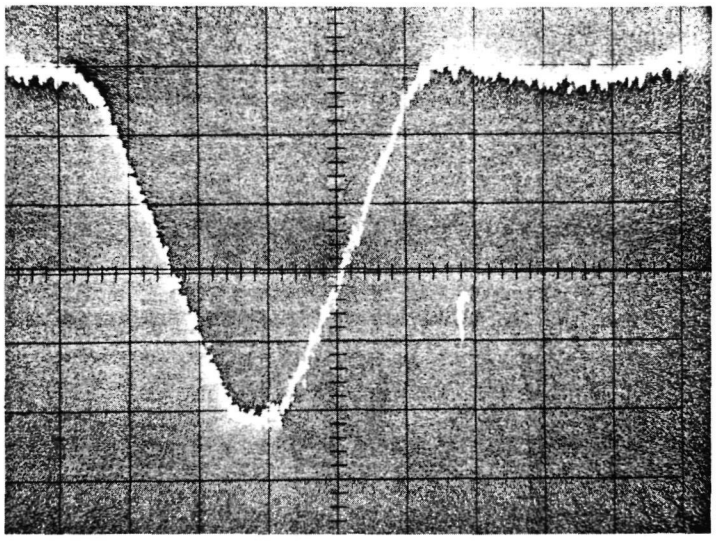

-436 V

Horizontal 500 ps/div

Vertical 1 mV/div

Figure 12 RCA Silicon APD F2 Impulse Response

Figure 13 shows a plot of NEIP versus applied bias for detector F2. Optimum bias was -438V.

2.3.3 Dual Wafer Detector DF1.

The current-voltage characteristics of detector DF1 are plotted in Figure 14 for the conditions of no illumination and with ∿0.1 μW of incident 1.064 μm radiation. The dark leakage current of two diodes in parallel was correspondingly higher than for the single diodes.

Figure 15 shows the scanned photoresponse of detector DF1. Scans of the photocurrent and of the 200 MHz component of the photocurrent are shown. Note that the photosensitive area was a circle truncated by two parallel chords. The two missing areas were electroded with gold in order to make electrical contact to what is normally the mirrored rear surface of the diodes. Response was uniform at a gain of 35. At a gain of 200, there was a 3 to 1 variation in response over the photosensitive area. Baseband response was identical to 200 MHz response.

Figure 16 shows the output waveform of detector DF1 in response to the modulated transmitter signal. The response was sufficiently fast to return to the baseline between adjacent pulses. Figure 17 shows the impulse response of detector DF1. Pulse width at the base was 2.5 ns.

Figure 18 shows a plot of NEIP versus applied bias for detector DF1. Optimum bias was -394V.

2.3.4 Dual Wafer Detector DF2.

The current-voltage characteristics of detector DF2 are plotted in Figure 19 for the conditions of no illumination and with ∿0.1 μW of incident 1.064 μm radiation.

Figure 20 shows the scanned photoresponse of detector DF2. Scans of the photocurrent and of the 200 MHz component of the photocurrent are shown. Response was moderately uniform at a gain of 25.

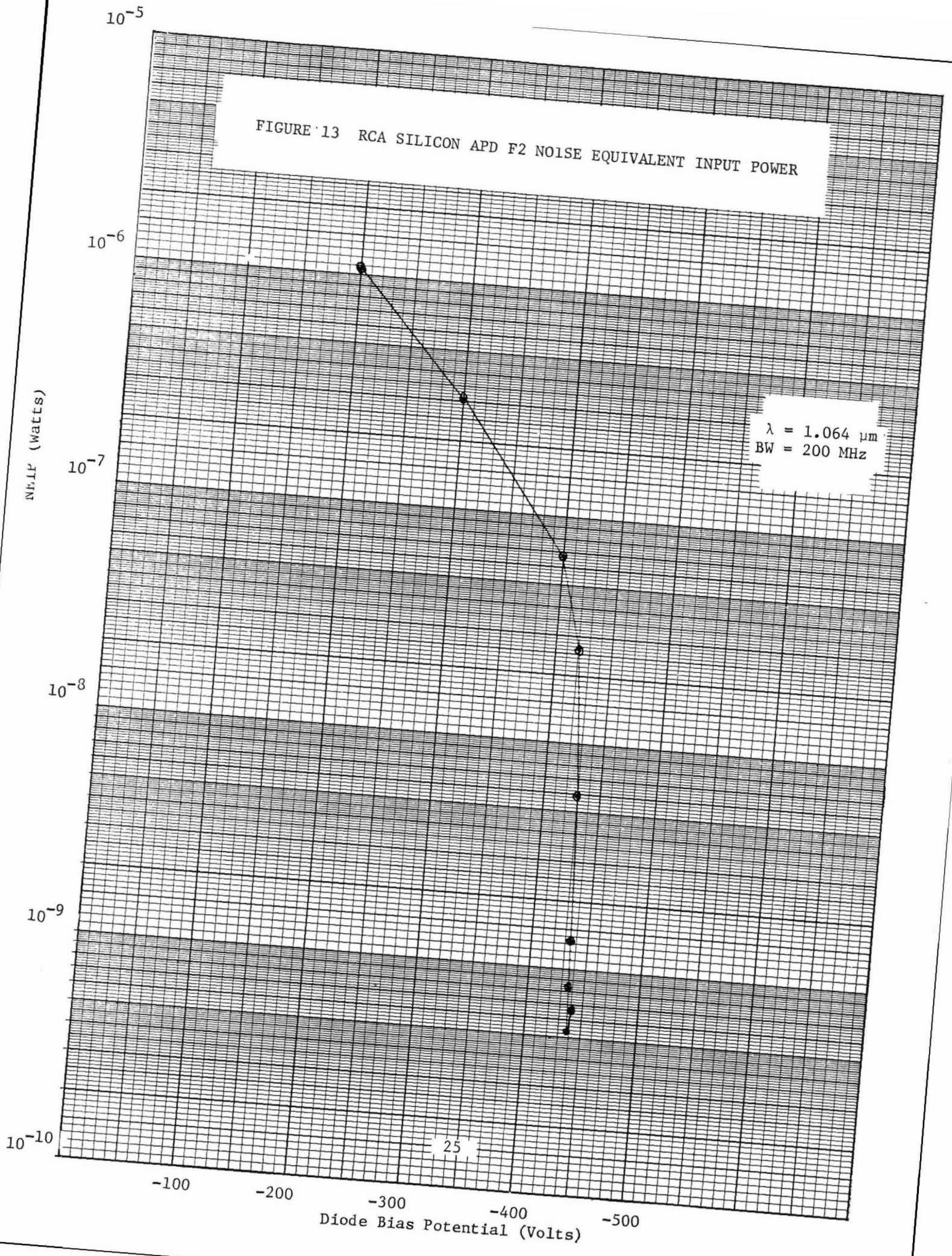
FIGURE 13 RCA SILICON APD F2 NOISE EQUIVALENT INPUT POWER
10^{-5}
10^{-6}
10^{-7}
10^{-8}
10^{-9}
10^{-10}
NEP (Watts)
λ = 1.064 μm
BW = 200 MHz
-100
-200
-300
-400
-500
Diode Bias Potential (Volts)

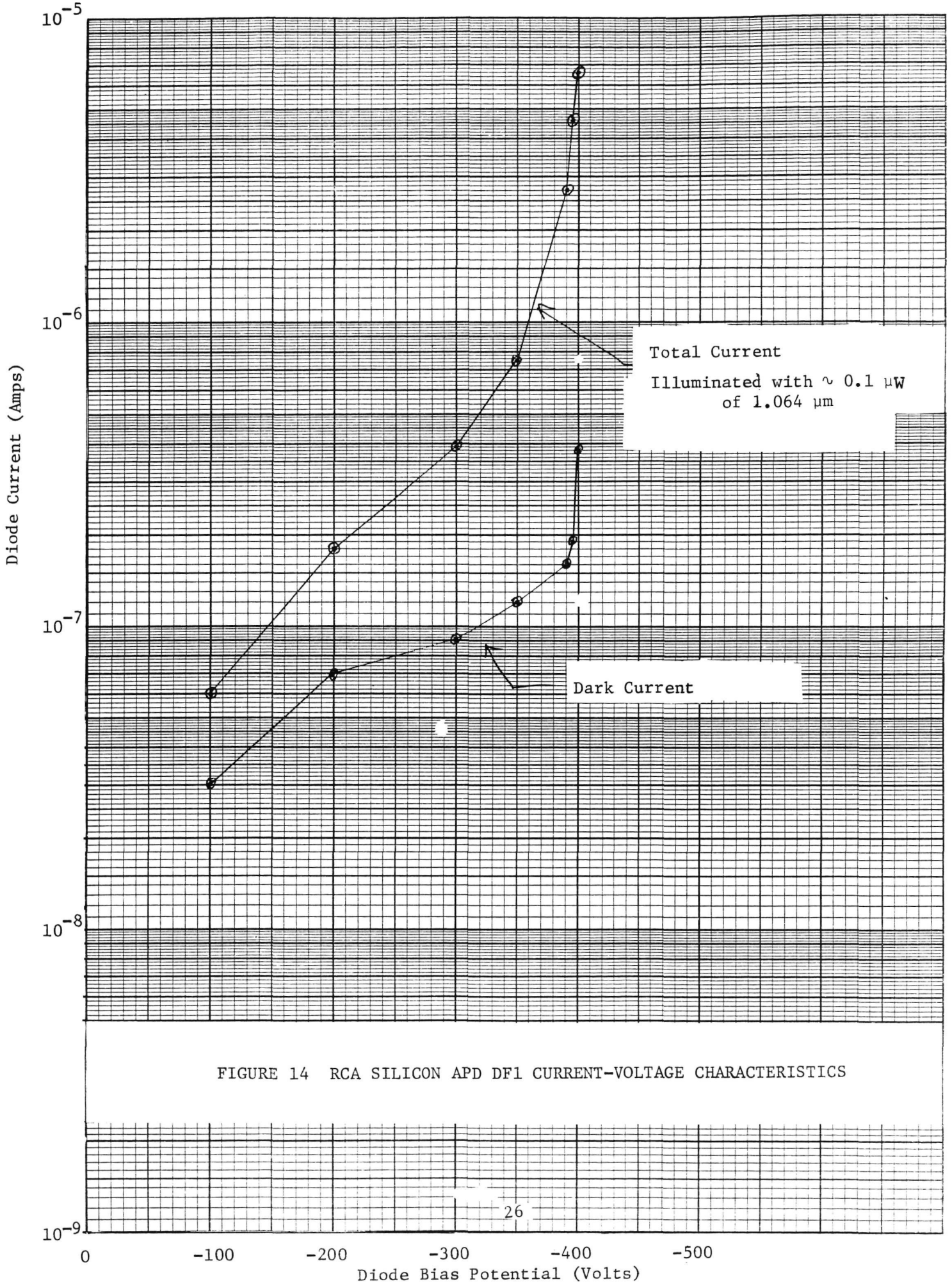

FIGURE 14 RCA SILICON APD DF1 CURRENT-VOLTAGE CHARACTERISTICS

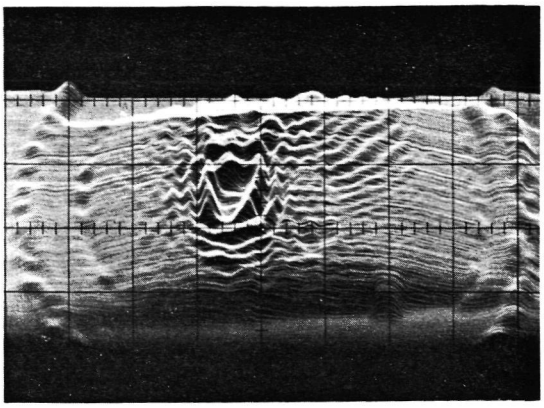

−100V
10 μw

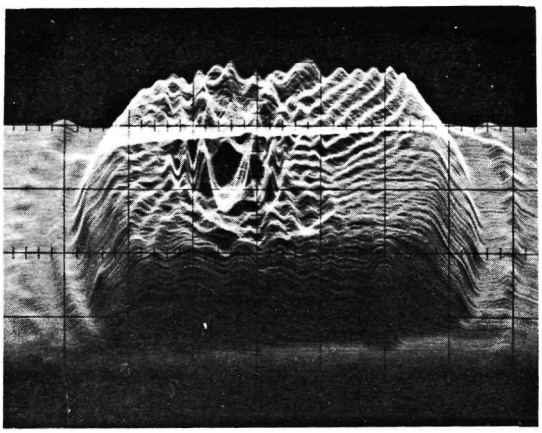

−200V
5 μw

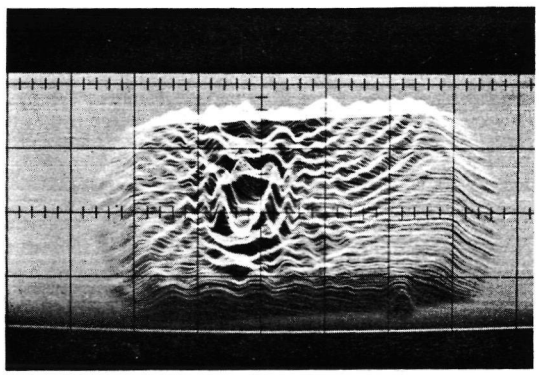

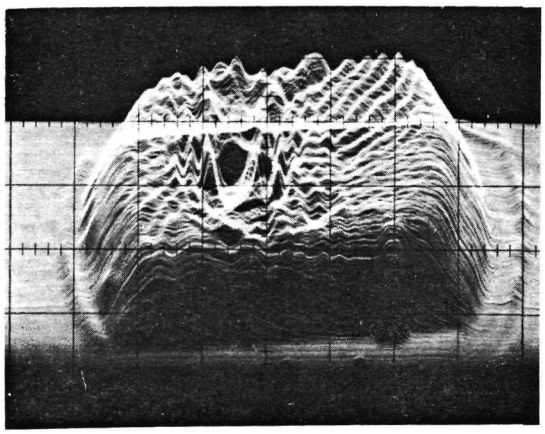

−350V
1 μw

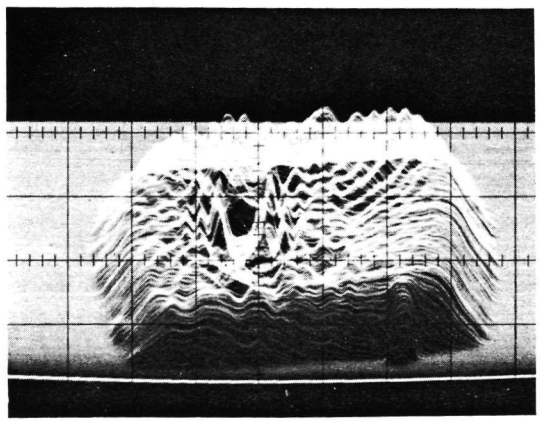

DC

200 MHz

FIGURE 15A RCA SILICON APD DF1 1.064 μm PHOTORESPONSE SCANS

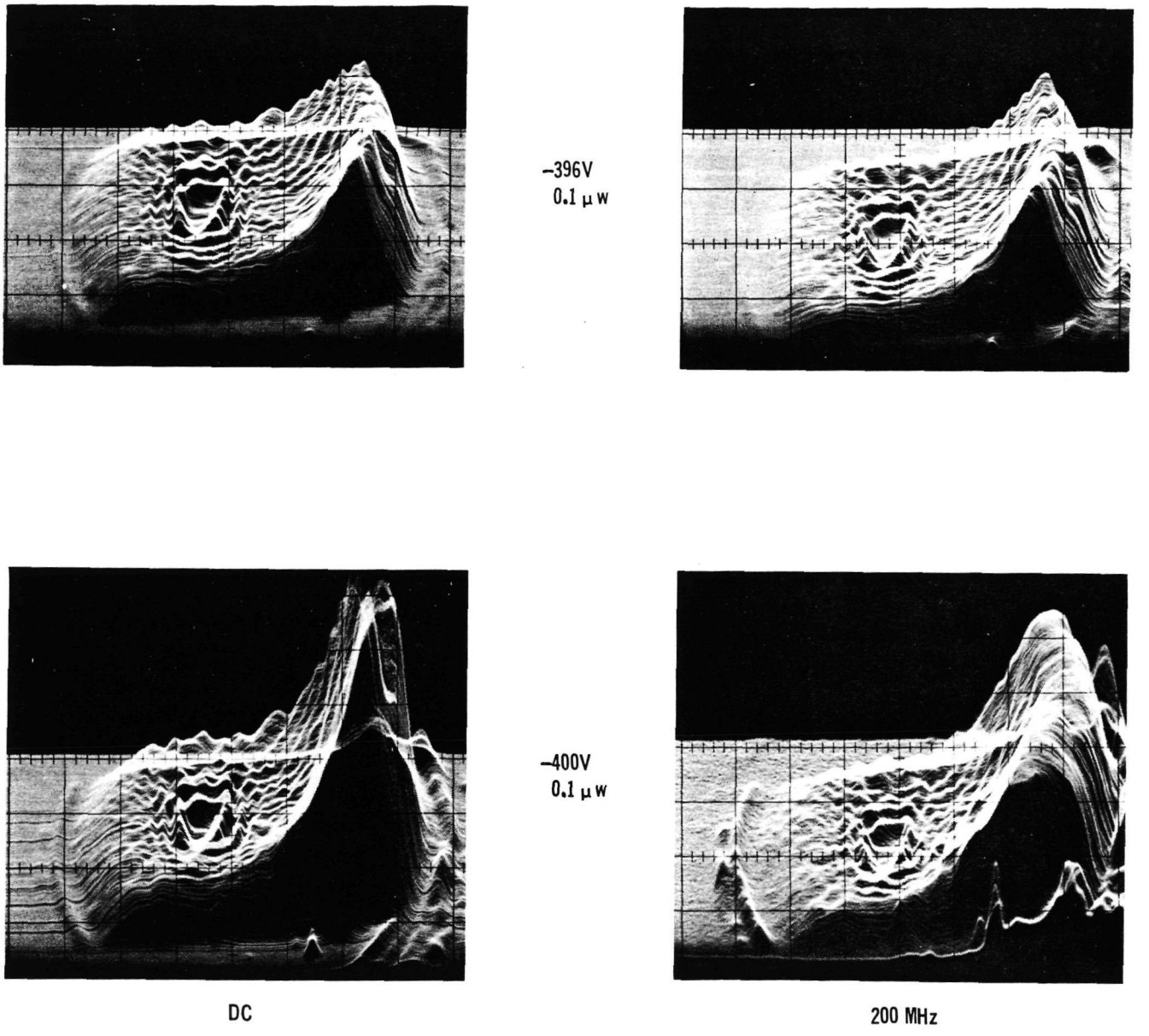

FIGURE 15B RCA SILICON APD DF1 1.064 μm PHOTORESPONSE SCANS

REPRODUCIBILITY OF THE
ORIGINAL PAGE IS POOR

FIGURE 16 RCA SILICON APD DF1 OUTPUT WAVEFORM

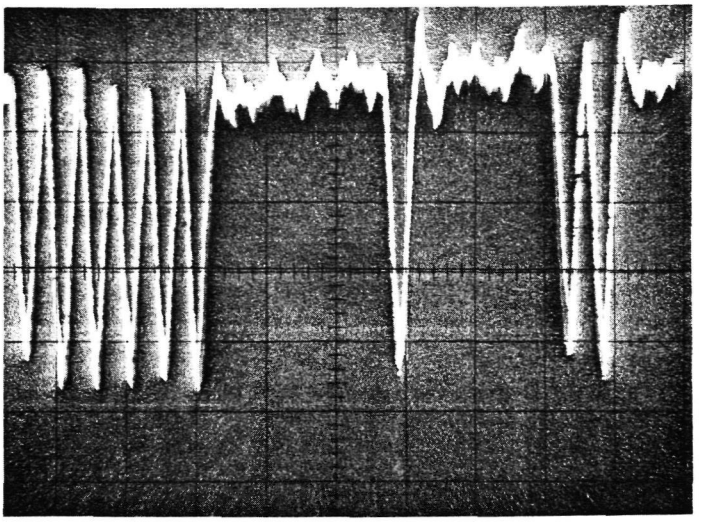

5 nsec/div
−396V BIAS
10 μA AVERAGE

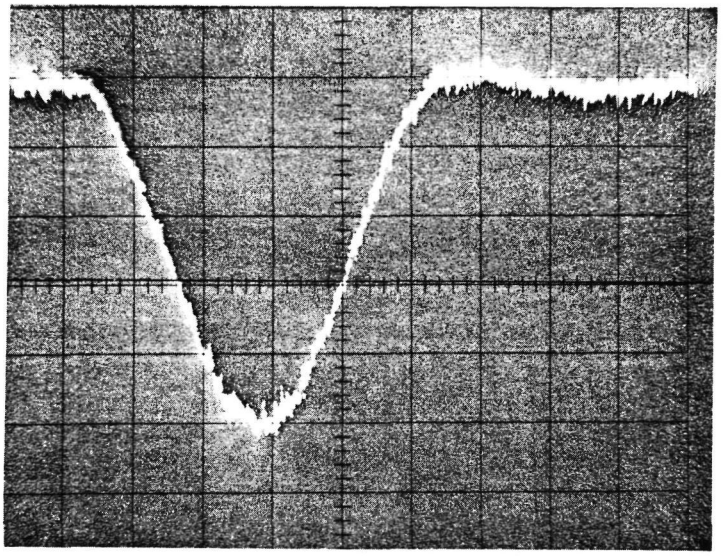

-396 V

Horizontal 500 ps/div

Vertical 1 mV/div

Figure 17 RCA Silicon APD DF1 Impulse Response

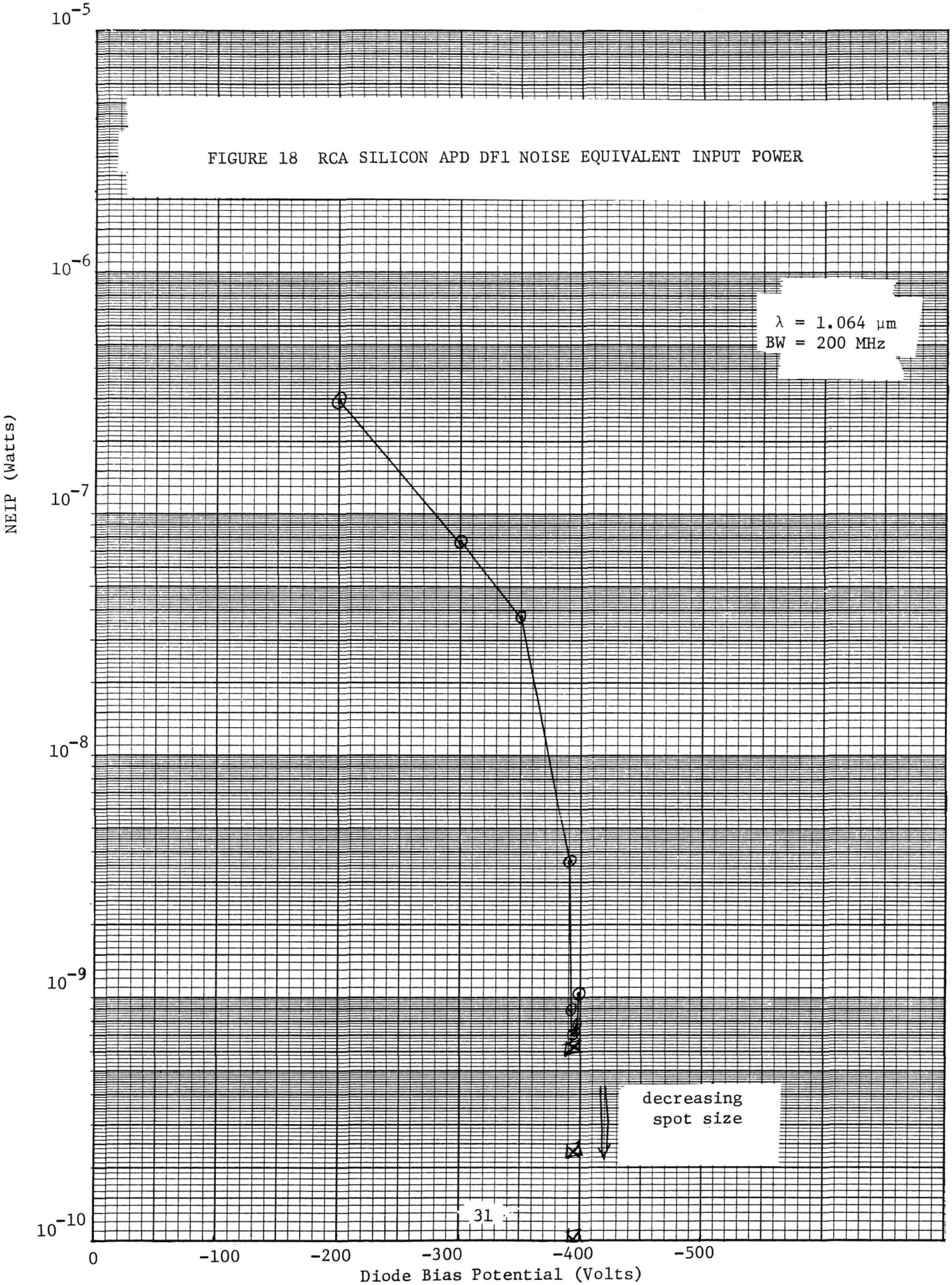
FIGURE 18 RCA SILICON APD DF1 NOISE EQUIVALENT INPUT POWER
λ = 1.064 μm
BW = 200 MHz
decreasing
spot size
NEIP (Watts)
10^-5
10^-6
10^-7
10^-8
10^-9
10^-10
0
-100
-200
-300
-400
-500
Diode Bias Potential (Volts)

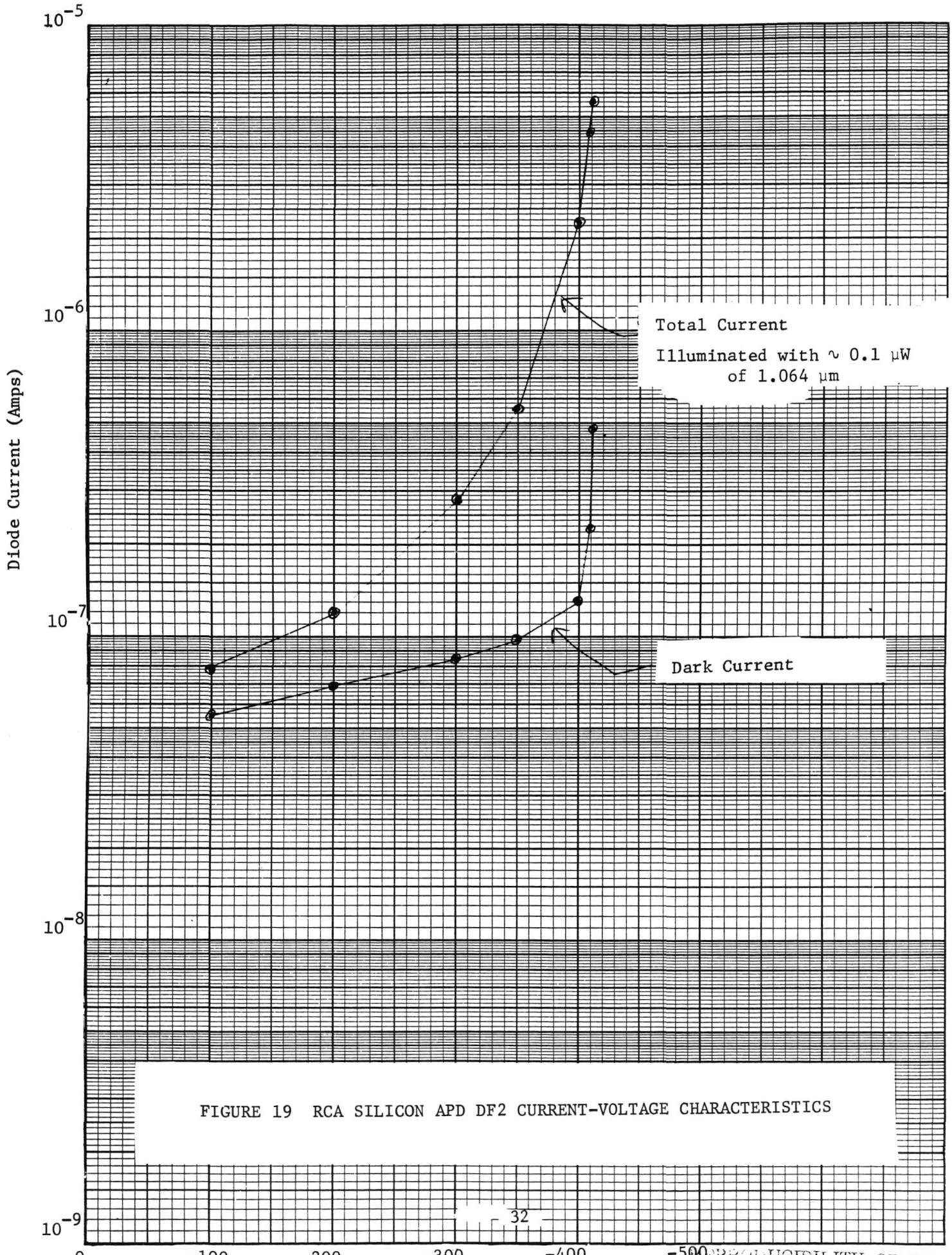

FIGURE 19 RCA SILICON APD DF2 CURRENT-VOLTAGE CHARACTERISTICS

REPRODUCIBILITY OF THE
ORIGINAL PAGE IS POOR

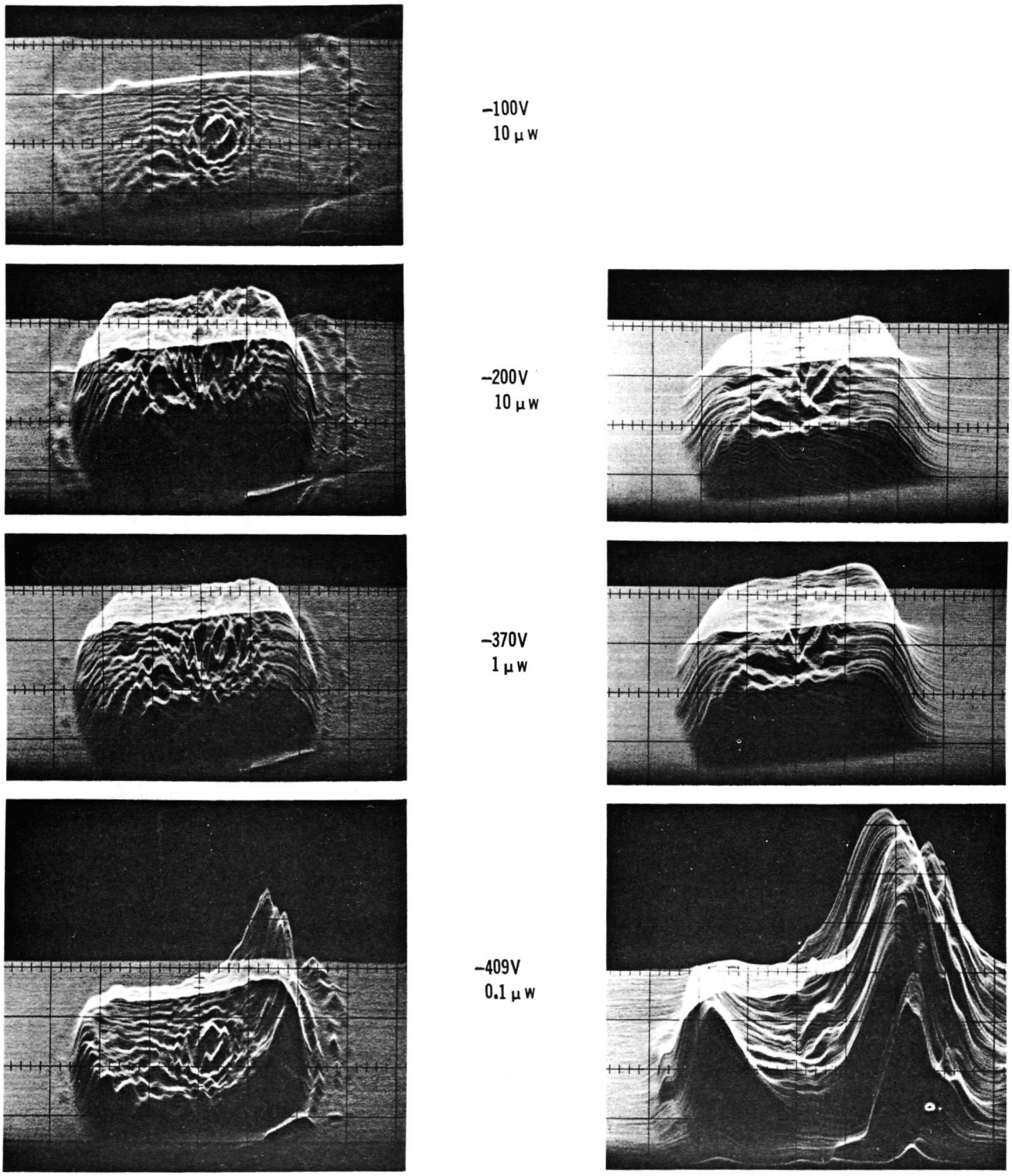

FIGURE 20 RCA SILICON APD DF2 1.064 μm PHOTORESPONSE SCANS

At a gain of 200, there was a 3 to 1 variation in response over the photosensitive area. Baseband response was identical to response at 200 MHz.

Figure 21 shows the output waveform of detector DF2 in response to the modulated transmitter signal. The response was sufficiently fast to return to the baseline between adjacent pulses. Figure 22 shows the impulse response of detector DF2. Pulse width at the base was 2.6 ns.

Figure 23 shows a plot of NEIP versus applied bias for detector DF2. Optimum bias was -406V.

2.3.5 Heated Detector HF2.

The current-voltage characteristics of detector HF2 are plotted in Figure 24 for the conditions of no illumination and with ∿0.1 μW of incident 1.064 μm radiation. Note that the curves for the heated detectors are presented on a different scale, because dark current was 50 times greater at 80°C than at room temperature.

Figure 25 shows the scanned photoresponse of detector HF2. Scans of the photocurrent and of the 200 MHz component of the photocurrent are shown. Response was uniform at a gain of 20. At a gain of 300, there was a 5 to 1 variation in response over the photosensitive area. Baseband response was identical to response at 200 MHz.

Figure 26 shows the output waveform of detector HF2. The response was sufficiently fast to return to the baseline between adjacent pulses. Figure 27 shows the impulse response of detector HF2 at room temperature and at +80°C. In both cases the pulse width at the base was 2.6 ns.

Figure 28 shows a plot of NEIP versus applied bias for detector HF2. Optimum bias was -436V.

2.3.6 Heated Detector HF3.

The current-voltage characteristics of detector HF3 are plotted in Figure 29 for the conditions of no illumination and with ∿0.1 μW of incident 1.064 μm radiation.

REPRODUCIBILITY OF THE
ORIGINAL PAGE IS POOR

FIGURE 21 RCA SILICON APD DF2 OUTPUT WAVEFORM

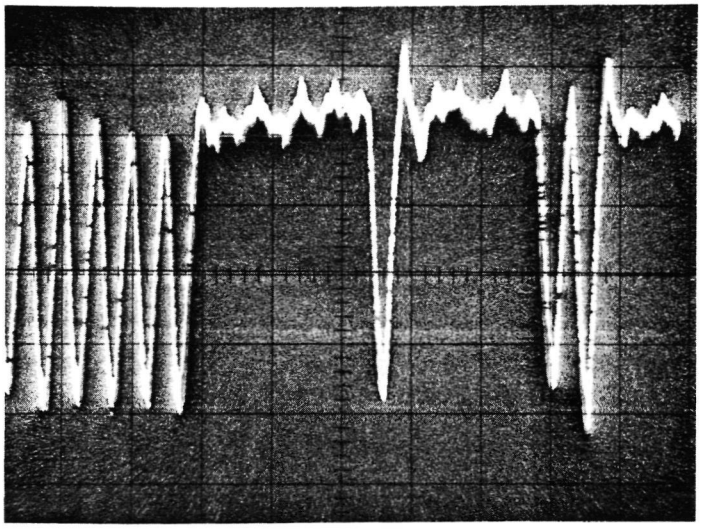

5 nsec/div
–400V BIAS
10 μA AVERAGE

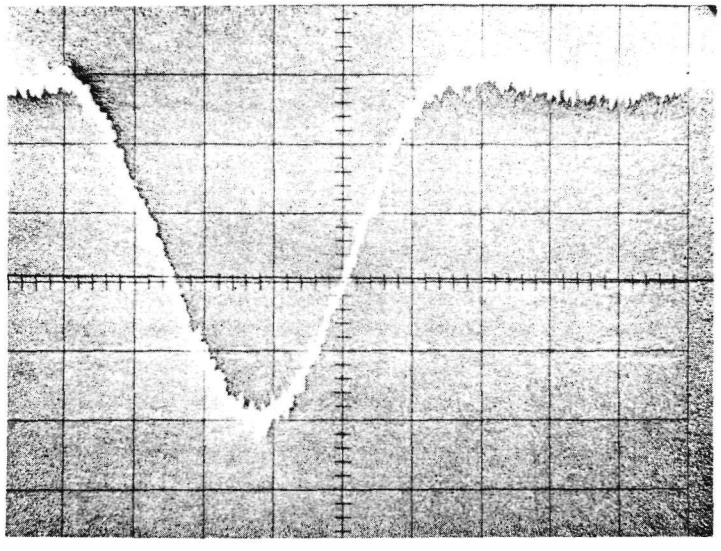

-400 V

Horizontal 500 ps/div

Vertical 1 mV/div

Figure 22 RCA Silicon APD DF2 Impulse Response

FIGURE 23 RCA SILICON APD DF2 NOISE EQUIVALENT INPUT POWER

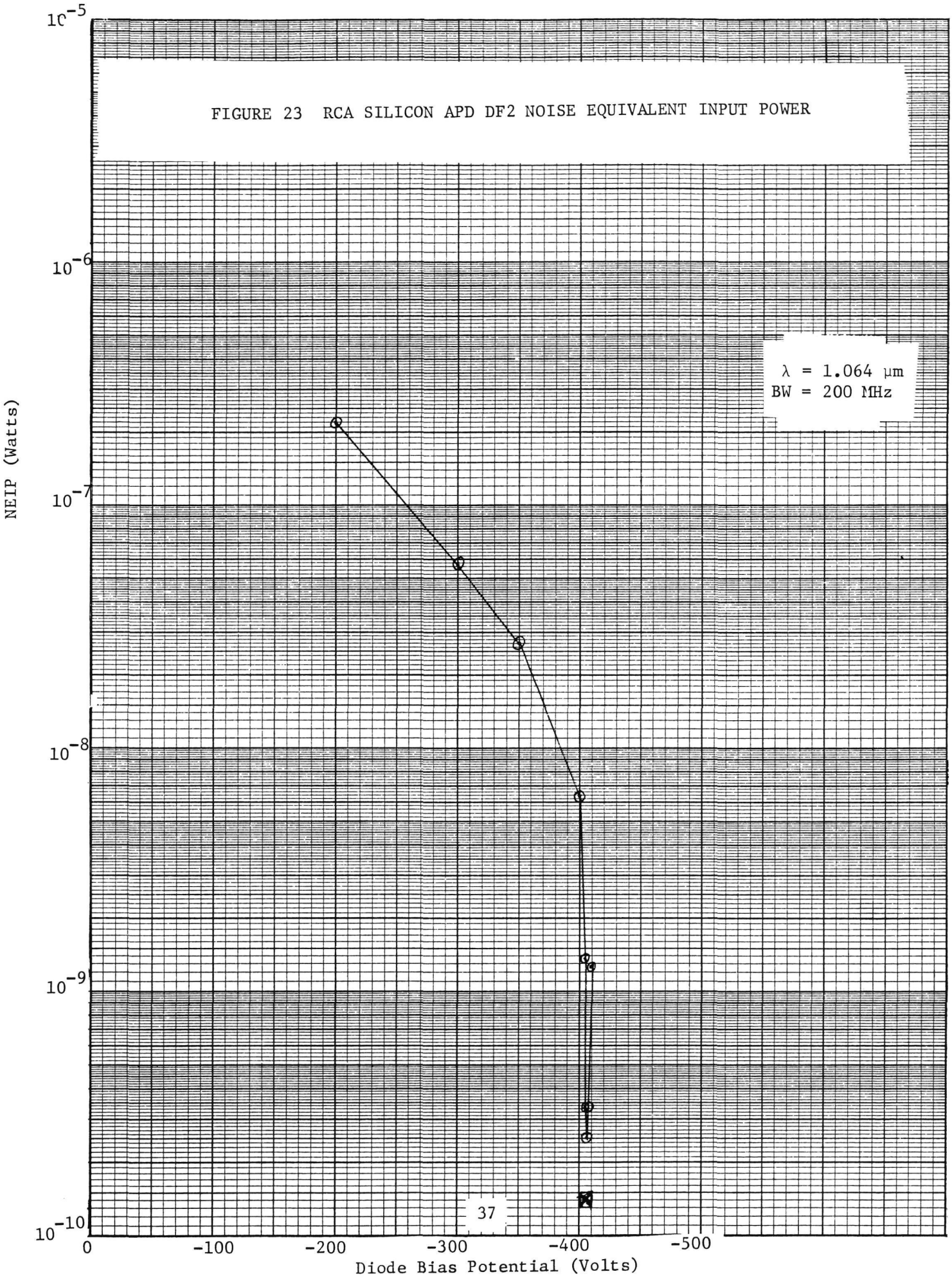

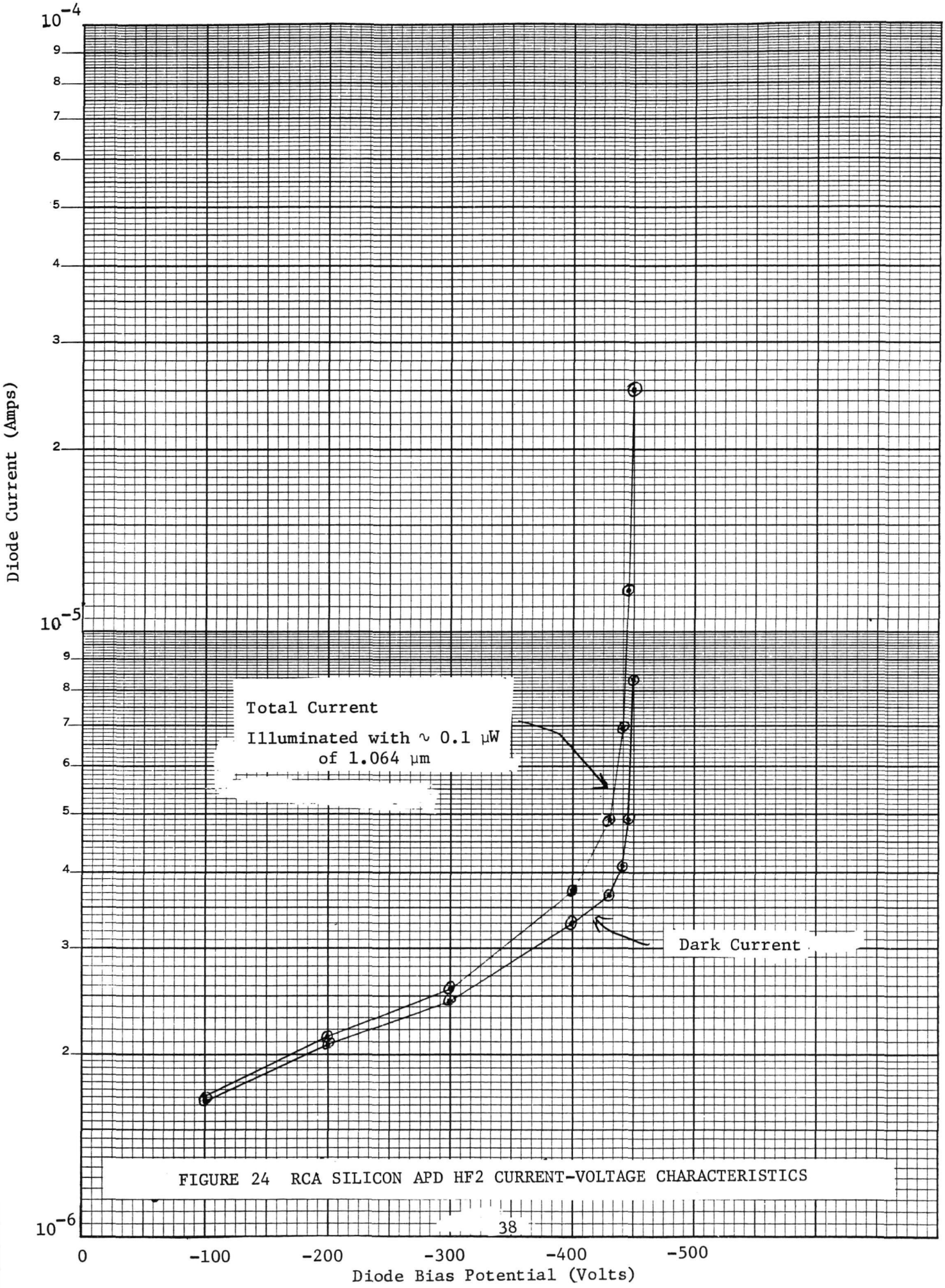

FIGURE 24 RCA SILICON APD HF2 CURRENT-VOLTAGE CHARACTERISTICS

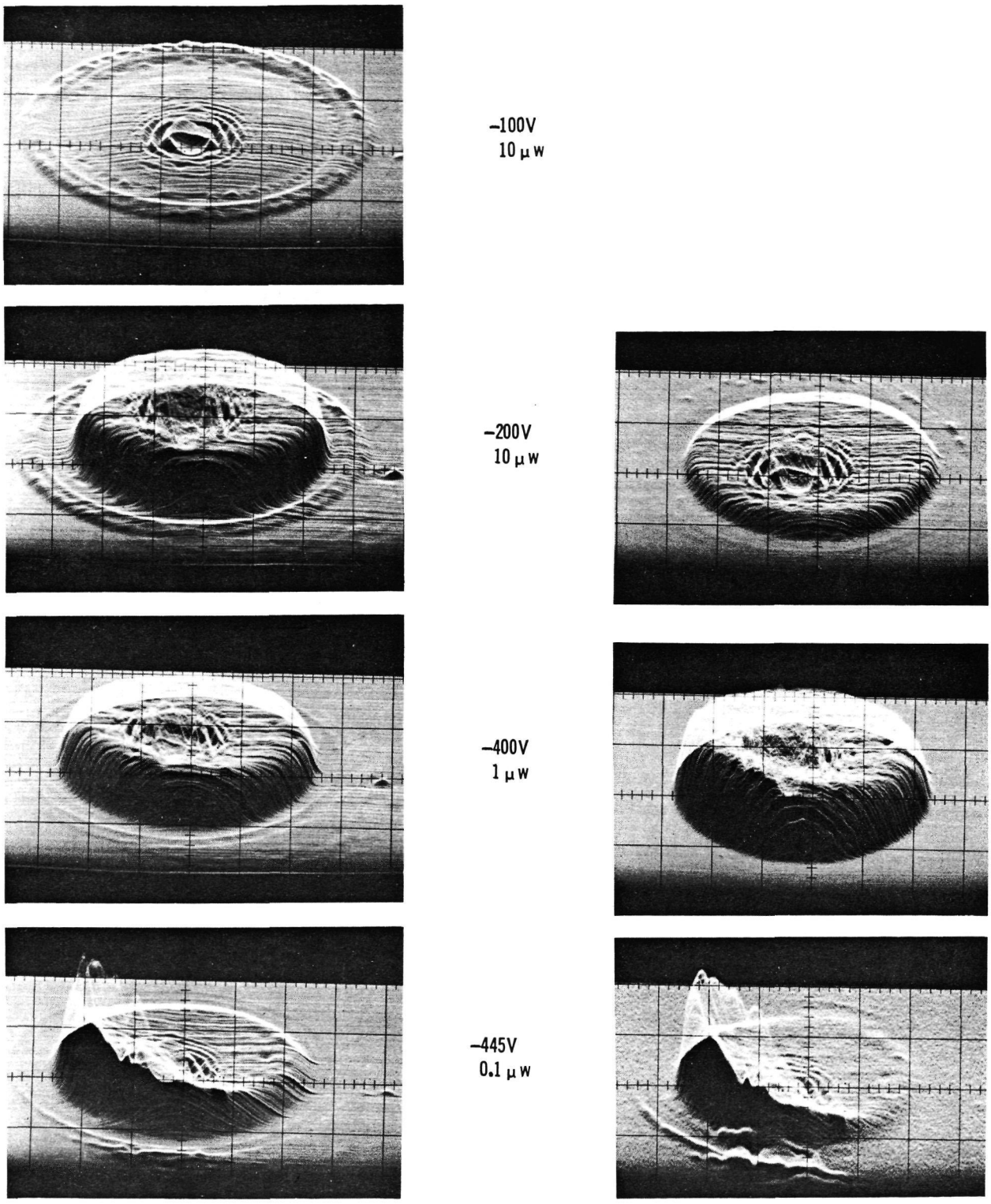

FIGURE 25 RCA SILICON APD HF2 1.064 μm PHOTORESPONSE SCANS

REPRODUCIBILITY OF THE
ORIGINAL PAGE IS POOR

FIGURE 26 RCA SILICON APD HF2 OUTPUT WAVEFORM

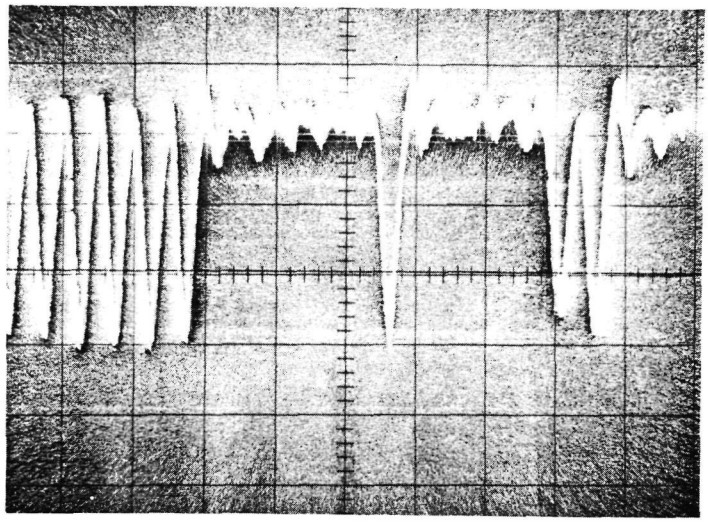

5 nsec/div
−438V BIAS
10 μA AVERAGE

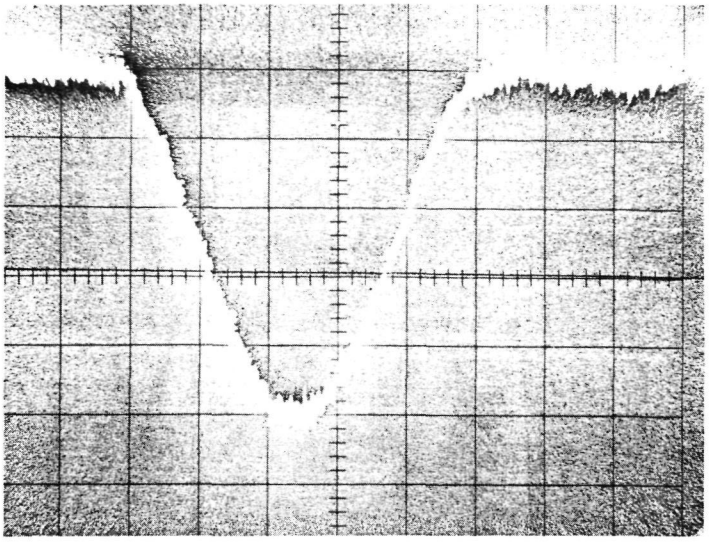

Cold
-346 V

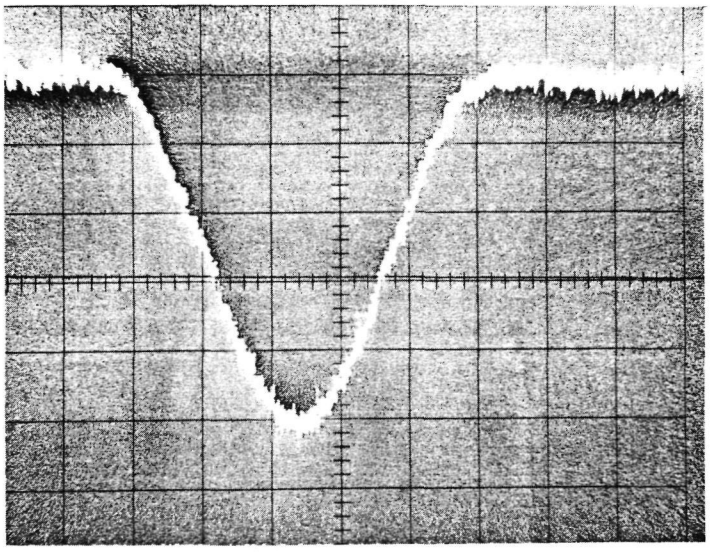

Hot
-442 V

Horizontal 500 ps/div
Vertical 1 mV/div

Figure 27 RCA Silicon APD HF2 Impulse Response

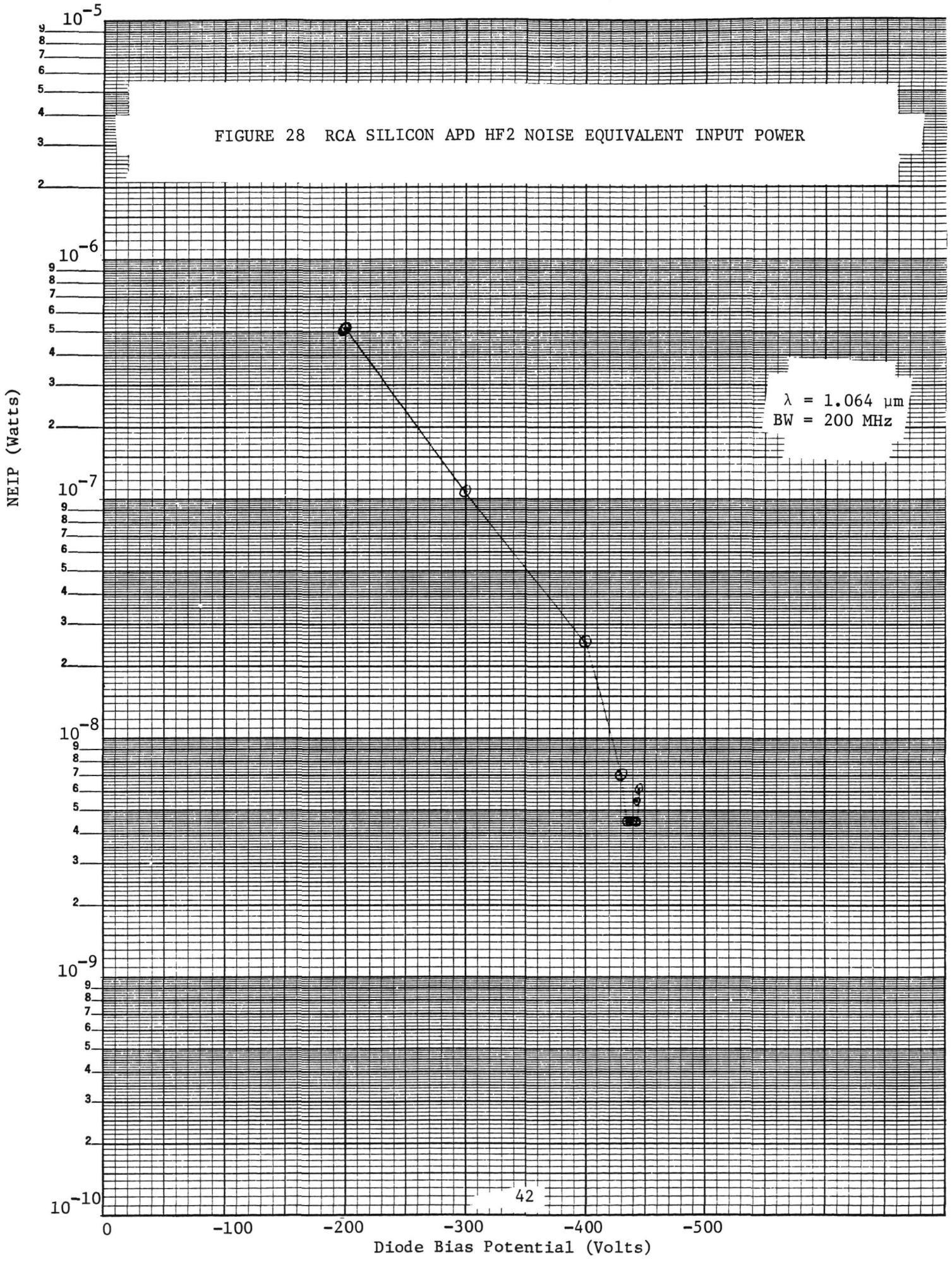
FIGURE 28 RCA SILICON APD HF2 NOISE EQUIVALENT INPUT POWER
λ = 1.064 μm
BW = 200 MHz
NEIP (Watts)
10^-5
10^-6
10^-7
10^-8
10^-9
10^-10
0
-100
-200
-300
-400
-500
Diode Bias Potential (Volts)
42

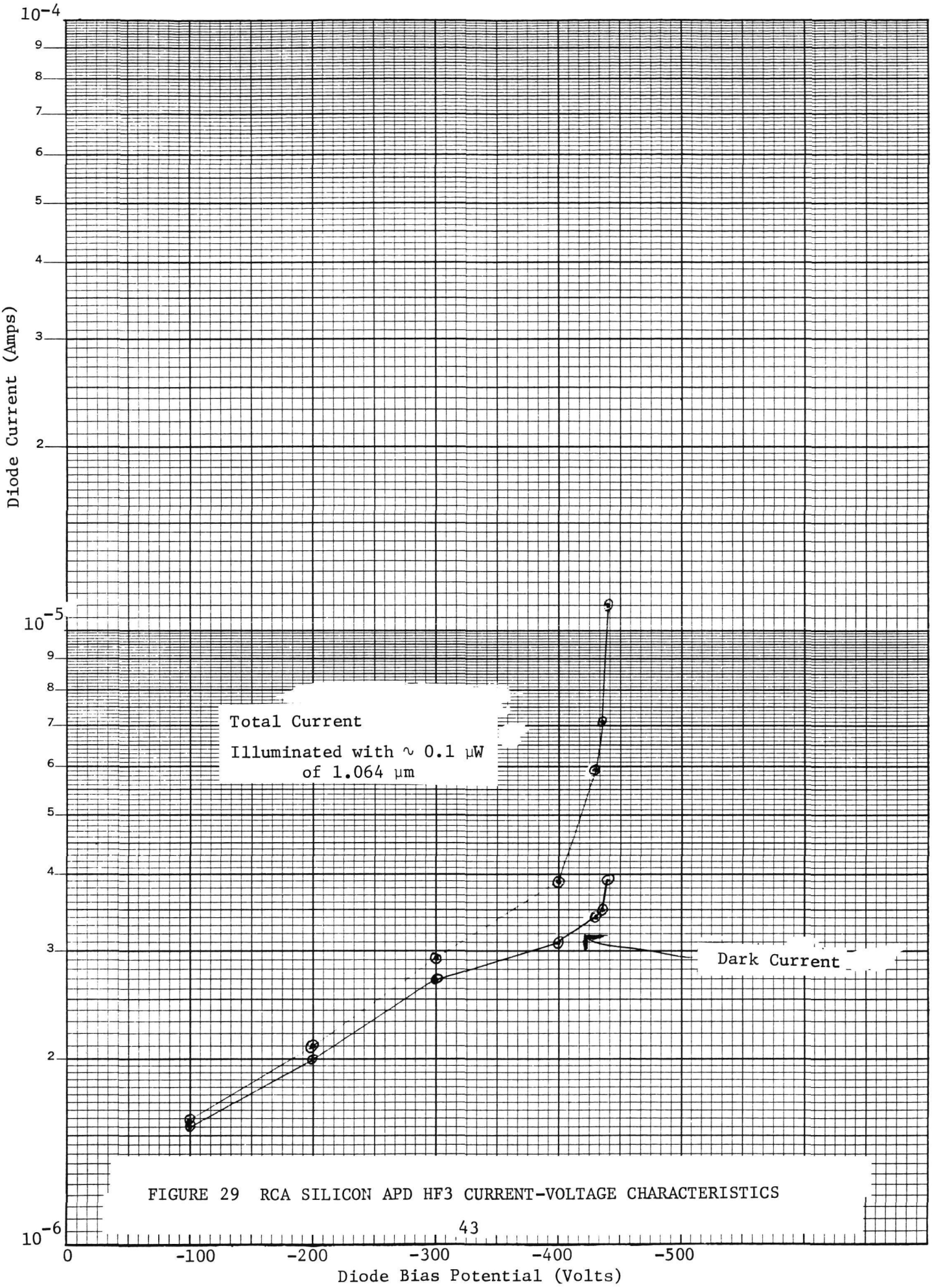

FIGURE 29 RCA SILICON APD HF3 CURRENT-VOLTAGE CHARACTERISTICS

Figure 30 shows the scanned photoresponse of detector HF3. Scans of the photocurrent and of the 200 MHz component of the photocurrent are shown. Response was uniform at a gain of 20. At a gain of 300, there was a 5 to 1 variation in response over the photosensitive area. Baseband response was identical to response at 200 MHz.

Figure 31 shows the output waveform of detector HF3. Modulator extinction ratio appeared degraded in this photo. The response was sufficiently fast to return to the baseline between adjacent pulses. Figure 32 shows the impulse response of detector HF3 at room temperature and at +80°C. In both cases the pulse width at the base was 2.7 ns.

Figure 33 shows a plot of NEIP versus applied bias for detector HF3. Optimum bias was -431V.

2.4 DISCUSSION OF PERFORMANCE

Table V shows the estimated and measured performance of the RCA detectors in communication system tests. The signal level required for 10^{-6} bit error rate was estimated from an analysis* prepared by R. J. McIntyre of RCA Limited. This comprehensive analysis considered the Poisson statistics of the signal, the extinction ratio of the transmitter modulator, the current gain of the detector, the variation of avalanche noise with current gain for these detectors, the required bit error rate, and the noise equivalent number of photoelectrons (per pulse) based on detector temperature and speed of response, and on preamplifier noise. The analysis showed that the optimum avalanche current gain had a shallow minimum between 200 and 400. Calculations used the quantum efficiency and current gain values of Table III even though these did not agree with measured responsivity values, because it was not certain whether the gain or the quantum efficiency was in error. Sample imperfections, such as measured dark current, were not considered in the analysis, and in that sense the treatment was idealized. The following assumptions were made for the calculation of estimated performance levels. Bit error rate = 10^{-6}. Transmitter modulator extinction ratio = 20 to 1. Preamplifier noise figure = 4.5 dB. Current gain = 300 for F and HF types. Current gain = 200 for DF types. The noise equivalent number of electrons (per pulse) = 7500 electrons into

* To be Published.

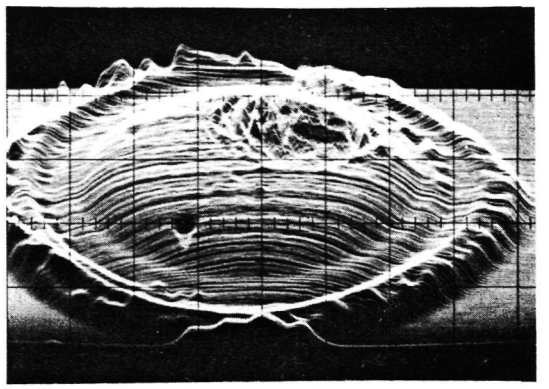

−100V
10 μw

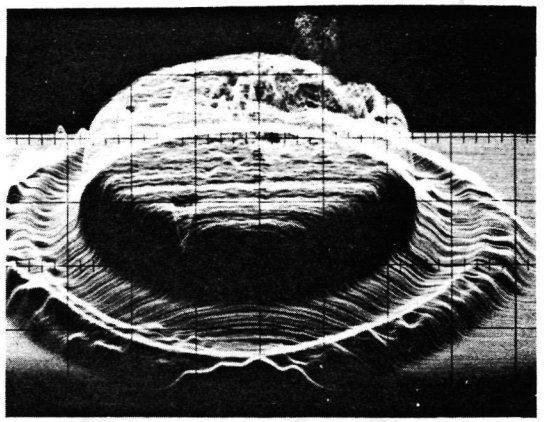

−120V
10 μw

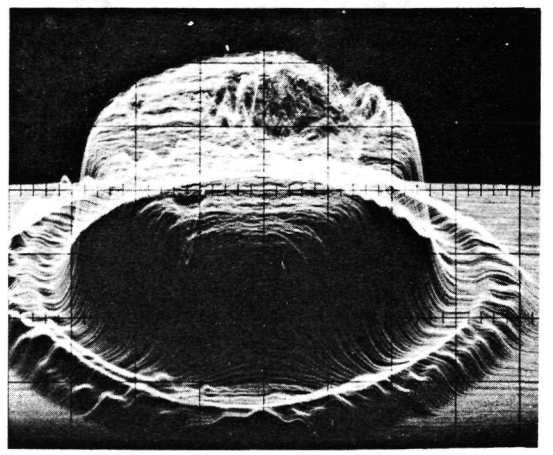

−150V
10 μw

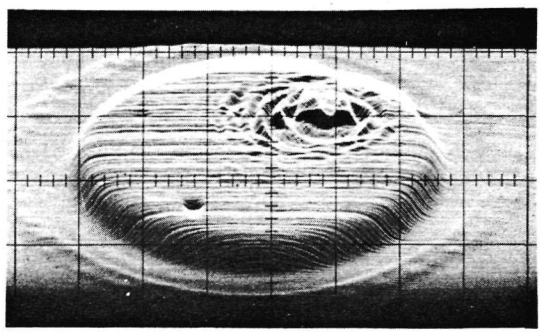

−250V
1 μw

DC

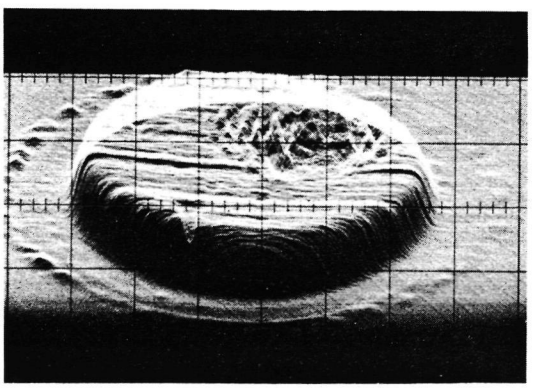

−200V
10 μw

200 MHz

FIGURE 30A RCA SILICON APD HF3 1.064 μm PHOTORESPONSE SCANS

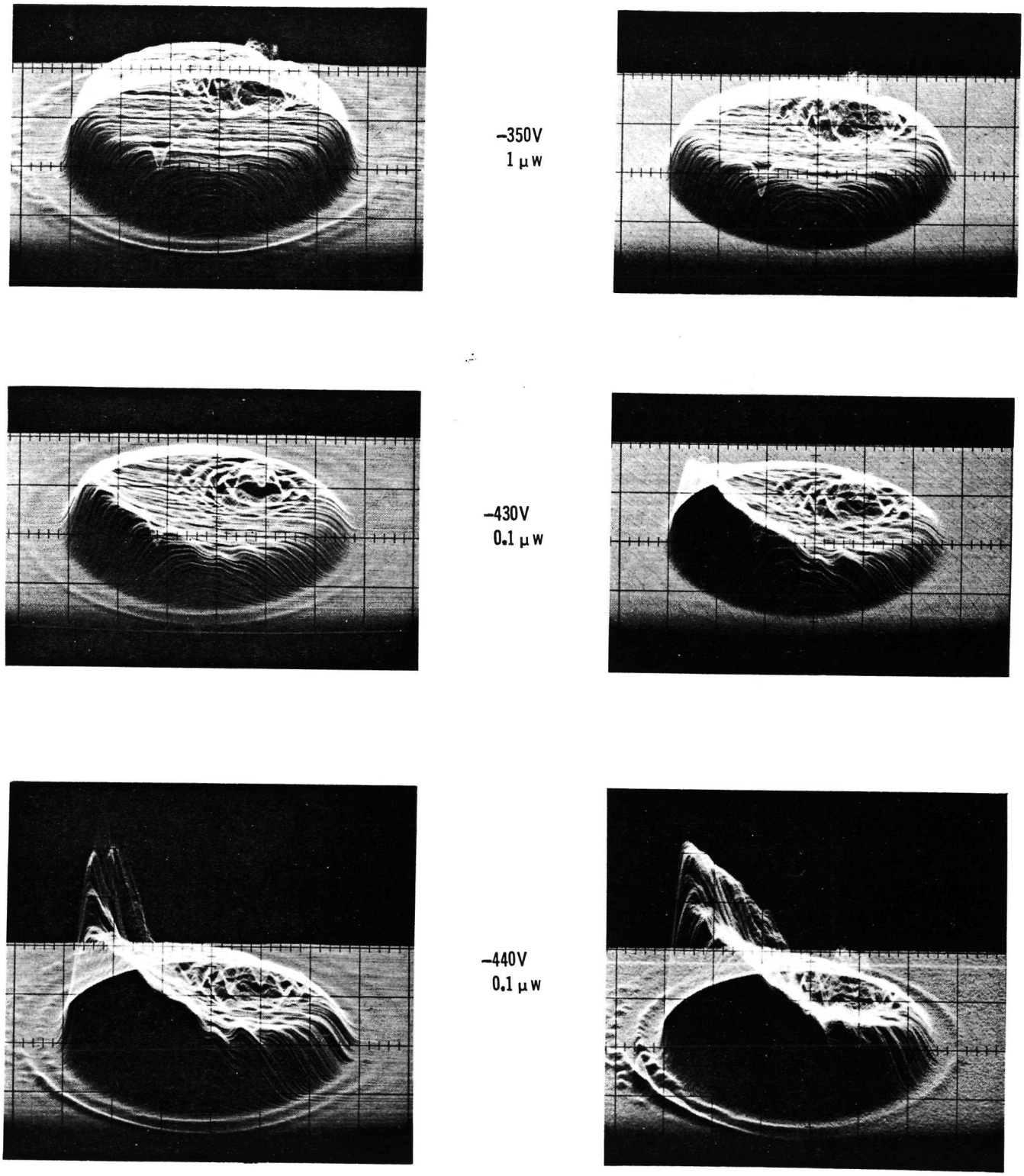

FIGURE 30B RCA SILICON APD HF3 1.064 μm PHOTORESPONSE SCANS

REPRODUCIBILITY OF THE
ORIGINAL PAGE IS POOR

FIGURE 31 RCA SILICON APD HF3 OUTPUT WAVEFORM

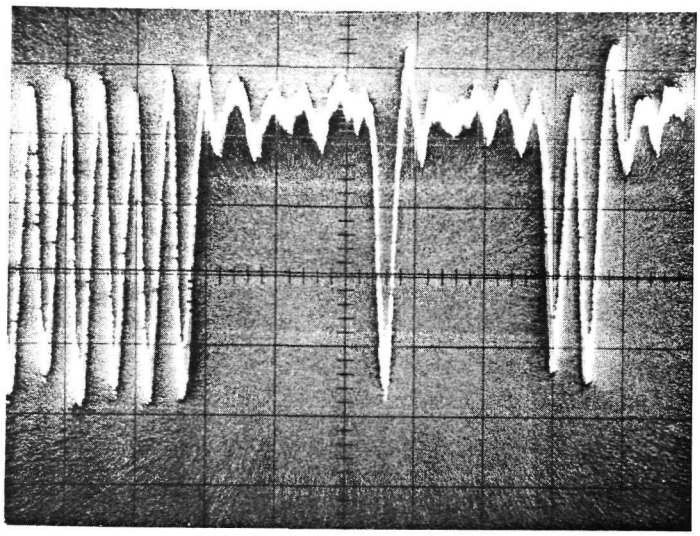

5 nsec/div
−432V BIAS
10 μA AVERAGE

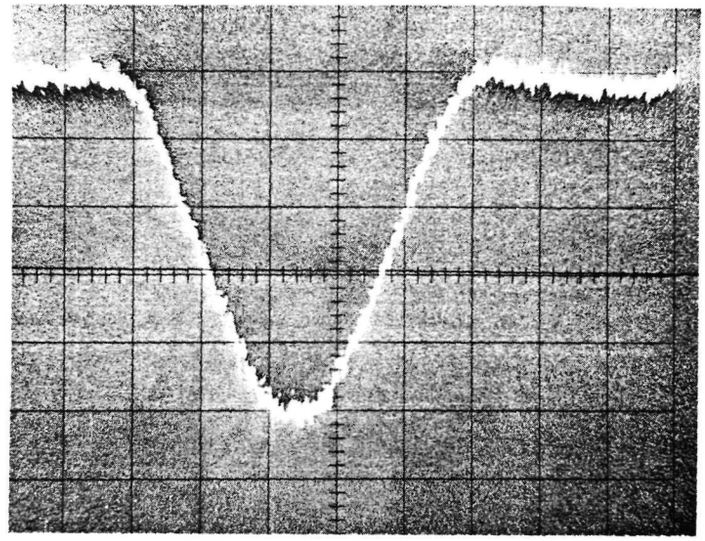

Cold
-335 V

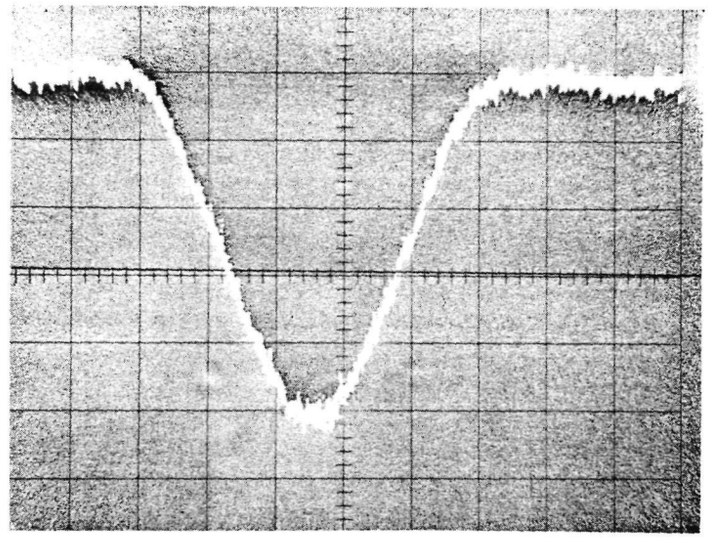

Hot
-437 V

Horizontal 500 ps/div

Vertical 1 mV/div

Figure 32 RCA Silicon APD HF3 Impulse Response

FIGURE 33 RCA SILICON APD HF3 NOISE EQUIVALENT INPUT POWER

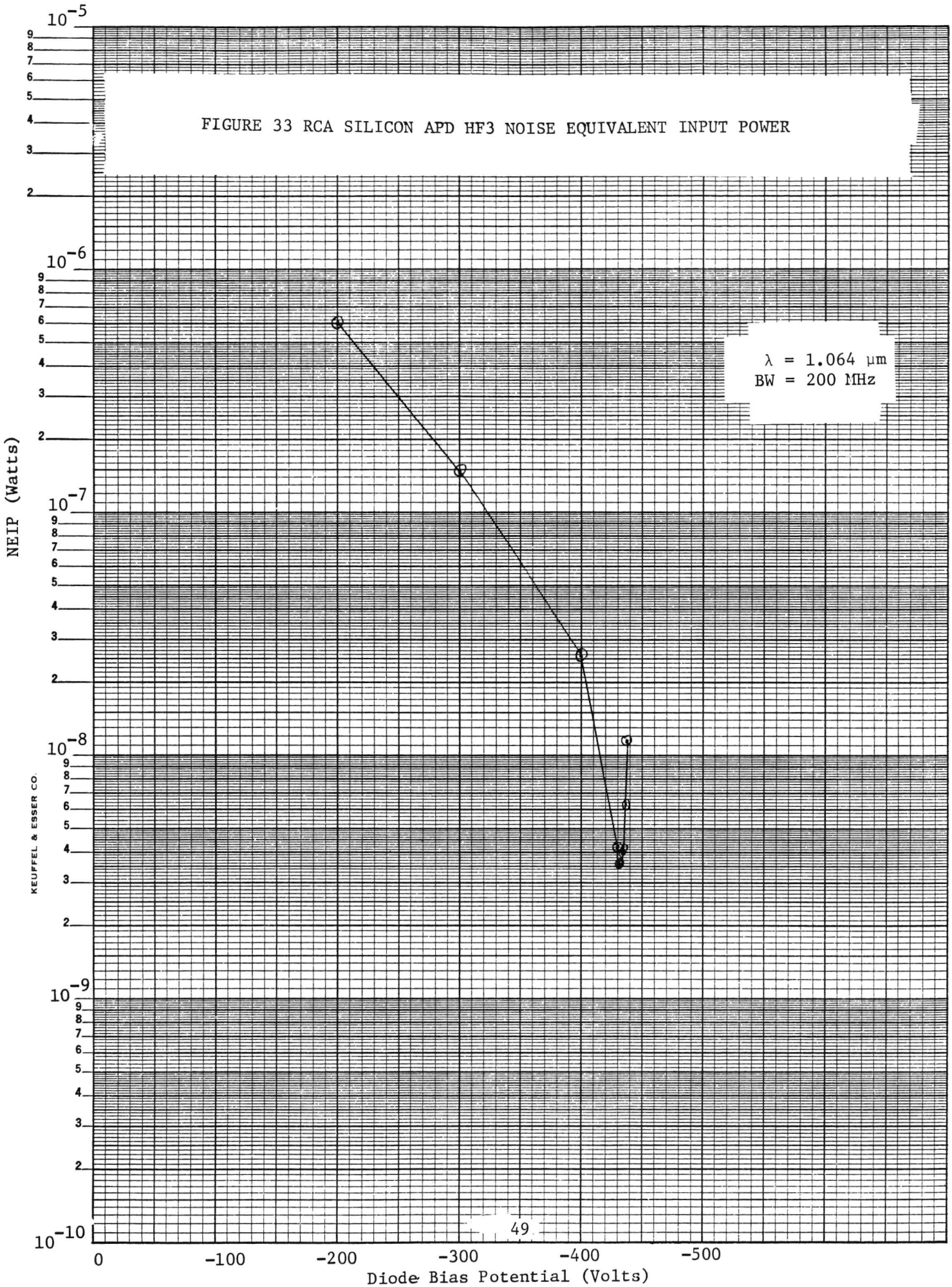

TABLE V

RCA Silicon APD Detector Performance Comparison

Detector	Signal For 10^{-6} Bit Error Rate		Comments
	Estimated Photons/Pulse	Measured Photons/Pulse	
F1	3199	4521	
F2	3199	4288	
DF1	2113	2807	
DF2	2113	2675	
		1581	Best Focused Spot
HF2	2008	3664	
HF3	2008	3117	

REPRODUCIBILITY OF THE
ORIGINAL PAGE IS POOR

the preamplifier. It is difficult to explain why DF2 operated so well with a very small spot. The performance was not explained by the somewhat higher gain observed. Perhaps the quantum efficiency was enhanced by etalon effects between the parallel faces of the silicon wafer. Note the interference patterns in the RCA detector photoresponse scans. Application of the normal antireflection coating will reduce and perhaps eliminate this interference.

The agreement between estimated and measured values was good. Looking at the best detector of each type, the measured values were an average of 1.4 dB poorer than theoretical.

The disagreement between responsivity values in Table III and Table IV is not understood. They may be due to differences between large and small focused spot measurements and to differences in ambient temperature which change the required bias voltage.

3. VARIAN PHOTOMULTIPLIER

3.1 DESCRIPTION

The VPM 152A detector manufactured by Varian LSE of Palo Alto is a high speed all electrostatic photomultiplier with beryllium copper dynodes and an externally processed indium gallium arsenide phosphide (InGaAsP) photocathode optimized for 1.064 μm. The internal cup and slat focusing structure does not inherently shield the cathode from the high level dynodes resulting in signal induced noise problems which degrade detector performance. The manufacturer has plans to add baffles intended to minimize this noise generation.

Quantum efficiency of the Varian detectors tested during this program was short lived. The final device received and tested during this program was stored and operated at -20°C and shipped in dry ice to maintain photoresponse. Operation at excessive anode current also adversely affected cathode life. Only the last of five devices tested had sufficient quantum efficiency to be competitive with the other detector types.

Devices designated S/N 027 and S/N 028 were 5 stage tubes. Devices designated S/N 029 and S/N 031 and S/N 035 were 6 stage tubes.

A compilation of data provided by the manufacturer appears in Table VI. The extremely low dark anode current of S/N 035 was attributed to very heavy scrubbing (operation at high output current while still on the vacuum station) prior to cathode insertion. This device also exhibited the best noise and system performance.

The earlier Varian detectors, including S/N 027, S/N 028, and S/N 029, incorporated a resistive dynode voltage divider string potted within the enclosure along with the PMT. The power dissipated in the divider chain warmed these devices noticibly. The cathodes degraded more rapidly at elevated temperature. The later Varian detectors, S/N 031,and S/N 035, had individual dynode leads and utilized an external resistive voltage divider chain to minimize the heating of the tube body. The diagram for operation of these detectors is shown in Figure 34.

TABLE VI

VARIAN LSE VPM 152A MANUFACTURER DATA

PMT	TEMPERATURE	QUANTUM EFFICIENCY	DYNODES	GAIN	DARK CURRENT
S/N 027	23°C		5	3000	.4 na
S/N 028	23°C	1.5%	5	3000	8 na
S/N 029	23°C	0.4%	6	12000	7 na
S/N 031	23°C	0.12%	6	9000	.5 na
S/N 035	-20°C	3.0%	6	3000	1 pa

3.2 BIT ERROR RATE TESTS

Communication system bit error rate test data for the Varian photomultiplier detectors is summarized in Table VII. The bit error rate curves of each detector are presented in Figure 35. These curves are a composite of the best data points observed under various modes of PMT operation and are plotted versus photocurrent to allow a comparison independent of photocathode quantum efficiency. Only scanty data was taken on the earlier devices since they were tested early in the program when the test set up was primitive and difficult to use. Quantum efficiency of all photomultiplier detectors degraded with operation. Only S/N 035 had sufficient photoresponse to compete with the photodiode detectors. S/N 035 was shipped with 3% quantum efficiency. The quantum efficiency was measured at 2.3% focused and 2.0% average before testing. The quantum efficiency during bit error rate testing was 2.17% at the best point, including the transmission loss through three uncoated windows (estimated transmission 72%). For bit error rate testing with alternative gain reduction methods performed later in the program, quantum efficiency had degraded to 1.22%. After return to the manufacturer for further testing, quantum efficiency had fallen to 0.7%. Total elapsed time for this drop was less than 2 months, all at -20°C or below.

The results of communication system bit error rate testing with S/N 031 are presented in Figure 36 and are plotted versus photocurrent for comparison with other detectors. Quantum efficiency during these tests was 0.11%. Low bit error rates could be obtained at reduced gain at the expense of high input signal levels. Gain was reduced by lowering the overall dynode chain potential.

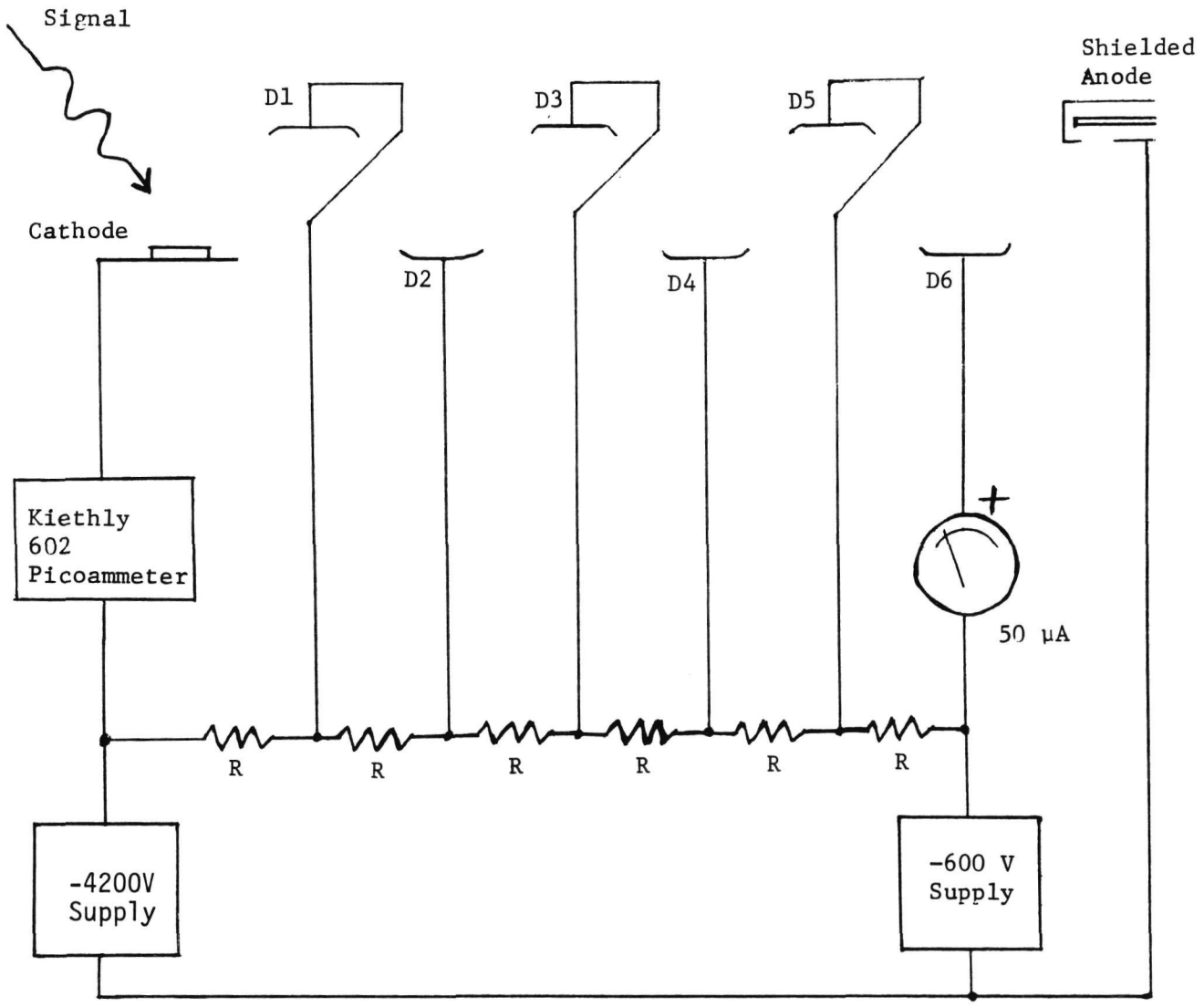

FIGURE 34 VPM 152A OPERATION WITH EXTERNAL DIVIDER

TABLE VII

VARIAN VPM 152A 400 Mbps PGBM COMMUNICATION SYSTEM TEST RESULTS

Detector	QE	FOR 10^{-6} BIT ERROR RATE			Comments
		1.064 μm Power	Photons/Pulse	Photoelectrons/Pulse	
S/N 027					QE too low for testing.
S/N 028	0.012%	81000 nW	2.17×10^{6}	249	
S/N 029	0.09%	4500 nW	1.2×10^{5}	108	For BER = 2×10^{-6}
S/N 031	0.11%	6000 nW	1.6×10^{5}	177	Reduced gain
S/N 035	2.17%	213 nW	5704	124	Reduced gain (-20°C)

Figure 35 VPM 152A Bit Error Rate Data

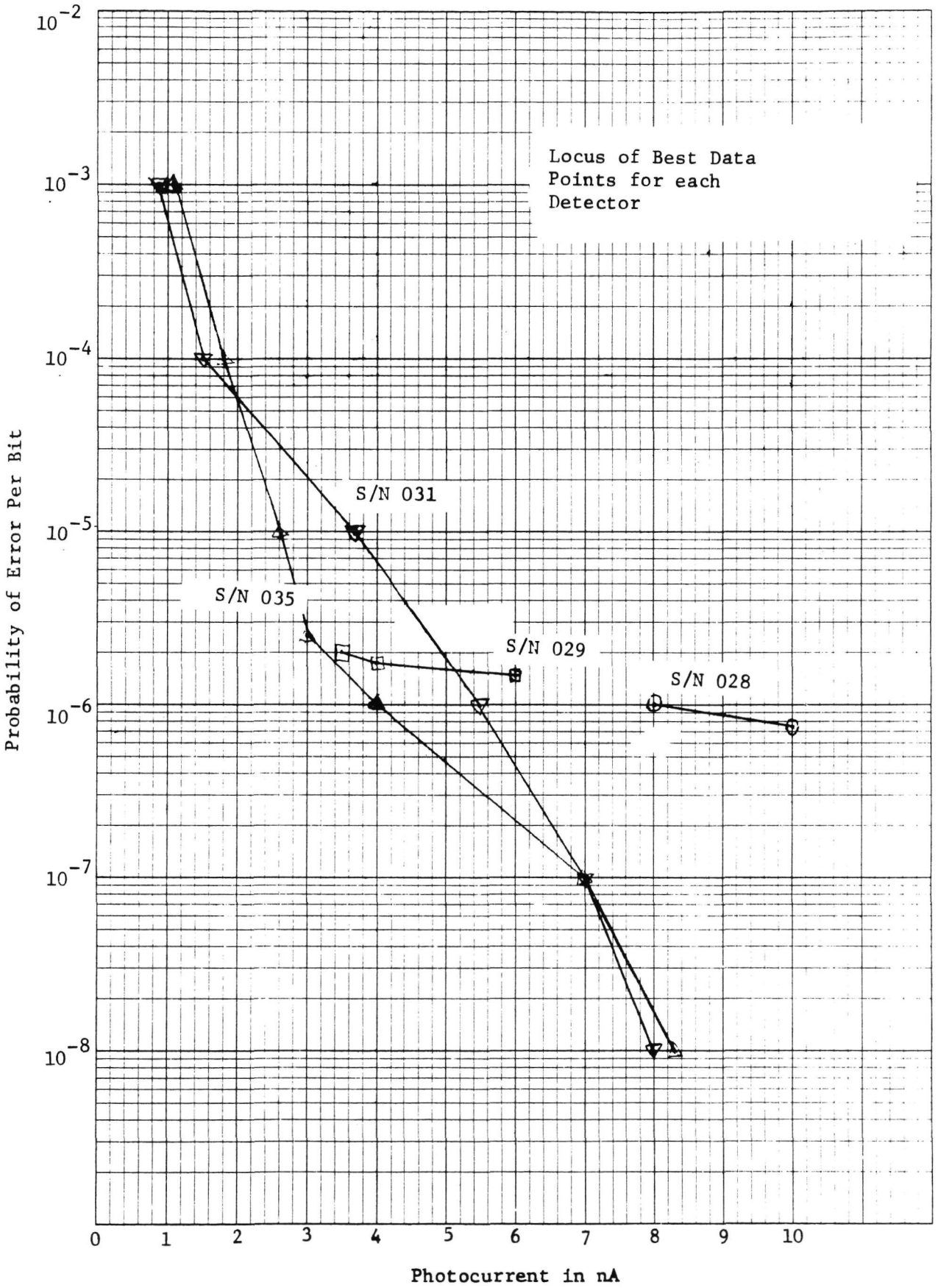

Figure 36 VPM 152A S/N 031 Bit Error Rate Data

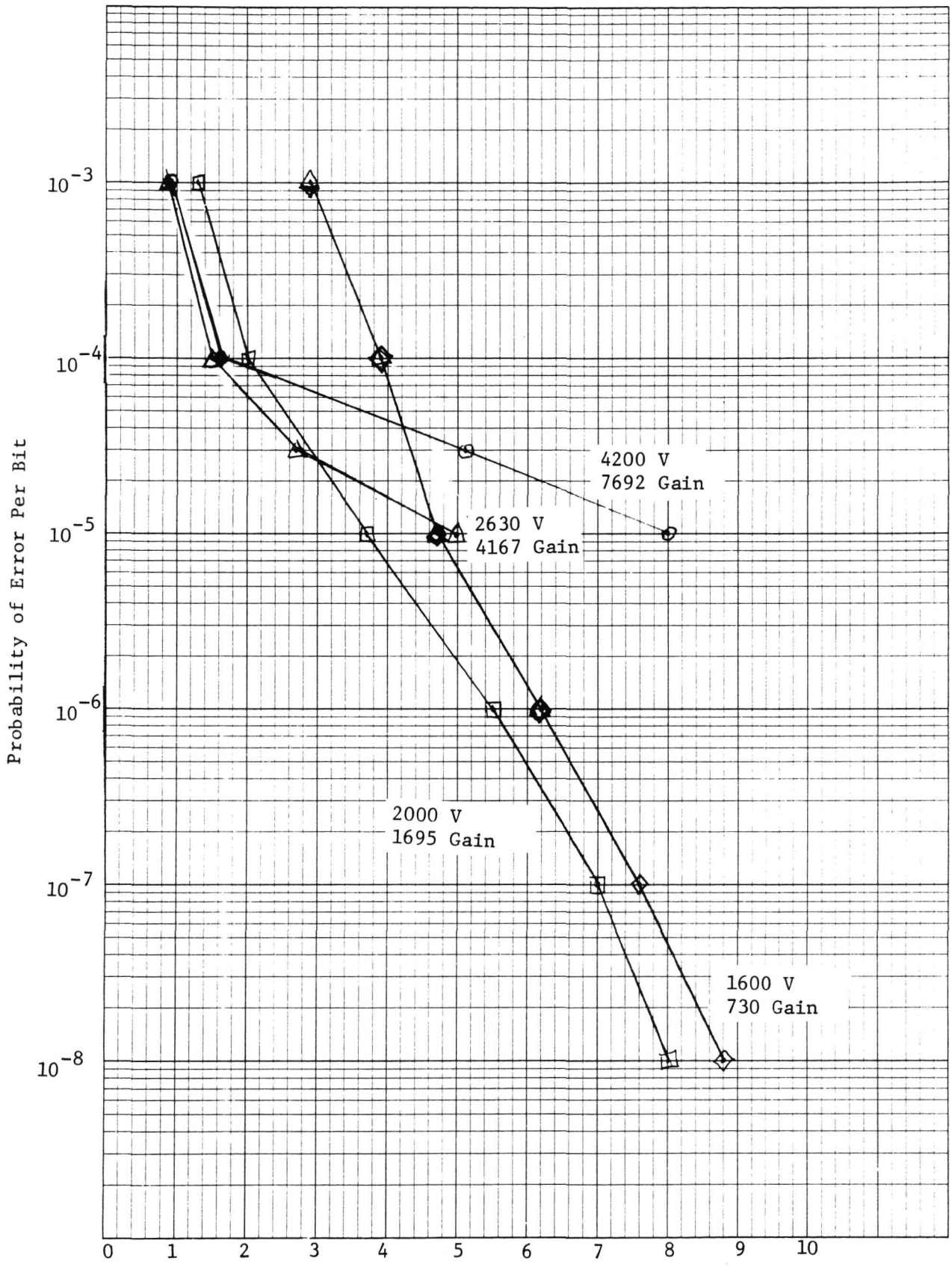

The results of communication system bit error rate testing with S/N 035 are presented in Figure 37 and are plotted versus photocurrent because quantum efficiency degraded in the course of testing. At high gain, the signal induced noise limited the bit error rates attainable. At reduced gain, lower errors were attainable. Two methods of gain reduction were employed. Reduction of gain by lowering overall dynode chain potential, with dynode 6 potential held at -600V, resulted in the curves for gain values of 1235, 806, and 323. (Dick Enck of Varian has since observed that the dynode 6 potential should have been lowered proportionally with cathode potential to maintain electron optic alignment. Reduction of gain by bringing dynode 1 closer to cathode potential as shown in Figure 38 resulted in the curve of gain value of 1040. This latter resulted in the best 10^{-6} BER data point and is plotted separately in Figure 39 versus input optical power. Quantum efficiency for this measurement was 2.17%.

3.3 UNIT TESTS.

Only devices S/N 031 and S/N 035 were completely evaluated. The latter because it was the best delivered detector of this type, and the former because it was very noisy and allowed characterization testing of the noise mechanism.

3.3.1 Five Stage Photomultiplier S/N 027.

VPM 152 S/N 027 had a current gain of 3×10^3 and a dark anode current of 0.5 nA. Cathode quantum efficiency was too low for use in the communication system test bed.

Figure 40 shows the output waveform of detector S/N 027. Pulse width at the 10% of maximum points was less than 600 ps.

3.3.2 Five Stage Photomultiplier S/N 028.

VPM 152 S/N 028 had a dark anode current of 0.4 nA and a measured current gain of 2×10^3, one-third lower than measured by the manufacturer.

Figure 41 shows the scanned photoresponse of detector S/N 028. Displacement from the baseline is proportional to detected current at each point. The 1.064 μm signal input is modulated at 200 MHz. Scans of detected cathode

FIGURE 37 VPM 152A S/N 035 BIT ERROR RATE DATA

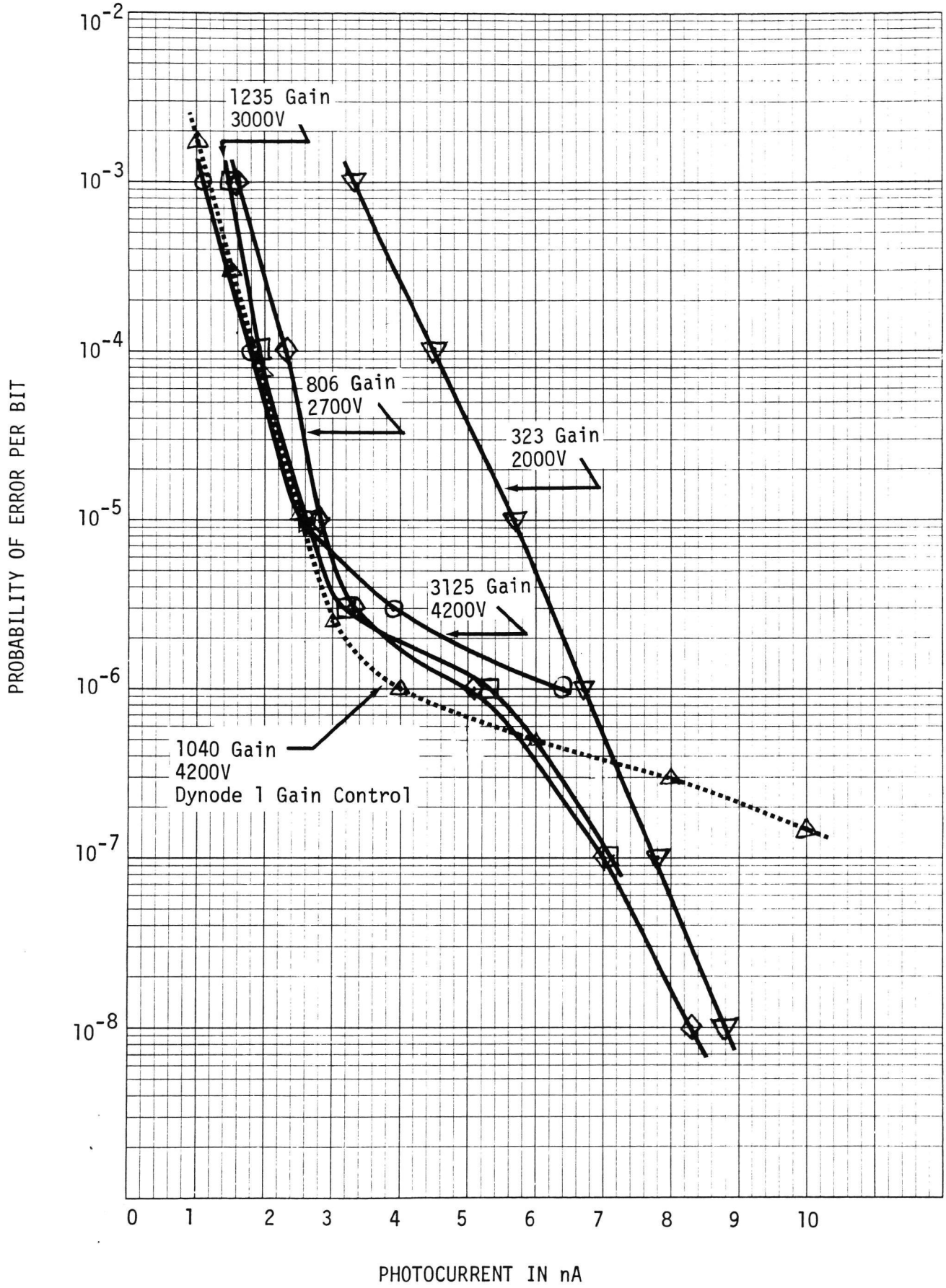

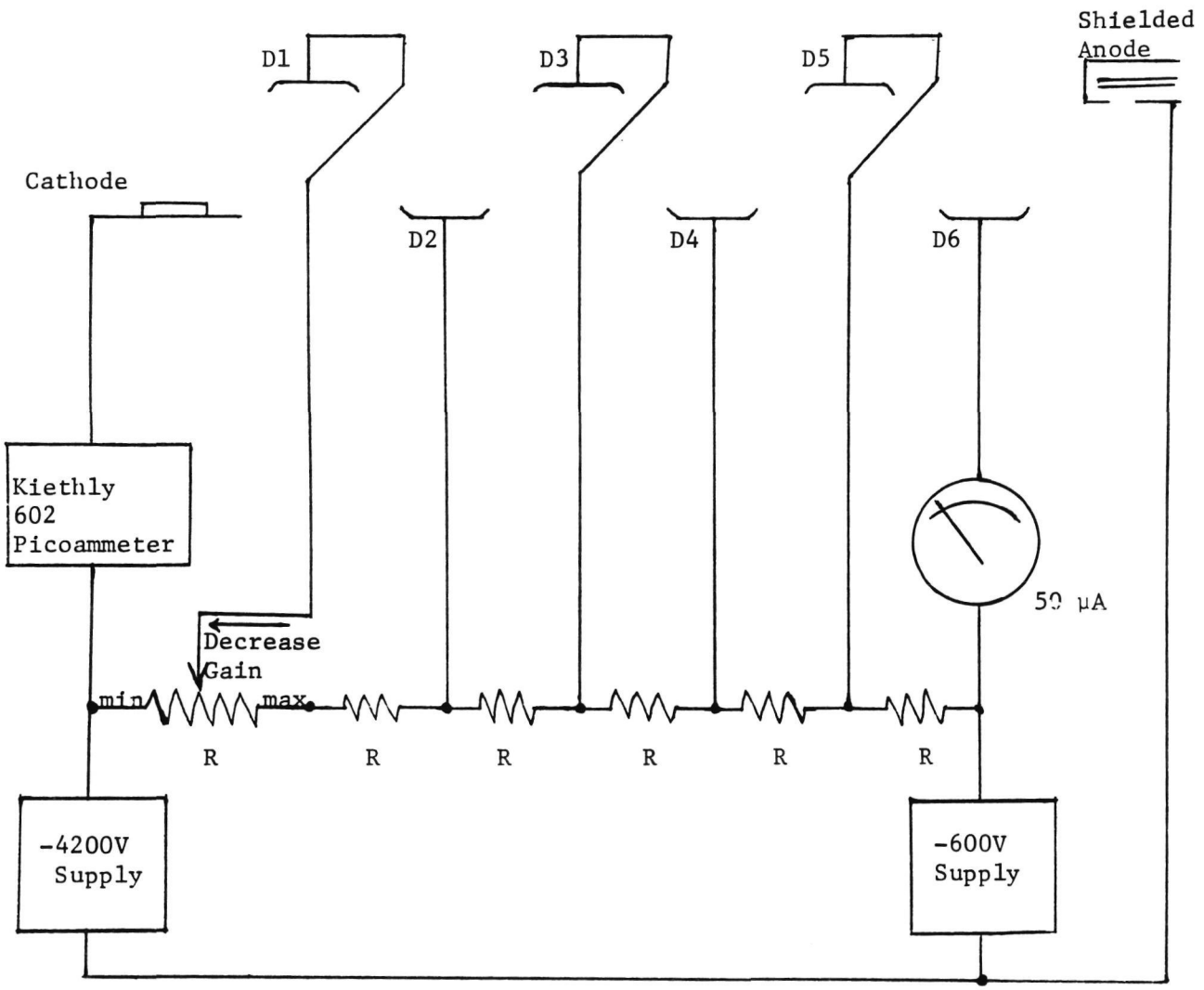

VPM 152A GAIN REDUCTION WITH DYNODE 1 POTENTIAL

FIGURE 38

FIGURE 39 VPM 152A S/N035 BIT ERROR RATE DATA

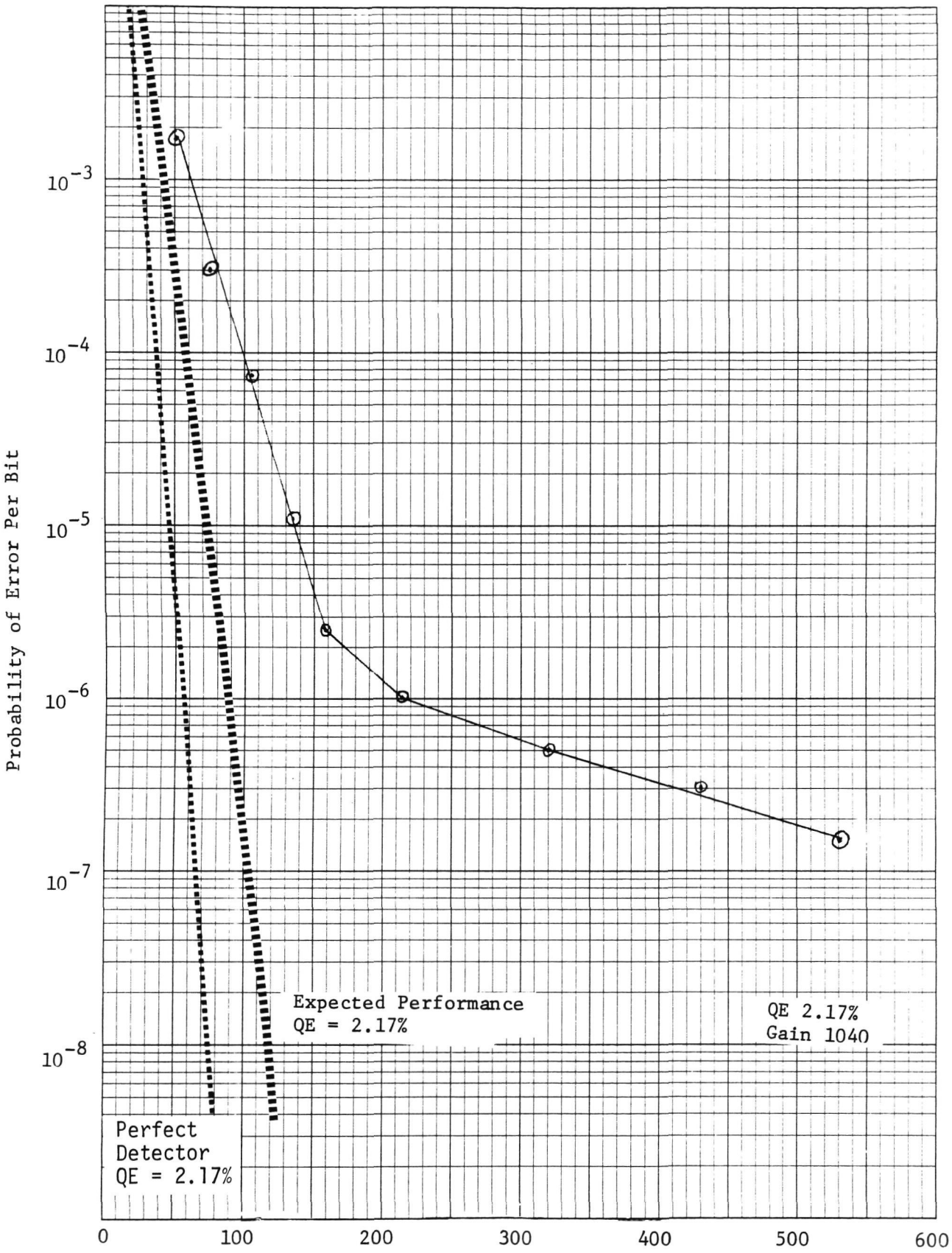

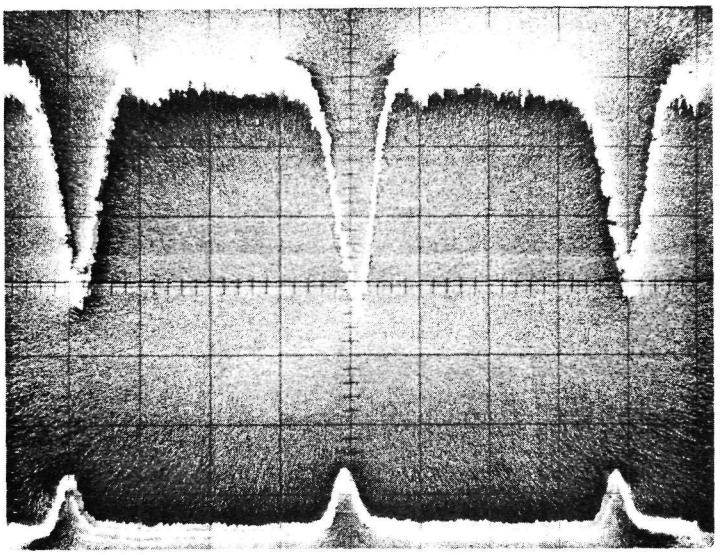

2mV/div
500ps/div
i_{anode}=25 μA

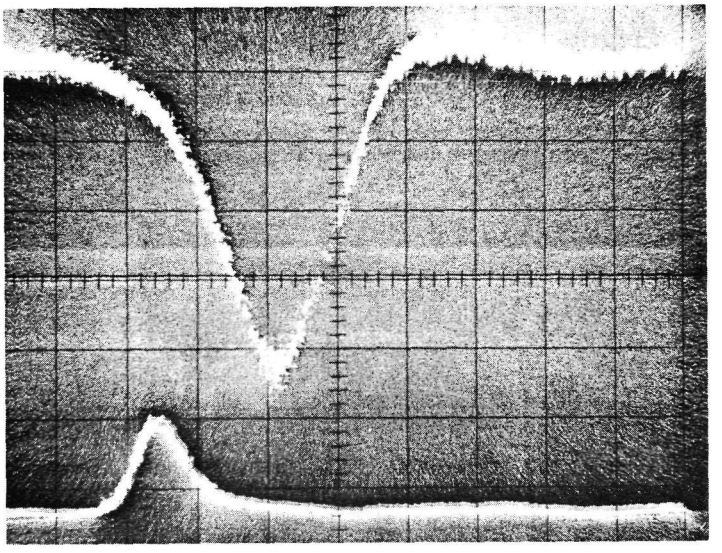

2mV/div
200ps/div
i_{anode}=35 μA

FIGURE 40 VPM 152A S/N027 OUTPUT WAVEFORMS

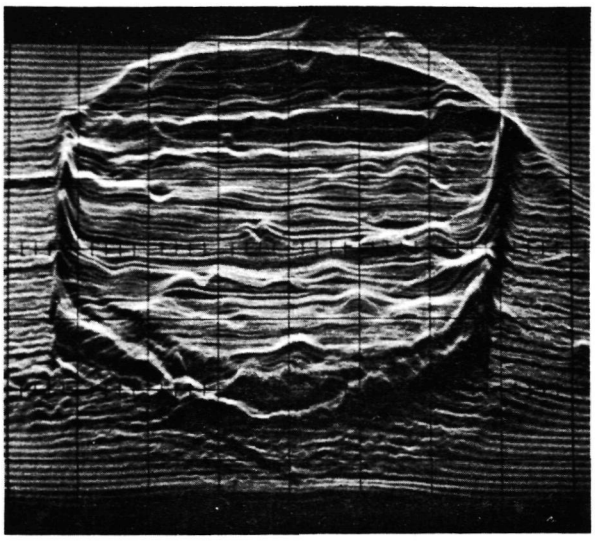

CATHODE
PHOTORESPONSE

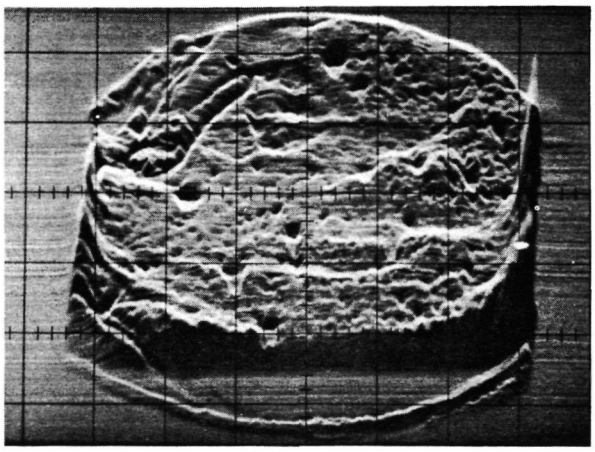

ANODE DC
RESPONSE

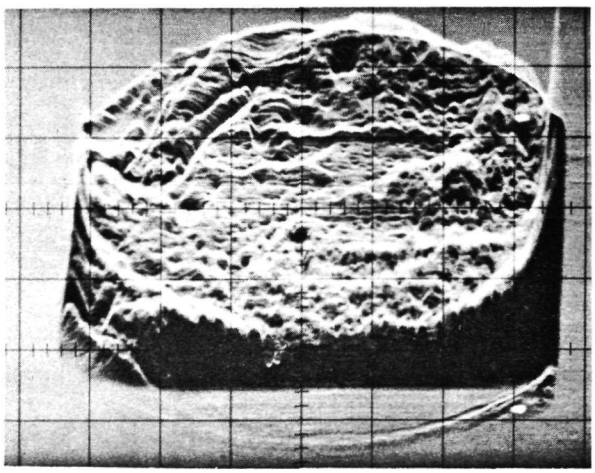

ANODE
200 MHz
RESPONSE

FIGURE 41 VPM 152A S/N028 1.064 μm PHOTORESPONSE SCANS

current and detected anode current are shown. A comparison between these shows variation in secondary current gain as a function of signal position on the cathode. A scan of the 200 MHz component of the anode signal (amplified, filtered, and square law detected) is shown which allows comparison between the baseband (dc) gain and the gain at 200 MHz as a function of cathode position. Increased detail is seen in the anode scans, partially due to improved signal to noise ratio of the measurement, and partially due to variations in dynode gain with position.

Figure 42 shows the output waveform of detector S/N 028. Pulse width at the 10% of maximum points was less than 650 ps.

Noise equivalent input power was measured at 1.36 μW in a 200 MHz bandwidth. Quantum efficiency for this measurement was 0.017%.

3.3.3 Six Stage Photomultiplier S/N 029.

VPM 152 S/N 029 had a dark anode current of 7 nA and a measured current gain of 1.1×10^4. Quantum efficiency during testing was 0.012%.

Figure 43 shows the output waveform of detector S/N 029. Pulse width at the 10% of maximum points was less than 850 ps. Response of the six stage tubes was noticibly slower than that of the 5 stage tubes above, however both were sufficiently fast to use in a 1 Gbs communication system.

3.3.4 Six Stage Photomultiplier S/N 031.

VPM 152 S/N 031 had a measured dark anode current of 180 pA at a measured current gain of 7.7×10^3. Photocathode quantum efficiency during testing was 0.11%.

Figure 44 shows the scanned photoresponse of detector S/N 031. Scans of cathode current, anode current, and the 200 MHz component of the anode current are shown. These scans show a dead band across the bottom of the cathode from which photoelectrons did not contribute to the output even at the recommended operating bias of -4200V. Response at 200 MHz was identical to response at baseband.

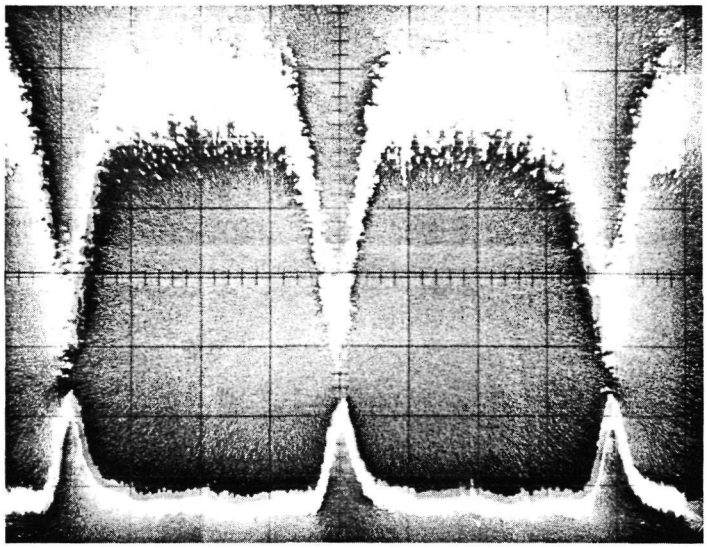

~1mV/div
500ps/div
i_{anode}=14 μA

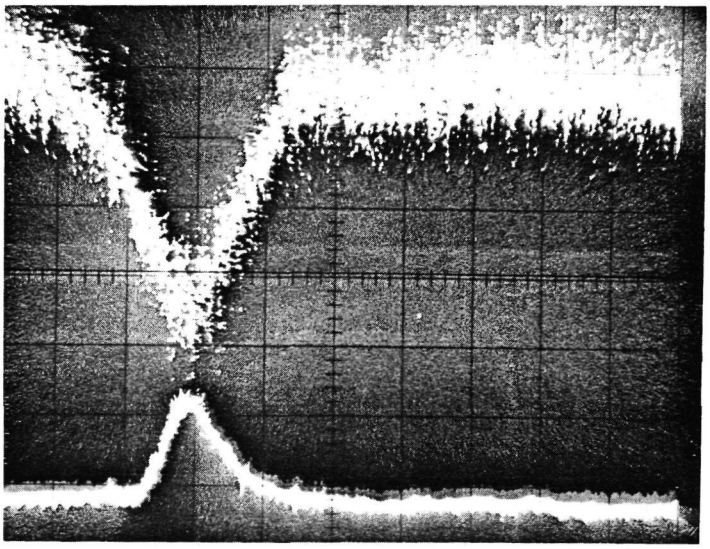

~1mV/div
200ps/div
i_{anode}=14 μA

FIGURE 42 VPM 152A S/N028 OUTPUT WAVEFORMS

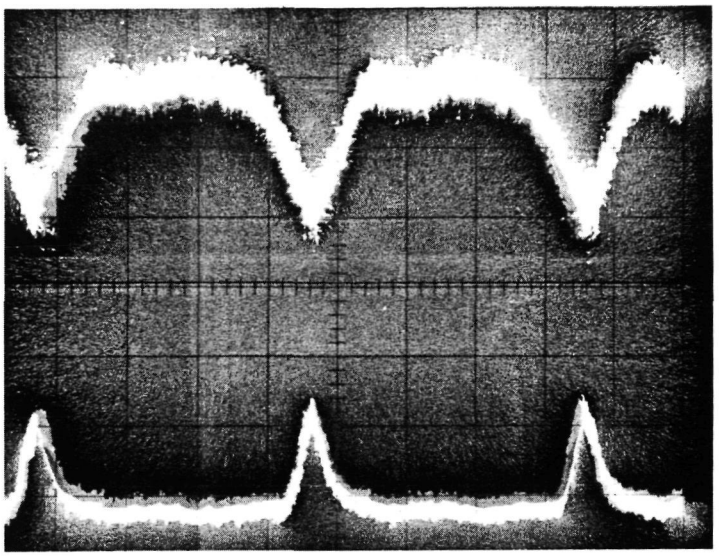

2mV/div
500ps/div
i_{anode}=27 μA

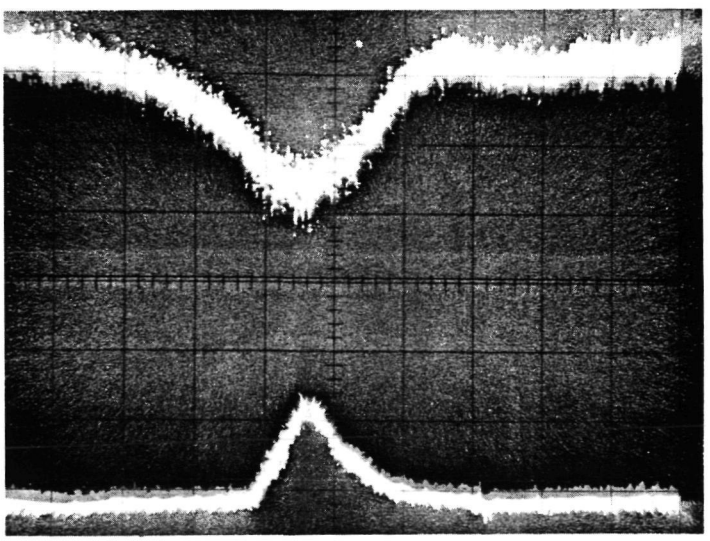

2mV/div
200ps/div
i_{anode}=28 μA

REPRODUCIBILITY OF THE
ORIGINAL PAGE IS POOR

FIGURE 43 VPM 152A S/N029 OUTPUT WAVEFORMS

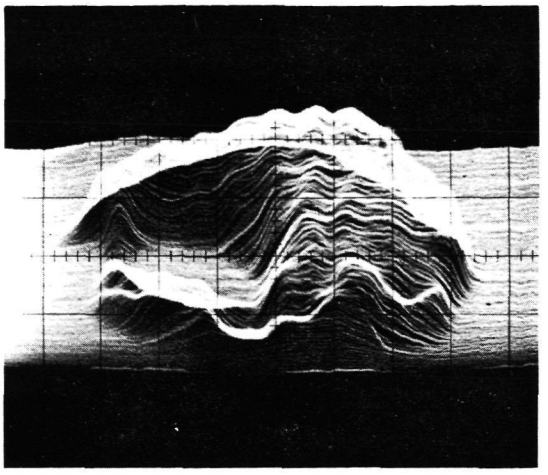

Cathode

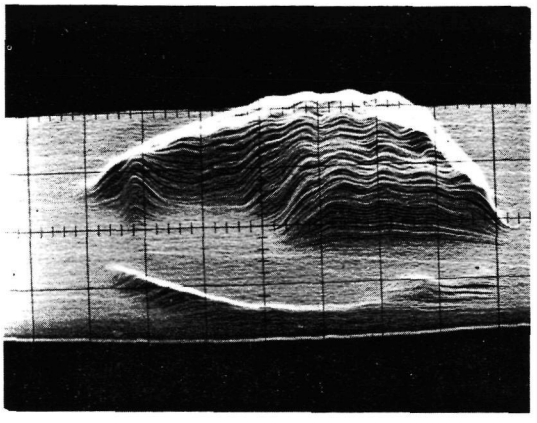

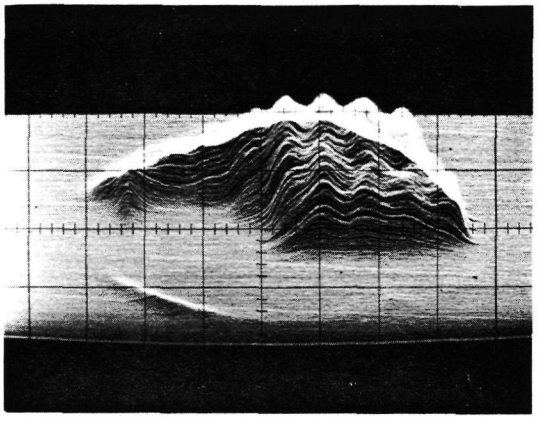

-2000V

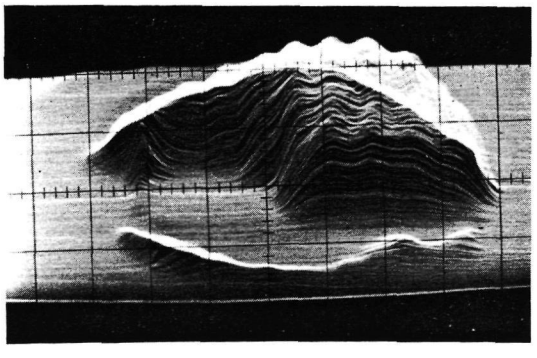

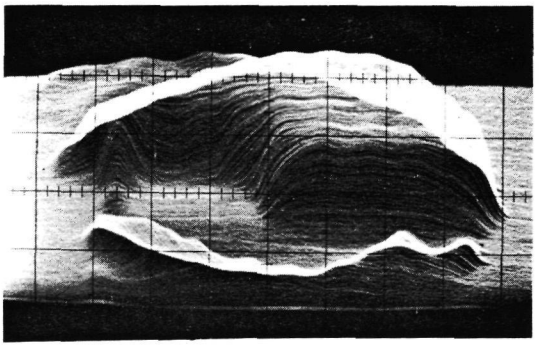

-4200V

dc

200 MHz

Figure 44 VPM 152A S/N 031 1.064 μm Photoresponse Scans

Figure 45 shows the output waveform of detector S/N 031 in response to the encoded transmitter signal. At the recommended operating potentials, noise pulses induced by signal are apparent. At reduced gain, the noise is not apparent and the speed of response is slowed somewhat. Figure 46 shows the impulse response of detector S/N 031. Pulse width at the 10% of maximum points was 750 ps with a 10% tail (post pulse) extending for an additional 500 ps.

Noise equivalent input power with zero background was measured to be 2.9 nW in a 200 MHz bandwidth.

3.3.5 Six Stage Photomultiplier S/N 035.

VPM 152 S/N 035 had a measured anode dark current of only 6.2 pA at a measured gain of 2.6×10^3. Photocathode quantum efficiency during testing was 2.17%.

Figure 47 shows the scanned photoresponse of detector S/N 035. Scans of cathode current, anode current, and the 200 MHz component of the anode current are shown. The gain at baseband was the same as the gain at 200 MHz, and both were uniform. All portions of the cathode contributed to the output. These scans are technically inferior to previous scans because the tube was mounted in a cooling enclosure with two additional uncoated windows. Interference effects were responsible for the observed waviness.

Figure 48 shows the output waveform in response to the encoded transmitter signal. The response was sufficiently fast to return to the baseline between adjacent pulses. A post pulse slowed the fall time and contributed to inter-symbol interference. The impulse response should be the same as that of S/N 031.

Noise equivalent input power was measured at 11.8 nW in a 200 MHz bandwidth. This value is over 500 times too high due to some unresolved error in the measurement.

3.4 NOISE MEASUREMENTS.

An effort was made to characterize the noise mechanisms in the VPM 152 to aid in reducing such effects in the future. S/N 031 was an exceptionally noisy tube and served well for such measurements. S/N 035 was very much quieter and yet still suffered from what was assumed to be similar phenomena.

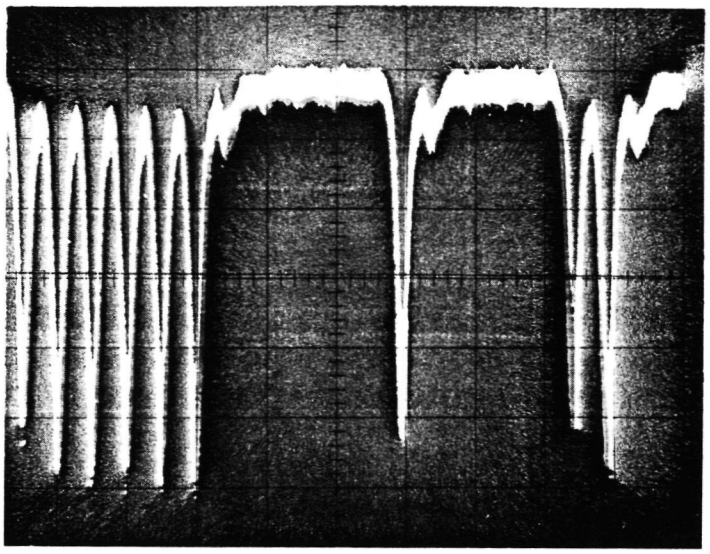

gain = 1700
-2000V cathode
- 600V dynode 6

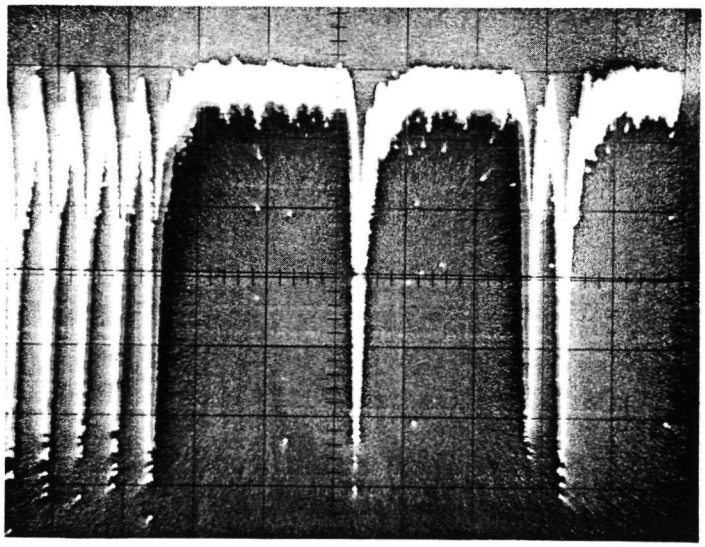

gain = 7700
-4200V cathode
- 600V dynode 6

horizontal 5 nsec/div

FIGURE 45 VPM152A S/N031 WAVEFORM SHOWING SIGNAL INDUCED NOISE AT HIGH GAIN

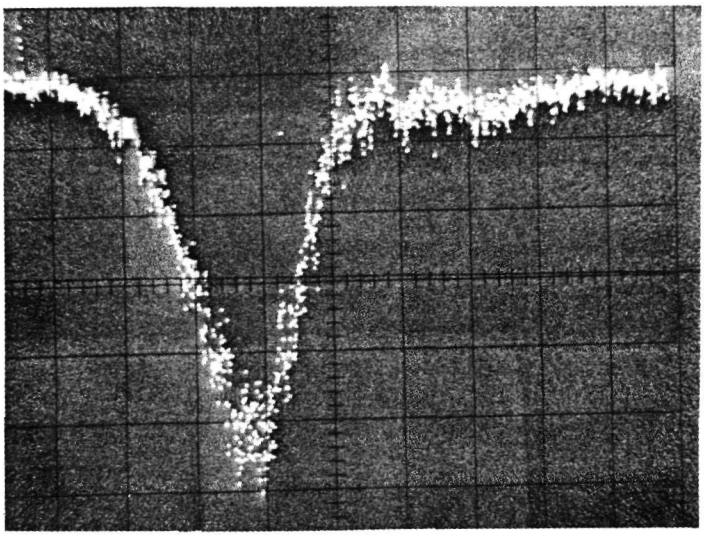

-600 V

-4200 V

Horizontal 200 ps/div

Vertical 1 mv/div

Figure 46 VPM 152 S/N 031 Impulse Response

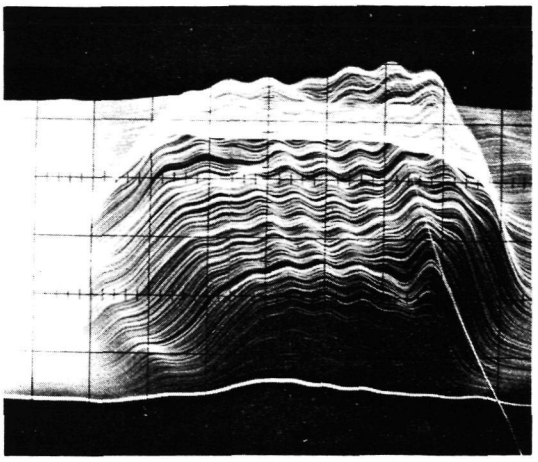

Cathode Response

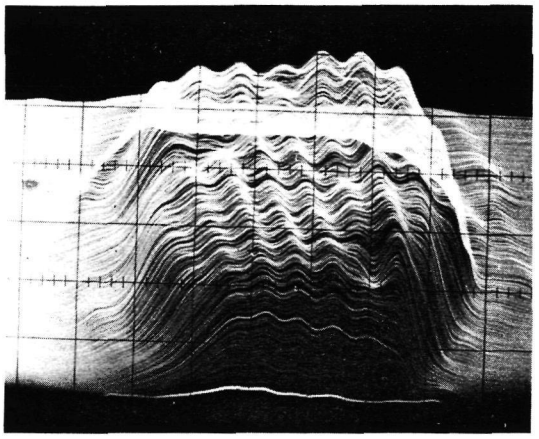

Anode Response

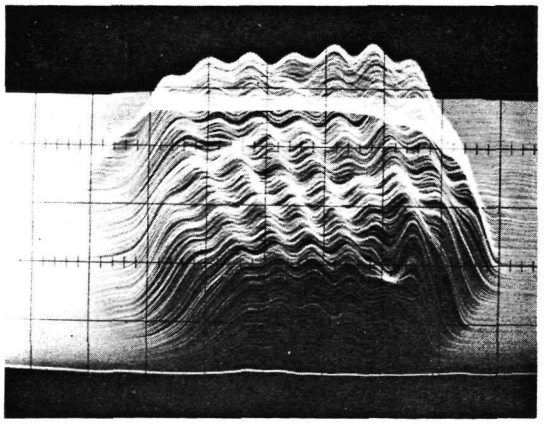

200 Mhz Anode Response

FIGURE 47 VPM152A S/N035 1.064 μm PHOTORESPONSE SCANS

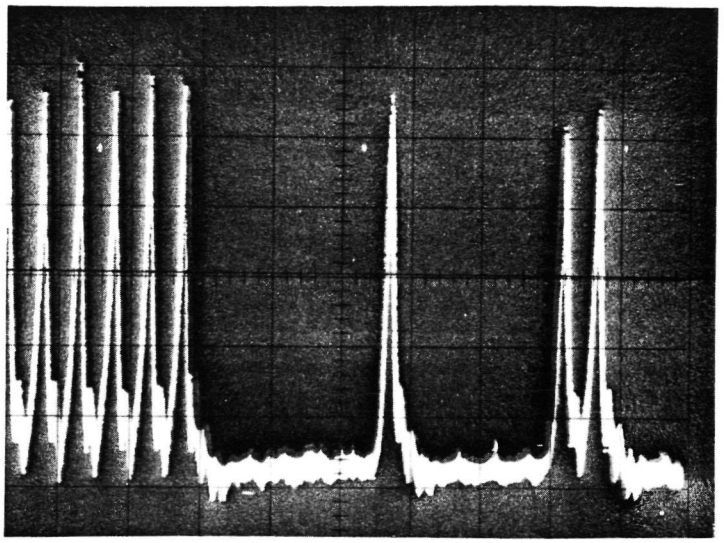

5 ns/div

FIGURE 48 VPM 152A S/N035 WAVEFORM (INVERTED)

3.4.1 S/N 031 Signal Induced Noise.

The measurement set up shown in Figure 49 was utilized to measure the amplitude distribution of noise pulses which occurred in response to a CW signal. The detector output was amplified and input to a high speed threshold detector. The threshold detector output toggled a flip-flop in order that the errors (÷2) could be counted by a conventional counter of moderate speed. A quiet tube should have Poisson behavior which would result in a linear representation when plotted on semilogarithmic paper. A noisy tube would have an abnormally large number of high amplitude pulses above that expected from the Poisson distribution on the input signal.

Figure 50 shows the distribution of pulses at the output of S/N 031 operated at rated gain in response to CW illumination of the cathode. The behavior was limited by noise in signal (Poisson) below the 3 mV threshold level. Above the 4 mV threshold level a broad skirt of signal induced noise pulses was apparent. These large noise pulses were up to several times larger than the expected signal distribution and caused excessive "zero" errors and required the threshold detector level to be set to an abnormally high level in communication system tests.

Figure 51 shows the distribution of signal induced noise pulses plotted as a function of delay time following an initiating optical pulse. The time dependence of noise pulse occurence showed broad maxima which peaked 0.5 to 0.8 μs after the end of the initiating optical pulse.

3.4.2 S/N 035 Signal Induced Noise

Figure 52 shows the distribution of pulses at the output of S/N 035 operated at rated gain and 1/2 gain in response to CW illumination of the cathode. The deviation from linearity was small, especially at reduced gain. The reduced gain curve taken at 15 μA is readily compared to the curve of S/N 031 in Figure 50 taken at 12 μA. The latter had more noise in the linear region at low threshold levels due to the higher gain and, therefore, lower photocurrent level.

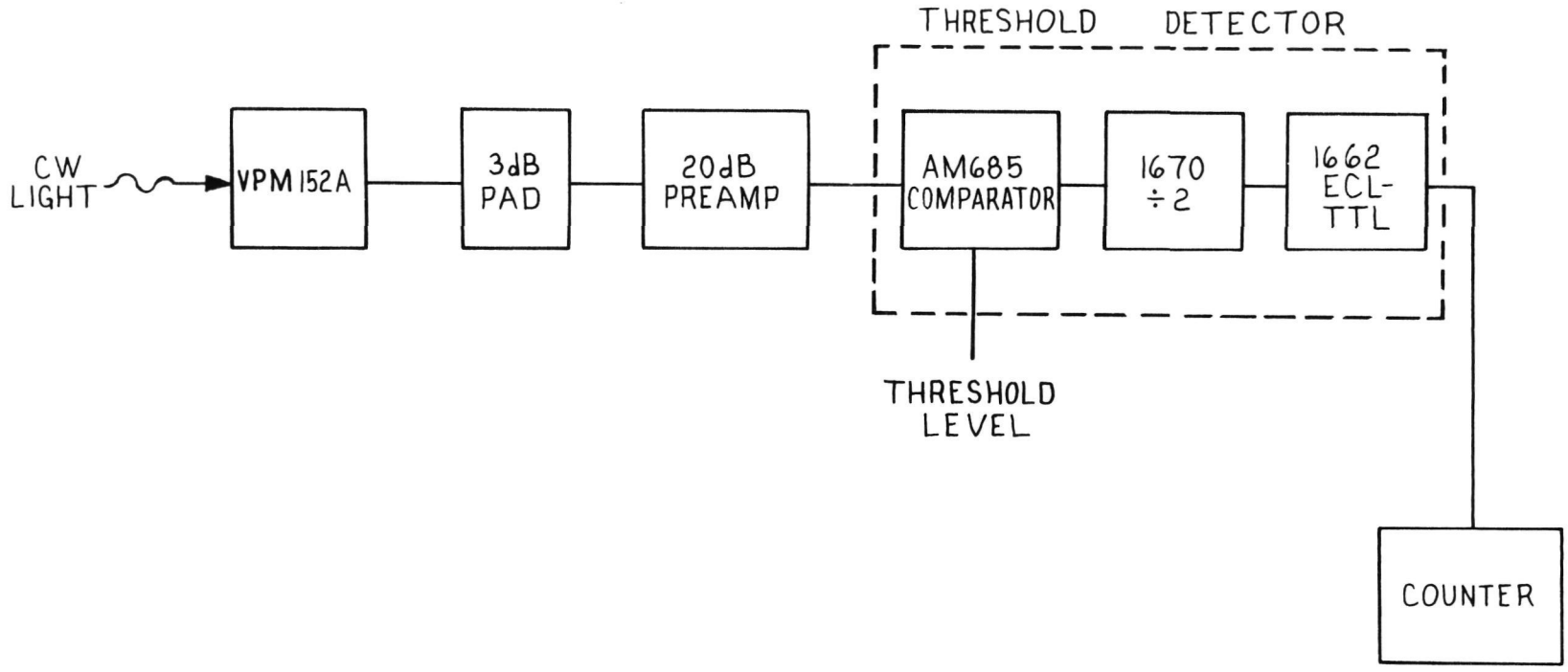

SIGNAL INDUCED NOISE PULSE MEASUREMENT SETUP

FIGURE 49

Figure 50 VPM 152A S/N 031 Signal Induced Noise Pulse Profile

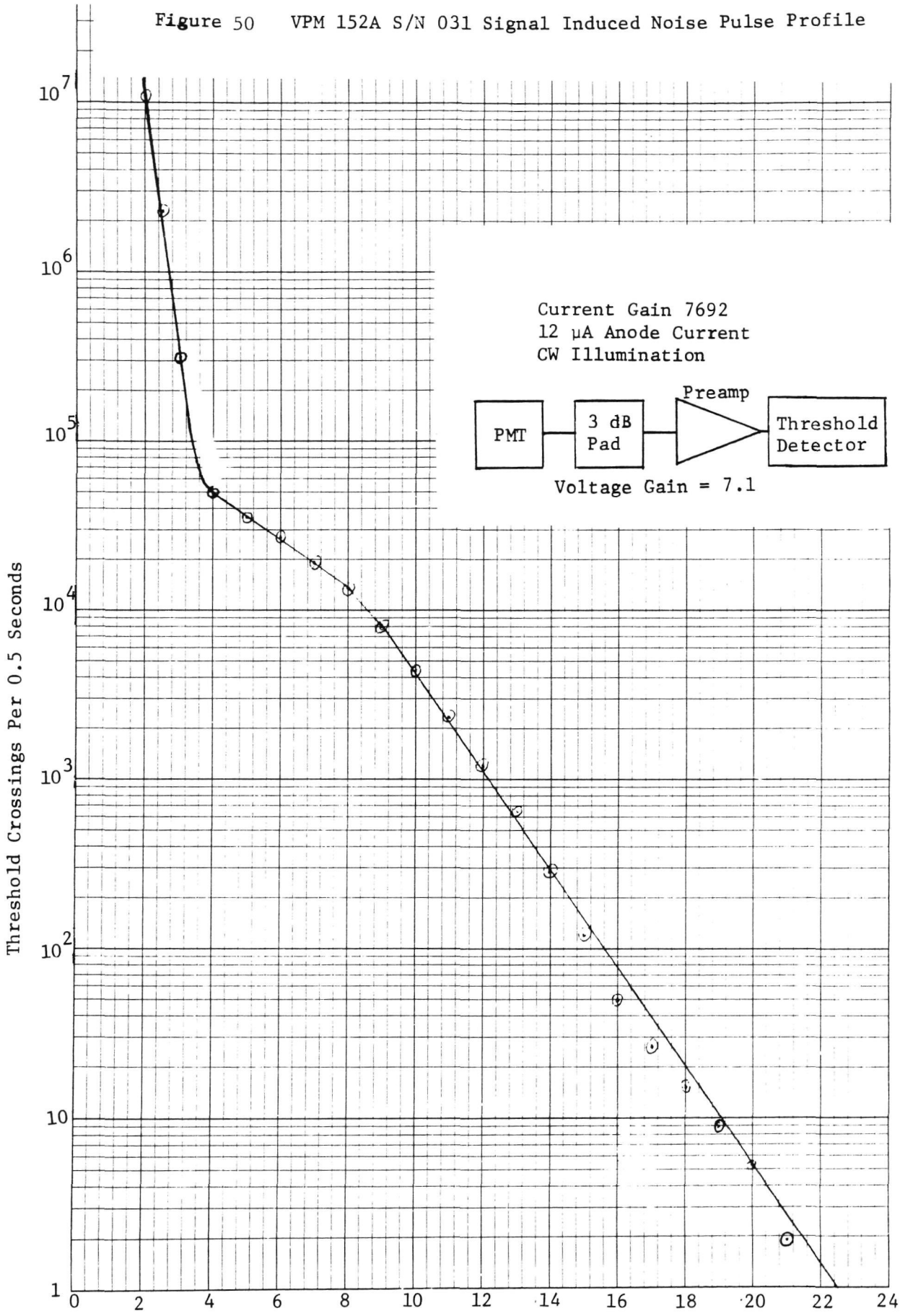

Figure 51 VPM 152A S/N 031 Noise Pulse Delay

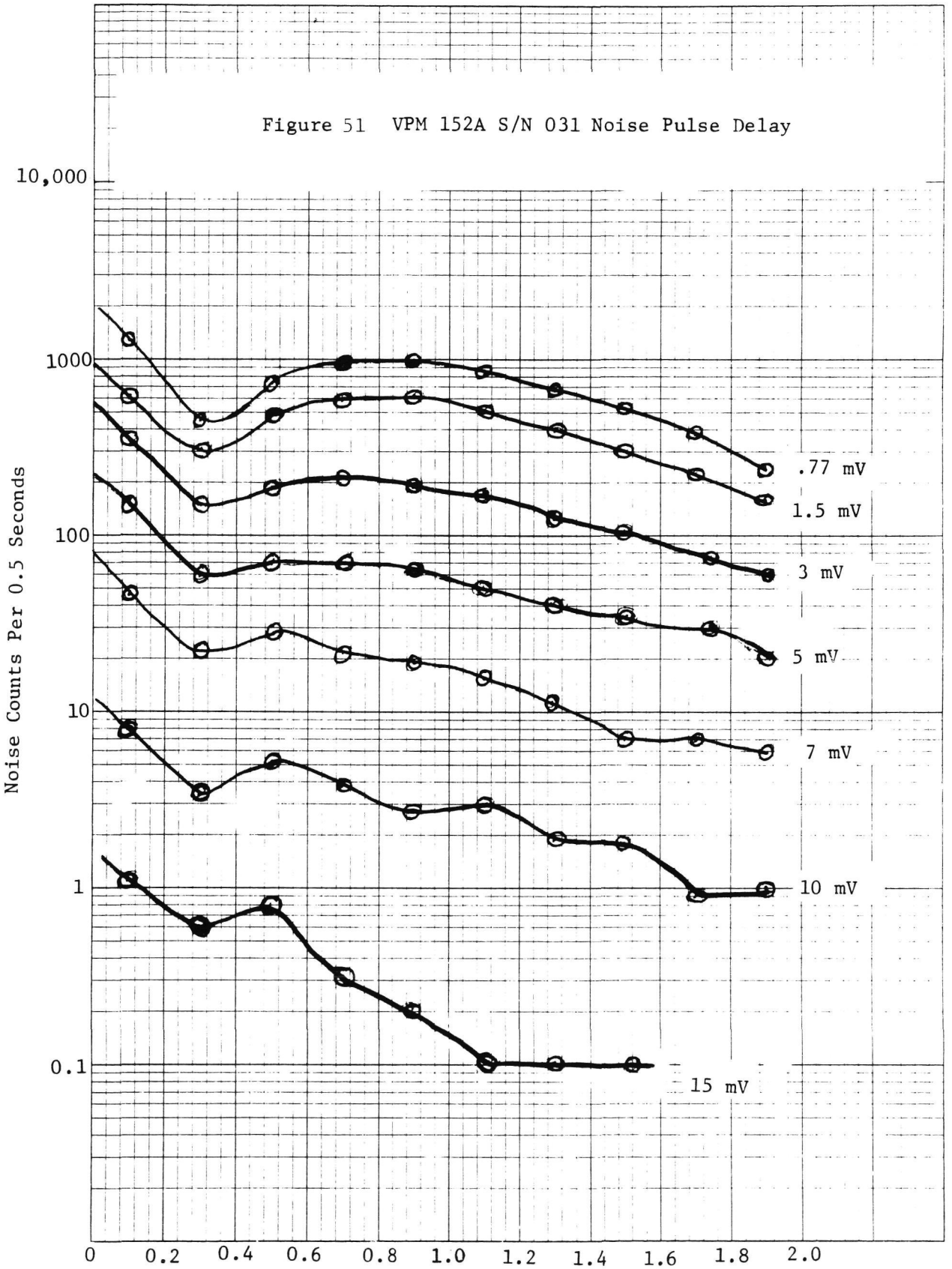

Figure 52 VPM 152A S/N 035 Signal Induced Noise Pulse Profile

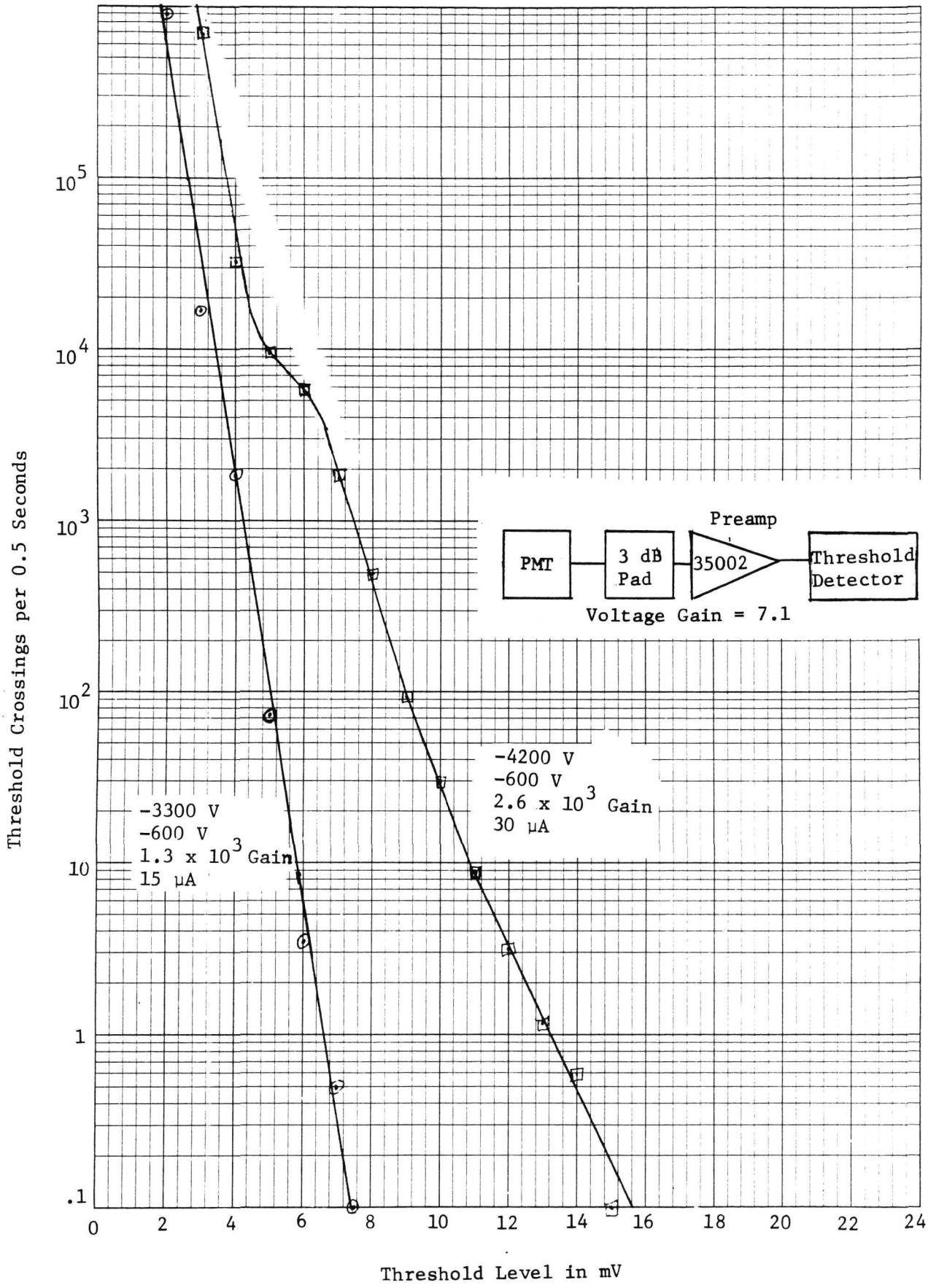

The lower gain curve had a proper linear dependence down to the resolution of the measurement. Yet communication system testing showed severe degradation below 10^{-6} bit error rate. This demonstrated that the bit error rate measurement was a very much more sensitive test for the presence of noise pulses than the pulse profile measurement.

This detector did not have sufficient noise to observe time delay behavior of the signal induced noise pulses.

3.5 DISCUSSION OF PERFORMANCE.

The best of the Varian photomultiplier detectors was S/N 035. Quantum efficiency was high for a 1.064 μm PMT during testing. Performance was good in the unit tests (except for NEIP). The communication system bit error rate measurements showed noise degradation, but S/N 035 was significantly better than all previous tubes of this type. In Figure 39, the best bit error rate curve is plotted along with the performance expected of a very good real photomultiplier tube with the same quantum efficiency. S/N 035 was about 3.9 dB poorer than expected for a real photomultiplier (based on the performance of the best dynamic crossed field photomultiplier utilized in a laboratory model 1 Gbps communication system at 0.53 μm) which was in turn about 1.9 dB poorer than an ideal noiseless detector with a 2.17% quantum efficiency(30 to 1 modulator extinction ratio and zero background).

The excess noise observed with this detector type was certainly due to ions striking the cathode liberated by a mechanism dependent on the presence of output current. This conclusion was supported by the presence of large narrow noise pulses and the long time delay between signal pulses and noise pulses measured on the noisier tubes. (Similar signal induced noise pulses have been observed from noisy static and dynamic crossed field photomultipliers). Much of the problem was due to the relatively open electron multiplier structure. Incorporation of baffles to prevent the input from "seeing" the output should eliminate this problem. Otherwise this detector will not be suitable for the high signal level applications considered. On the other hand, the noise problem would not be severe in a low average signal level situation as encountered in acquisition or ranging applications.

4. ROCKWELL HYBRID DETECTOR

4.1 DESCRIPTION.

The gallium arsenide antimonide avalanche photodiode (GaAsSb APD) fabricated by Rockwell is an inverted mesa structure. Radiation passes through the gallium arsenide substrate which is transparent at 1.064 μm to be detected in a region under the mesa. This APD has a small sensitive area, low capacitance, and very high speed of response. Rise times less than 25 ps have been reported[3]. One such GaAsSb APD detector was evaluated.

The Rockwell hybrid detector consists of a GaAsSb APD combined with a hybrid wideband preamplifier integrated into a detector package. The APD chip is placed at the input of the preamplifier to preclude reflections due to time delay and mismatch. The preamplifier is a baseband transimpedance amplifier fabricated with GaAs microwave MESFET transistor chips. The transimpedance is typically several kΩ which provides significant voltage gain over the same detector operating into a 50Ω preamplifier. This voltage gain is achieved at the expense of speed of response, which is initially much faster than needed in this 400 Mbps application. An output amplifier stage with a voltage gain of 1/3 drives a 50Ω load. Only detector M-7 has an additional voltage gain stage. Considerable care is taken to eliminate reflections at the preamplifier output. Four such detectors were evaluated.

Recent GaAsSb APD detectors have almost unity quantum efficiency at 1.064 μm. The spectral response is a bandpass centered near 1.064 μm. Response falls off on the short wavelength side because the GaAs substrate becomes opaque in the visible. Response falls off on the long wavelength side because the optical absorbtion coefficient of the active layer (depletion region) falls. Below avalanche, detector uniformity is typically very good. With even modest avalanche gains, uniformity becomes extremely poor and only a few hot spot areas exceeded gains of 5 or so. Typical average gain was 2 to 3. Peak gains at hot spots up to 15 have been observed[4]. Selection of a very tiny hot spot for improved performance is not feasible in a real system when the total sensitive diode area is only 0.076 or 0.127 mm in diameter.

---

[3] R. C. Eden, Proc. IEEE, Vol. 63, No. 1, January 1975, pp 32-37.

[4] R. C. Eden, Private Communication

Because of the gain nonuniformity, unity gain bias was selected as normal for these measurements. In practice, operating with optimum avalance gain over the full detector area would result in perhaps a factor of 2 improvement.

Rockwell hybrid detectors M-7 and M-8 were both received with GaAsSb APD's which could not be operated above unity gain due to breakdown or leakage induced noise. After characterization testing at unity gain, these devices were returned to the manufacturer for replacement of the GaAsSb APD. The former versions were designated M7a and M8a, and the latter versions were designated M7b and M8b. Scant data was taken with M-8a, so that it could be quickly returned for replacement of the APD. M8b was not operative as received and no data was taken.

A compilation of data provided by the manufacturer appears in Table VIII. Quantum efficiency measurements were performed with a spatially filtered laser source to remove the effect of scattered radiation which passes through the lens but does not strike the diode. The quantum efficiency of several detectors was verified by such measurements, but in each case the manufacturers figures were taken as accurate for calculations.

4.2 BIT ERROR RATE TESTS.

Communication system bit error rate test data for the Rockwell detectors is summarized in Table IX. The bit error rate curves of the hybrid detectors operated at unity gain bias on the APD's is shown in Figure 53. At unity gain bias potential, typically 80V for most detectors tested, uniformity of photo-response was very good. Nevertheless, some small improvement was realized by focusing to a small spot, and this was done for all cases with a 16 mm or 32 mm lens unless otherwise specified. At modest avalanche gain, the detector uniformity deteriorated drastically. At high reverse bias, only "hot spots" achieved high avalanche gain. Although operation on a selected hot spot may yield impressive data, the measurement is extremely difficult to perform because the target area is far too small to be utilized in any real system situation. The peak gain spots are only a few microns in diameter, and standard precision micrometers are too coarse to readily adjust the position of a focused spot upon them. Figure 54 shows the best bit error rate test data

TABLE VIII

ROCKWELL HYBRID DETECTOR MANUFACTURER DATA

Detector	QE	Diameter	Hybrid Preamplifier			Unity Gain APD Bias			Comments
			Transimpedance OF First Stage	Gain of Later Stages	Bandwidth (3 dB)	Minimum Detectable Signal	Noise Equivalent Power	Estimated Signal For 10^{-6} BER	
	%	Microns	Ohms=Volts/Amp	Volt/Volt	MHz	Pe/Pulse	$W/Hz^{1/2}$	Photons/ Pulse	
M-4	97	127	2525	0.34	303	722	4.0×10^{-12}	7200	
M-5	97	127	2548	0.29	408	593	3.3×10^{-12}	<6000	
M-7a	96	127	3457	4.6 x 0.38	290	492	3.0×10^{-12}	4900	Additional Preamplifier Stage
M-7b	96	127	3457	4.6 x 0.38	290	492	3.0×10^{-12}	4900	
M-8a	54	127	4750	0.35	538	418.5		8000	Poor Diode
M-8b	96	76.2	4750	0.35	620	360	2.4×10^{-12}	3600	

TABLE IX

ROCKWELL DETECTOR 400 Mbps PGBM COMMUNICATION SYSTEM TEST RESULTS

DETECTOR	QUANTUM EFFICIENCY	FOR 10^{-6} BIT ERROR RATE			COMMENTS
		1.064 μm POWER	PHOTONS/PULSE	PHOTOELECTRONS/PULSE	
M15-7 APD	55.2%	3800 nW	1.02×10^5	5.6×10^4	4 μA
Hybrid M-4	*97%	501 nW	13417	13015	Unity gain 80V
		186	4981	4832	Best focused spot 114V
Hybrid M-5	*97%	234 nW	6267	6079	Unity gain 80V
		57 nW	1537	1491	Best focused spot 115.1V
Hybrid M-7A	*96%	199 nW	5324	5111	Unity gain 80V
Hybrid M-7B	*96%	206 nW	5520	5299	Focused unity gain 80V
		78 nW	2092	2008	Best focused spot 125.0V
Hybrid M-8A	67.8%	373 nW	9989	6773	Unity gain 115V
Hybrid M-8B	--	--	--	--	Defective

* Manufacturer Estimated Quantum Efficiency

Figure 53 Rockwell Hybrid Detector Unity Gain Bit Error Rate Data

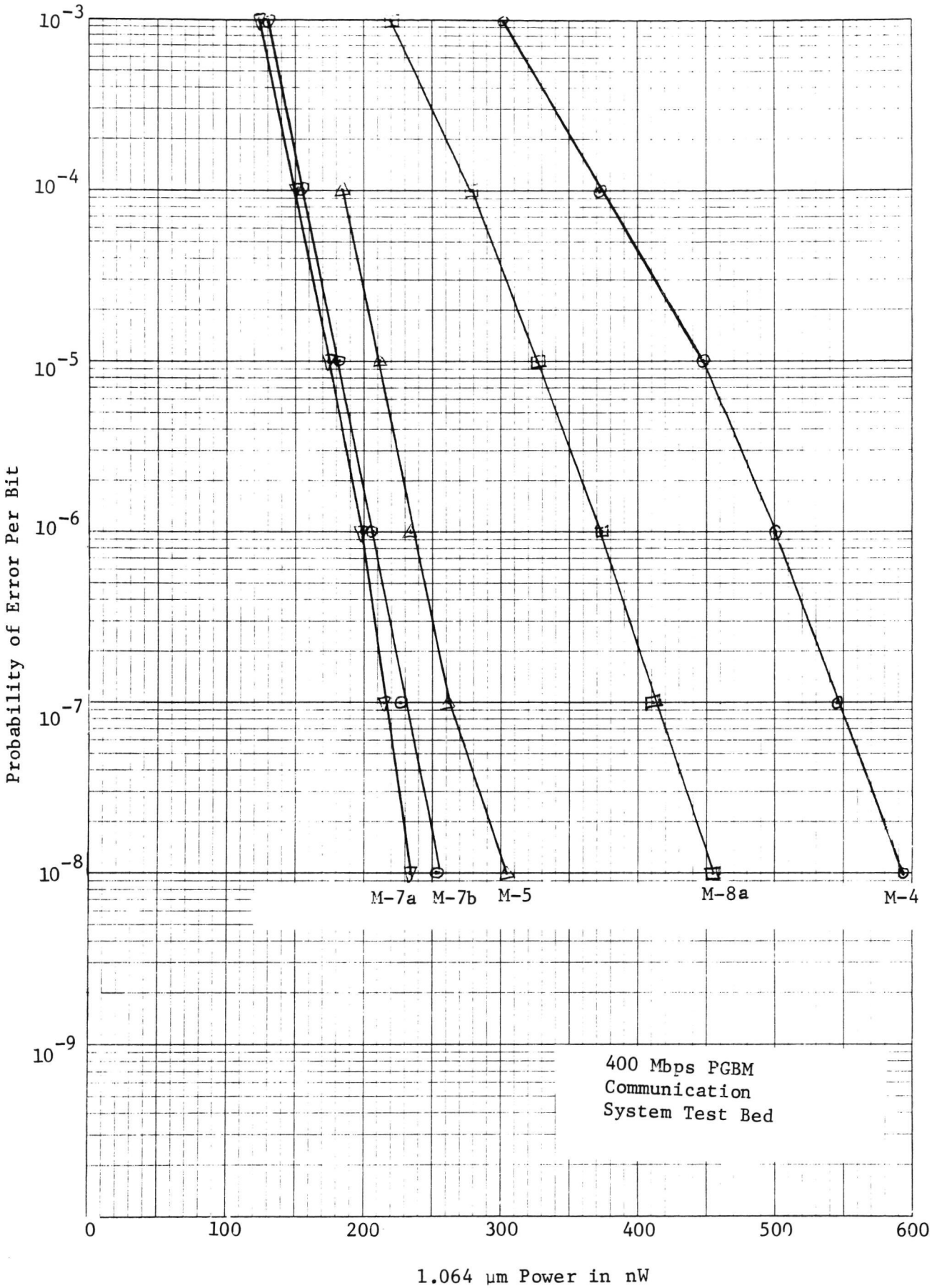

FIGURE 54 ROCKWELL HYBRID DETECTOR OPTIMUM GAIN BIT ERROR RATE DATA

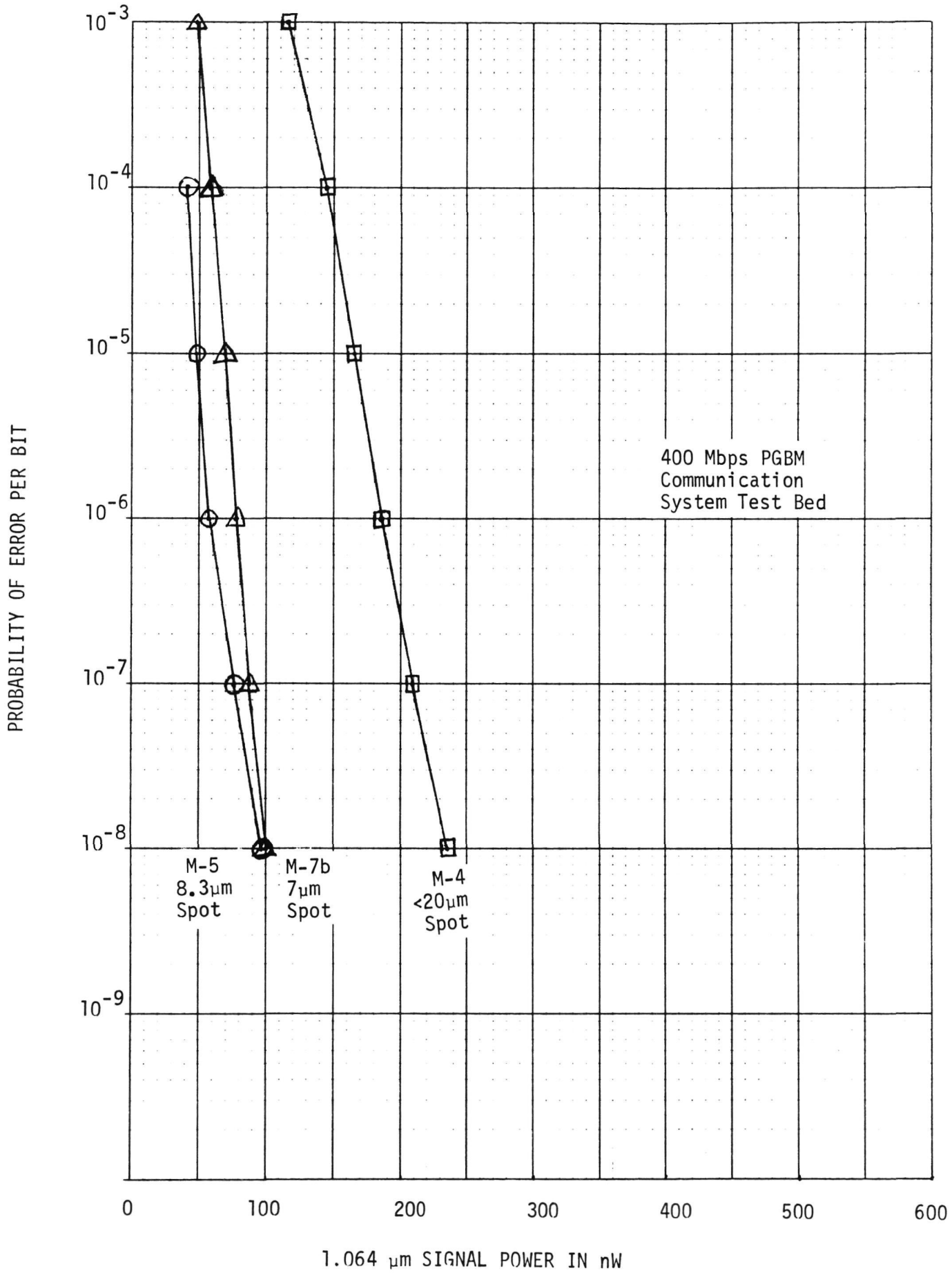

achieved with optimal bias and fine focusing upon the best high gain spots. Figure 55 shows 0.32 dB improvement in communication system performance at unity gain due to focusing the signal spot on the detector, and an additional 4.2 dB improvement when operated at optimum bias on a hot spot.

4.3 UNIT TESTS

4.3.1 GaAsSb APD M15-7

Detector M15-7 was an early heterojunction GaAsSb diode in a 50 ohm mount grown several years ago utilizing a different type of structure from the present homo-heterojunction devices in the hybrid detectors and is not representative of current device technology.

The dark current-voltage characteristic of APD M15-7 is shown in Figure 56. The quantum efficiency at 35V bias ($\sim$ unity gain) was measured at 55.2%.

Figure 57 shows the scanned photoresponse of APD M15-7. Scans of the photocurrent and of the 200 MHz components of the photocurrent are shown. A severe microplasma was observed at the upper right hand edge which had high dc gain at only 35.2V bias but did not contribute to the high frequency output at all. With increasing bias, two similar microplasmas appeared. With increasing gain, the high frequency response became wavy and nonuniform. At high gain the response was dominated by an array of hot spots and was extremely noisy.

Figure 58 shows the impulse response of APD M15-7. Figure 59 shows the detected waveforms in communication system tests in normal operation and focused on the low frequency microplasma. A large slow response signal was superimposed on the normal high frequency response. Post pulse ringing was due to the wideband preamplifiers used in this test.

Recent GaAsSb APD detectors have displayed improved quantum efficiency and uniformity. The impulse response waveform in Figure 84 was obtained with a newer device.

Figure 55 Rockwell Hybrid Detector M-7b Bit Error Rate Data

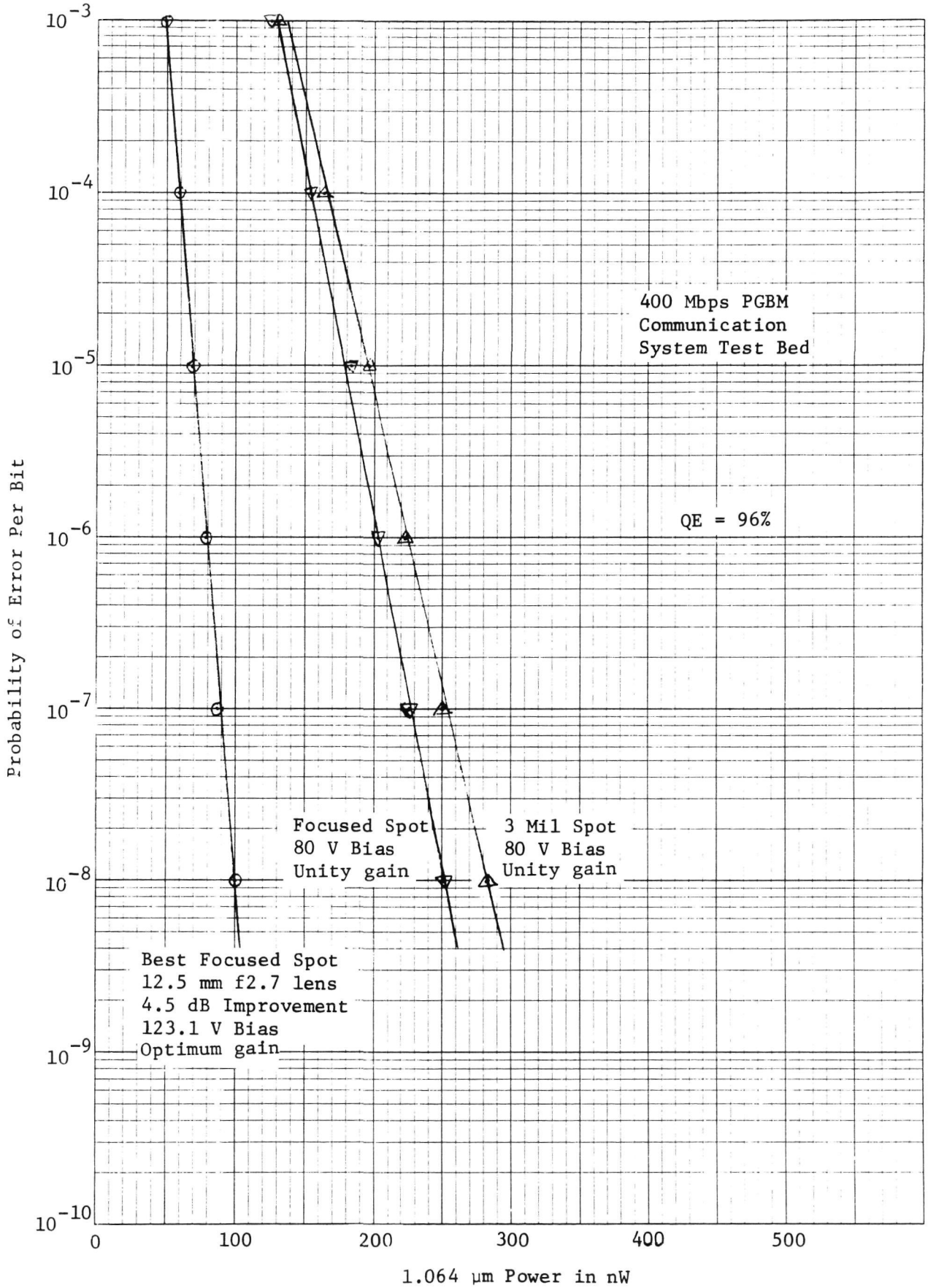

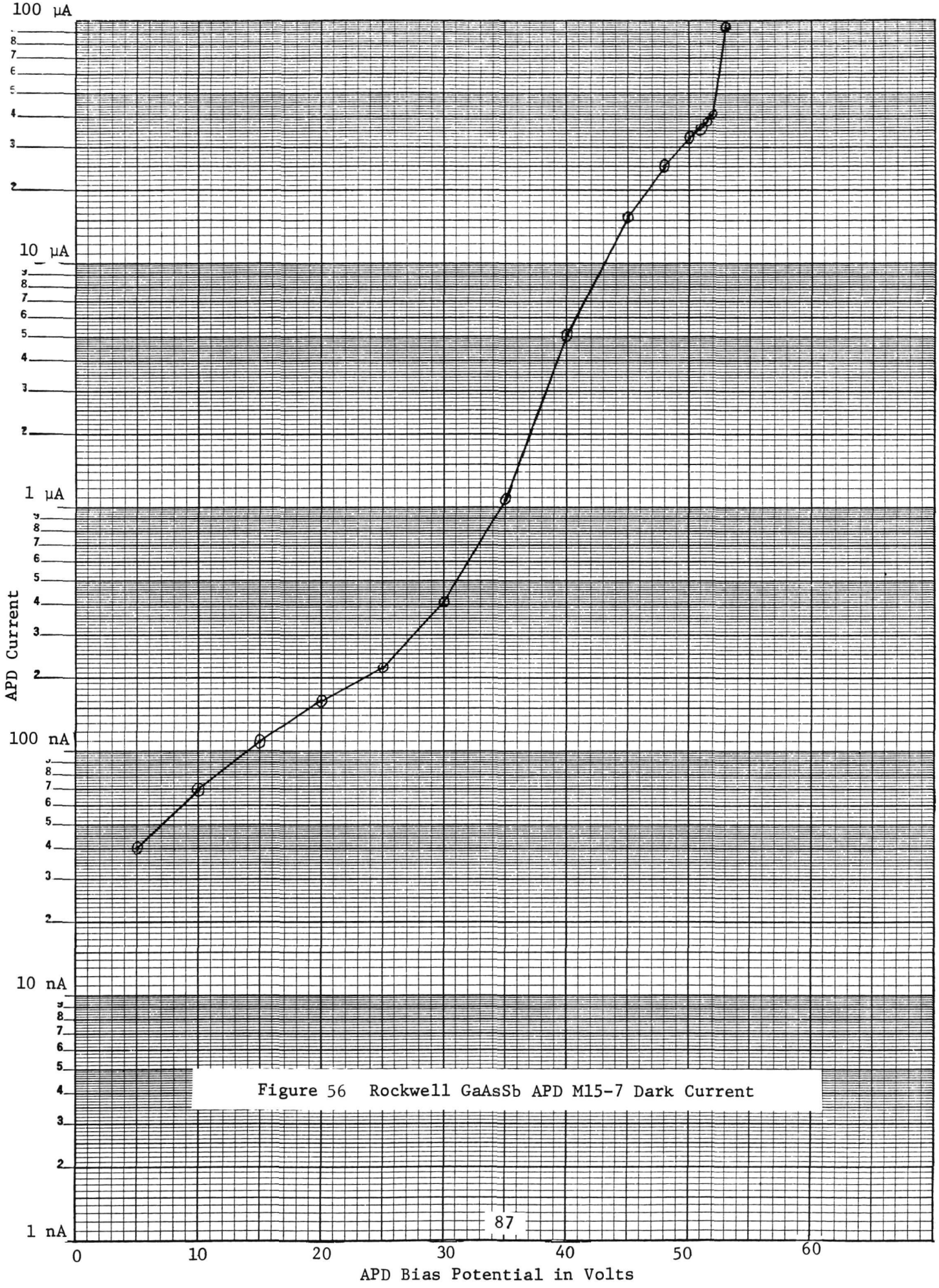

Figure 56 Rockwell GaAsSb APD M15-7 Dark Current

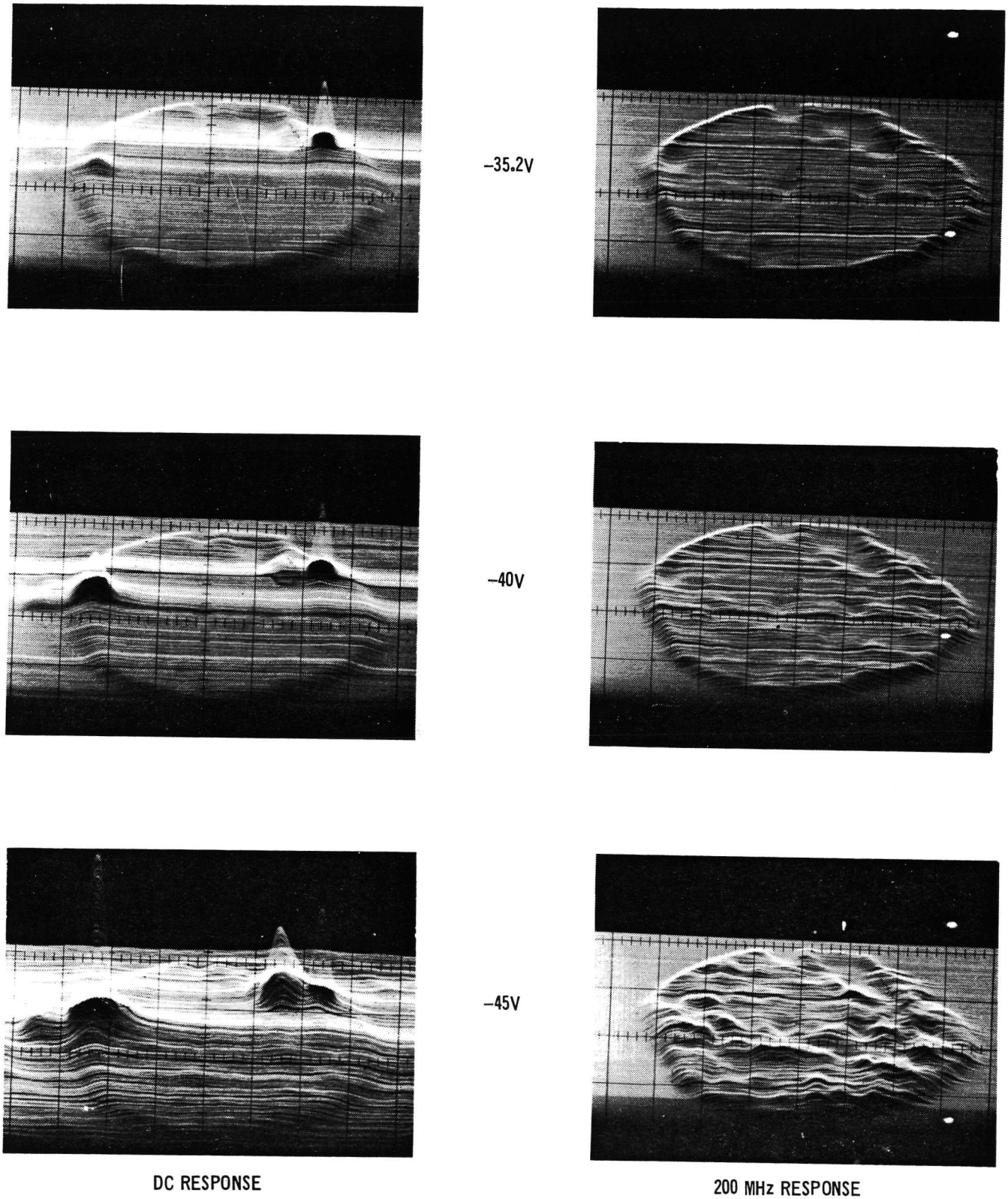

FIGURE 57A Rockwell GaAsSb APD M15-7 Photoresponse Scans

REPRODUCIBILITY OF THE
ORIGINAL PAGE IS POOR

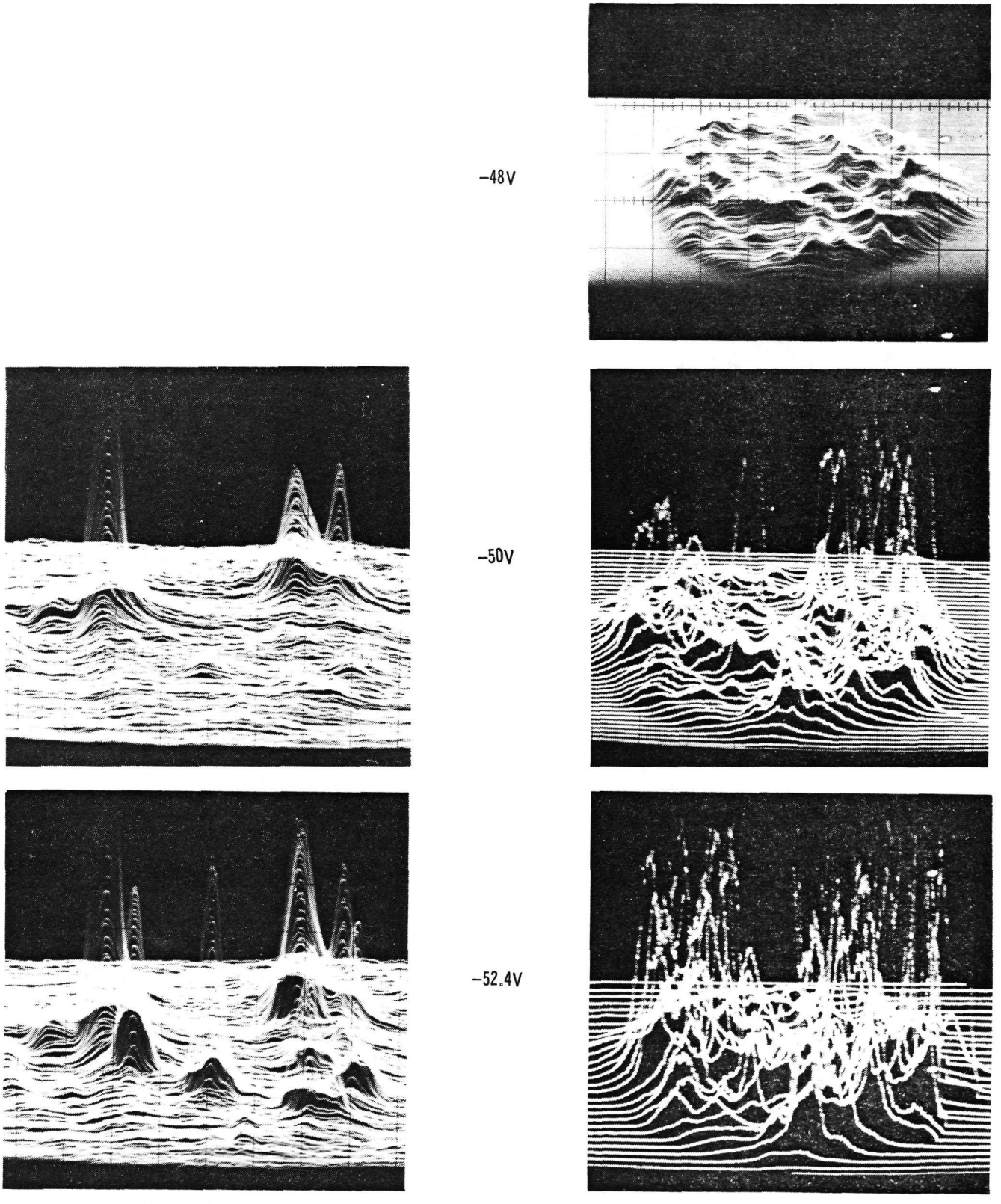

Figure 57B Rockwell GaAsSb APD M15-7 Photoresponse Scans

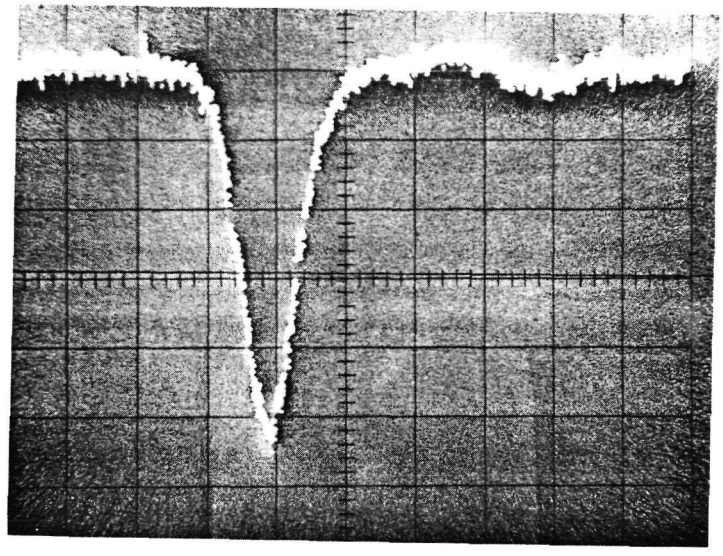

5 mV/div

200 ps/div

Figure 58 Rockwell GaAsSb M15-7 Impulse Response

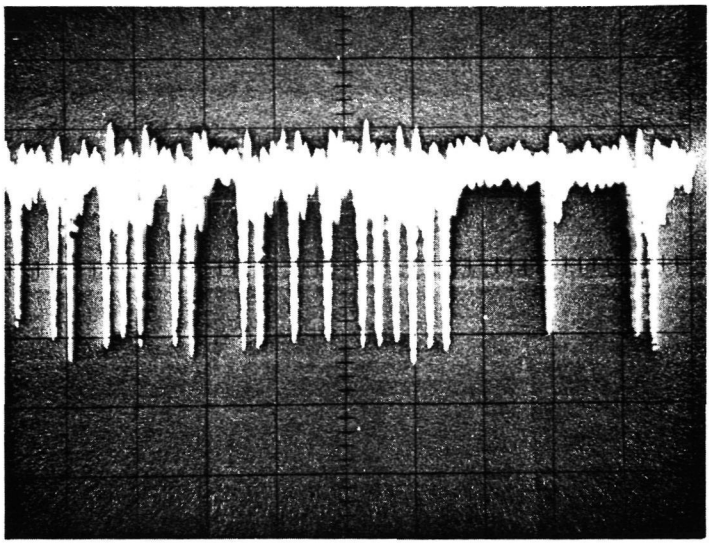

Normal
Operation

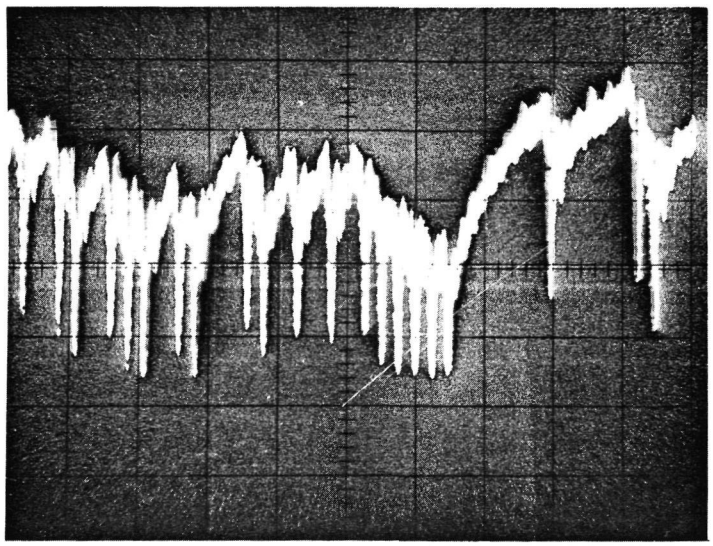

Hot Spot

Vertical 500mV/div

Horizontal 10nsec/div

FIGURE 59 ROCKWELL GaAsSb APD M15-7 WAVEFORMS

Figure 60 shows a plot of noise equivalent input power versus applied bias for APD M15-7. Optimum bias was -52.2V.

4.3.2 Hybrid Detector M-4

The dark current-voltage characteristic of the GaAsSb APD in hybrid detector M-4 is shown in Figure 61. The quantum efficiency at unity gain bias was 97% as measured by the manufacturer.

Figure 62 shows the scanned photoresponse of detector M-4. Scans of the photocurrent and of the 200 MHz component of the photocurrent are shown. The photoresponse at unity gain (80V) was very uniform. At an avalanche gain of only 2 to 3, the response became very wavy and nonuniform. High gain was only experienced by two hot spots.

Figure 63 shows the output waveform of detector M-4 in response to the 400 Mbps communication system signal. The response was sufficiently fast to return to the baseline between adjacent transmitted "1" pulses spaced 2.5 ns apart. Figure 64 shows the impulse response of detector M-4. A rise to 60% of maximum in 100 psec was preceeded by an unusual glitch of opposite polarity. Risetime was 300 ps (10% to 90%) and fall time was 1.2 ns (90% to 10%). A slower preamp than the B & H DC-3002 unit (DC - 3 GHz bandwidth) smoothed the response in system measurements.

Figure 65 shows a plot of noise equivalent input power versus applied APD bias potential. At optimal bias of -115V, the NEIP decreased 6 dB with the size of the focused signal spot when operating on the best hot spot.

4.3.3 Hybrid Detector M-5

The dark current-voltage characteristics of the GaAsSb APD in hybrid detector M-5 is shown in Figure 66. The quantum efficiency at unity gain bias was 97% as measured by the manufacturer.

Figure 67 shows the scanned photoresponse of detector M-5. Scans of the photocurrent and of the 200 MHz component of the photocurrent are shown. The

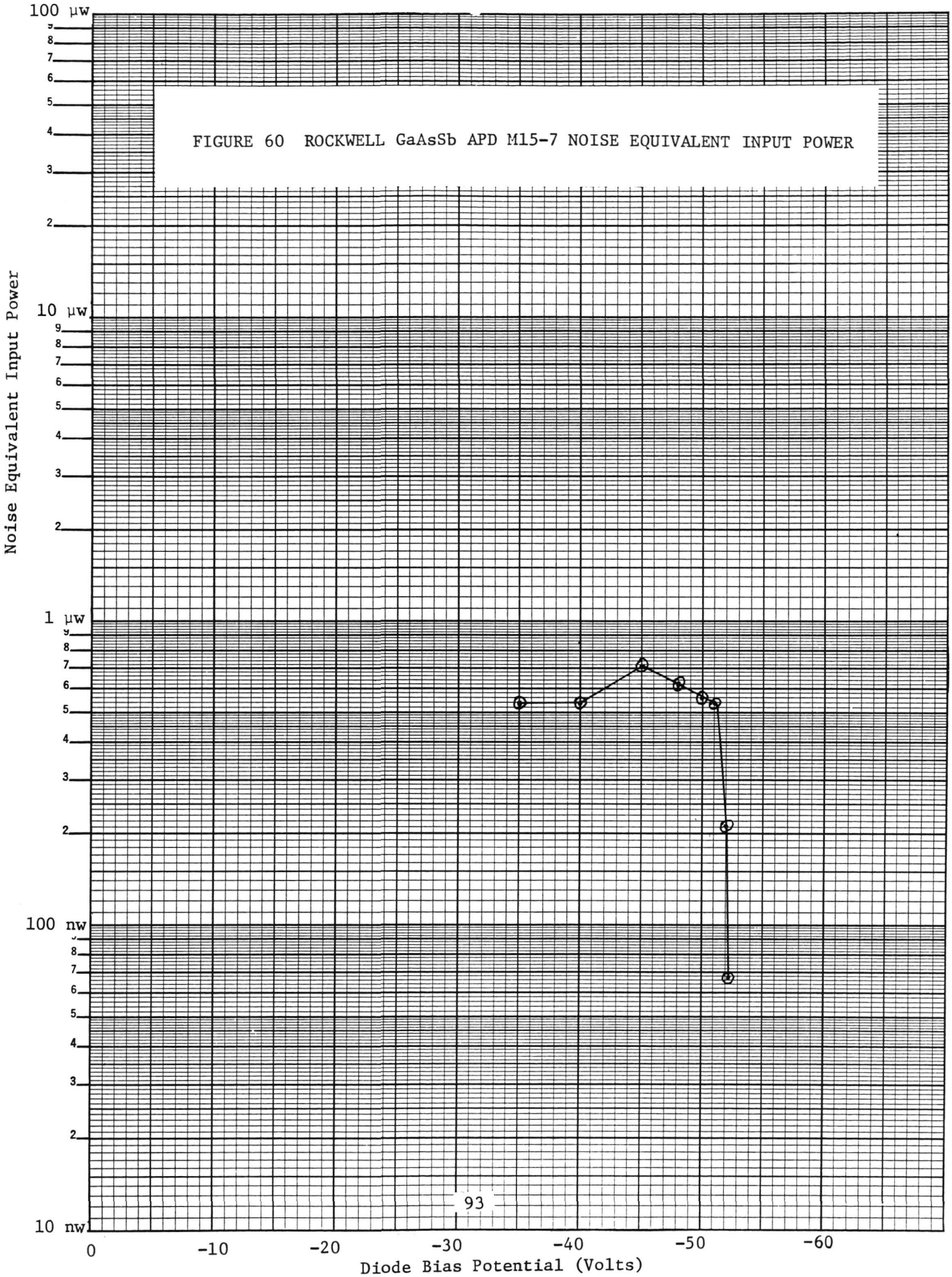

FIGURE 60 ROCKWELL GaAsSb APD M15-7 NOISE EQUIVALENT INPUT POWER

Figure 61 Rockwell Hybrid Detector M-4 APD Dark Current

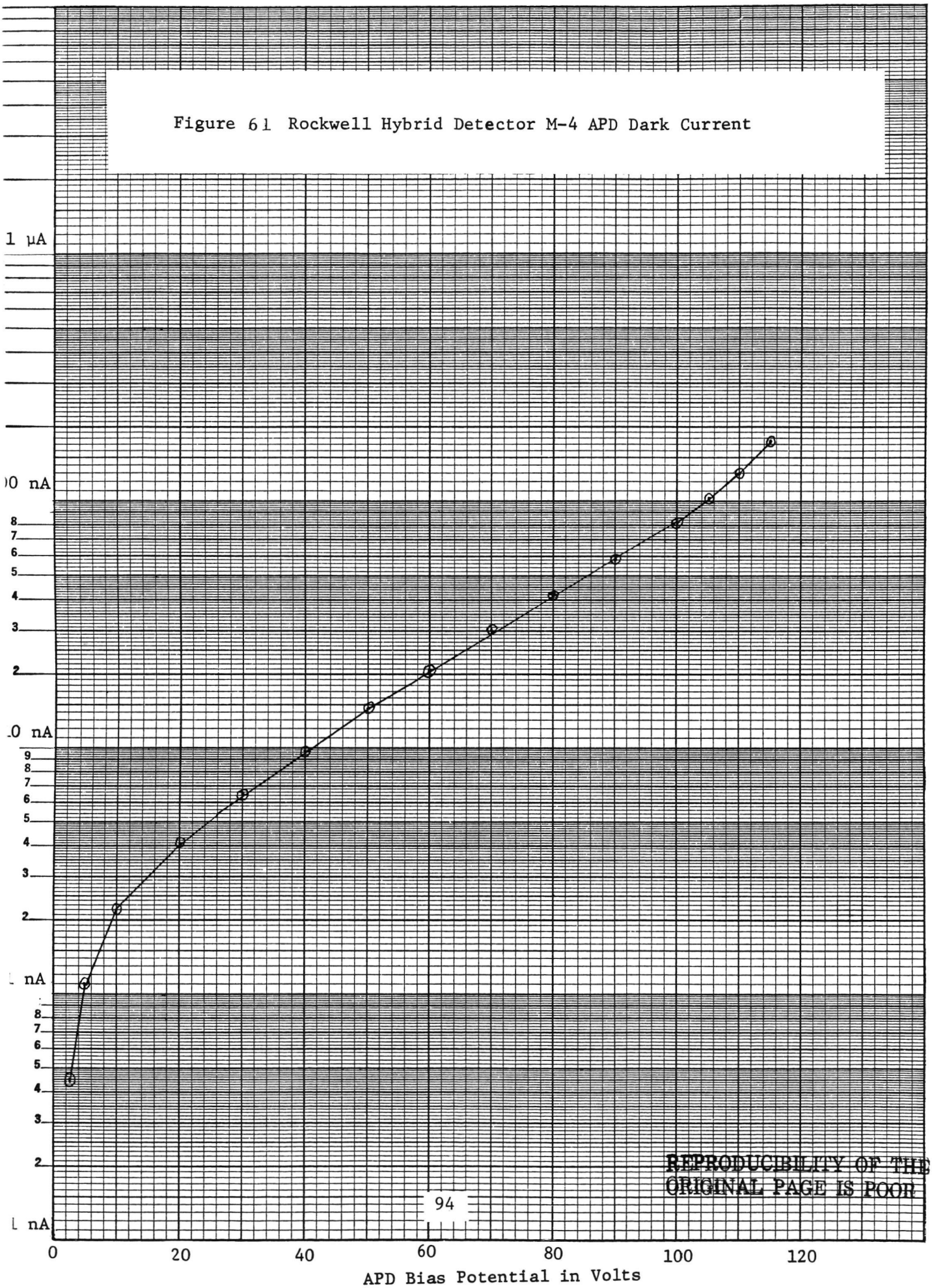

REPRODUCIBILITY OF THE
ORIGINAL PAGE IS POOR

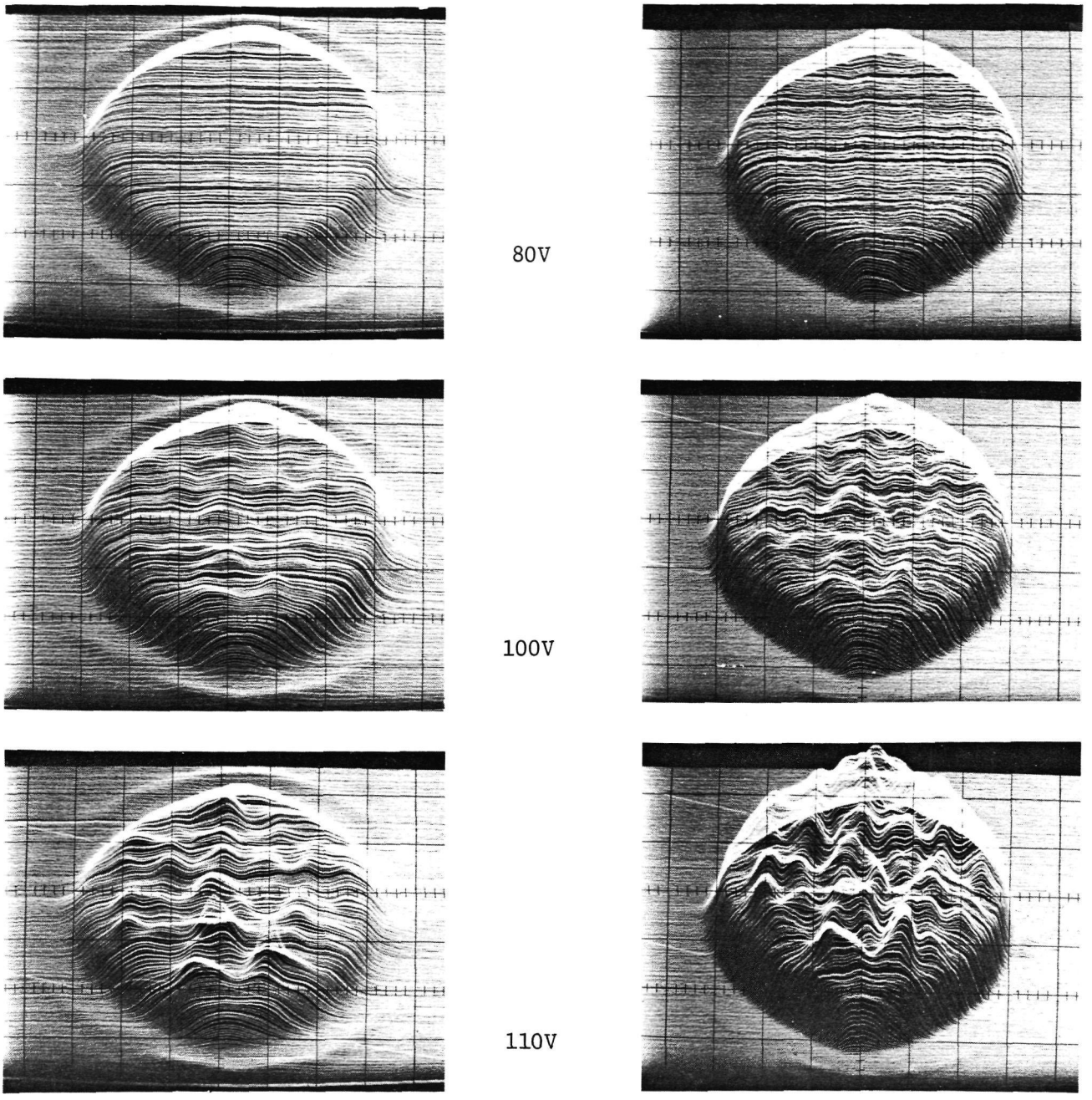

Figure 62A ROCKWELL HYBRID DETECTOR M-4 PHOTORESPONSE SCANS

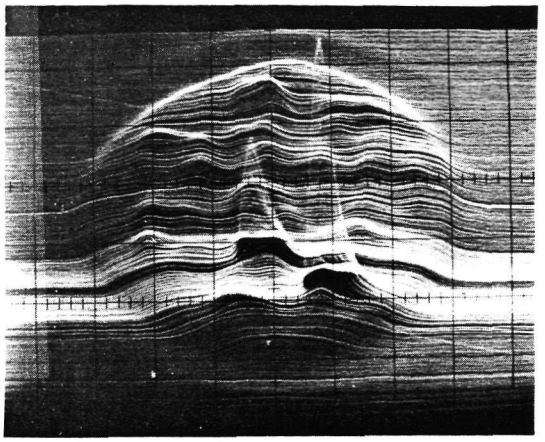

1X Power

113V

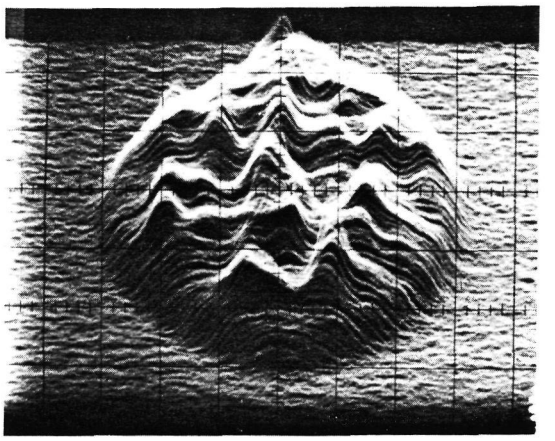

1/30X Power

115V

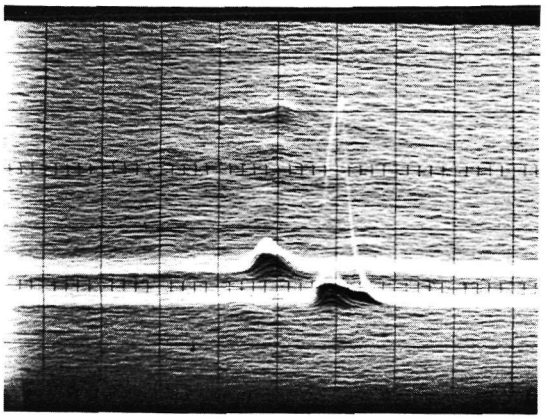

1/100X Power

DC

200 MHz

Figure 62B ROCKWELL HYBRID PREAMP M-4 PHOTORESPONSE SCANS

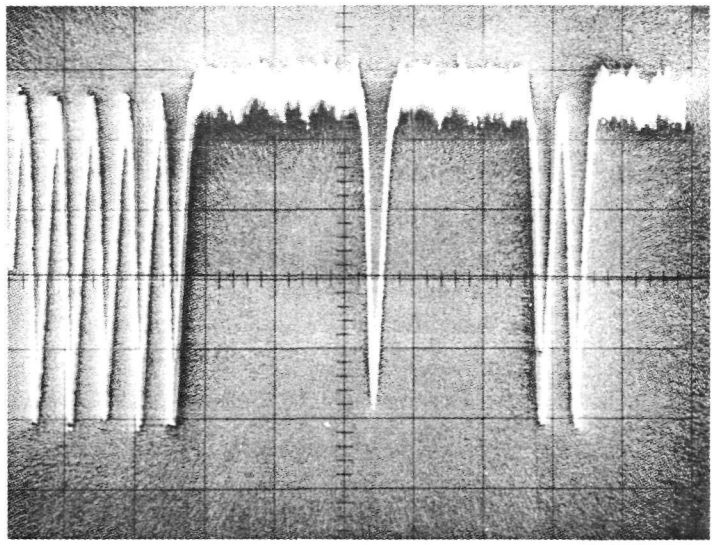

80V bias
0.5 μA diode current
5 ns/div

FIGURE 63 ROCKWELL HYBRID DETECTOR M-4 OUTPUT WAVEFORM

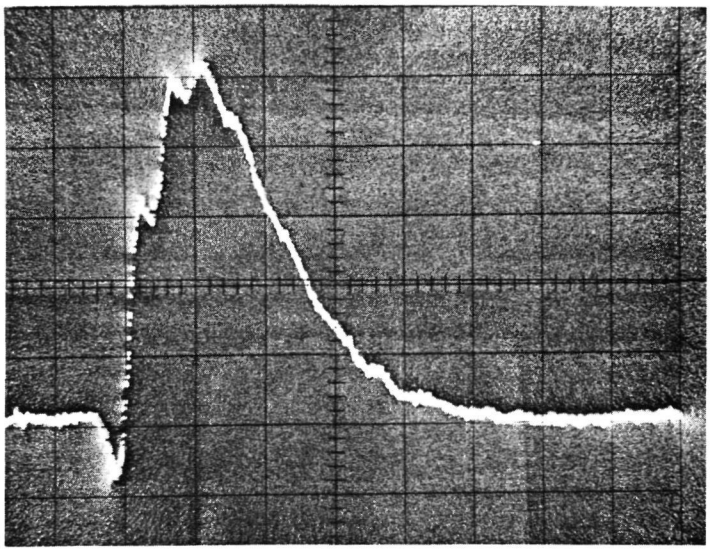

Without Preamp
14 mV/div

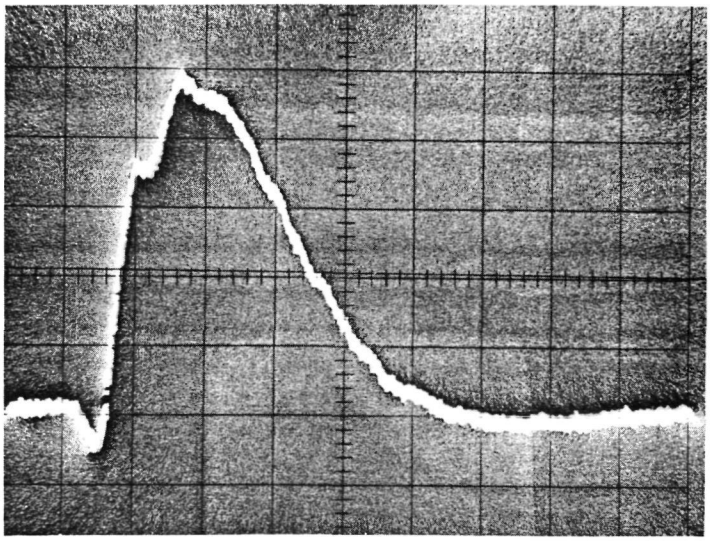

With B&H DC3002
Preamp and 3 dB Pad

1.4 mV/div

Horizontal 500 ps/div

Figure 64 Rockwell Hybrid Detector M-4 Impulse Response

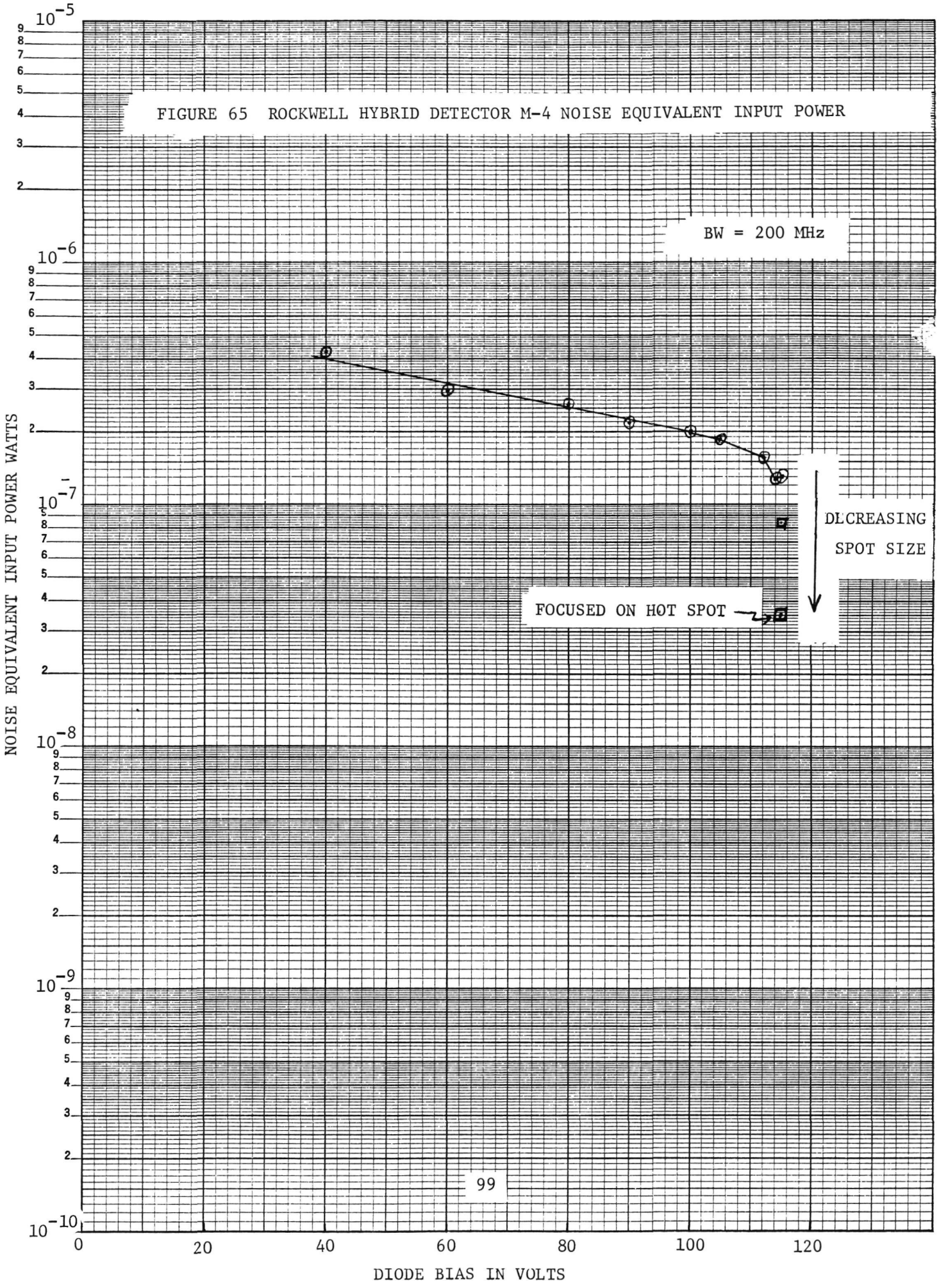
FIGURE 65 ROCKWELL HYBRID DETECTOR M-4 NOISE EQUIVALENT INPUT POWER
BW = 200 MHz
DECREASING SPOT SIZE
FOCUSED ON HOT SPOT
NOISE EQUIVALENT INPUT POWER WATTS
10^{-5}
10^{-6}
10^{-7}
10^{-8}
10^{-9}
10^{-10}
0
20
40
60
80
100
120
DIODE BIAS IN VOLTS

Figure 66 Rockwell Hybrid Detector M-5 APD Dark Current

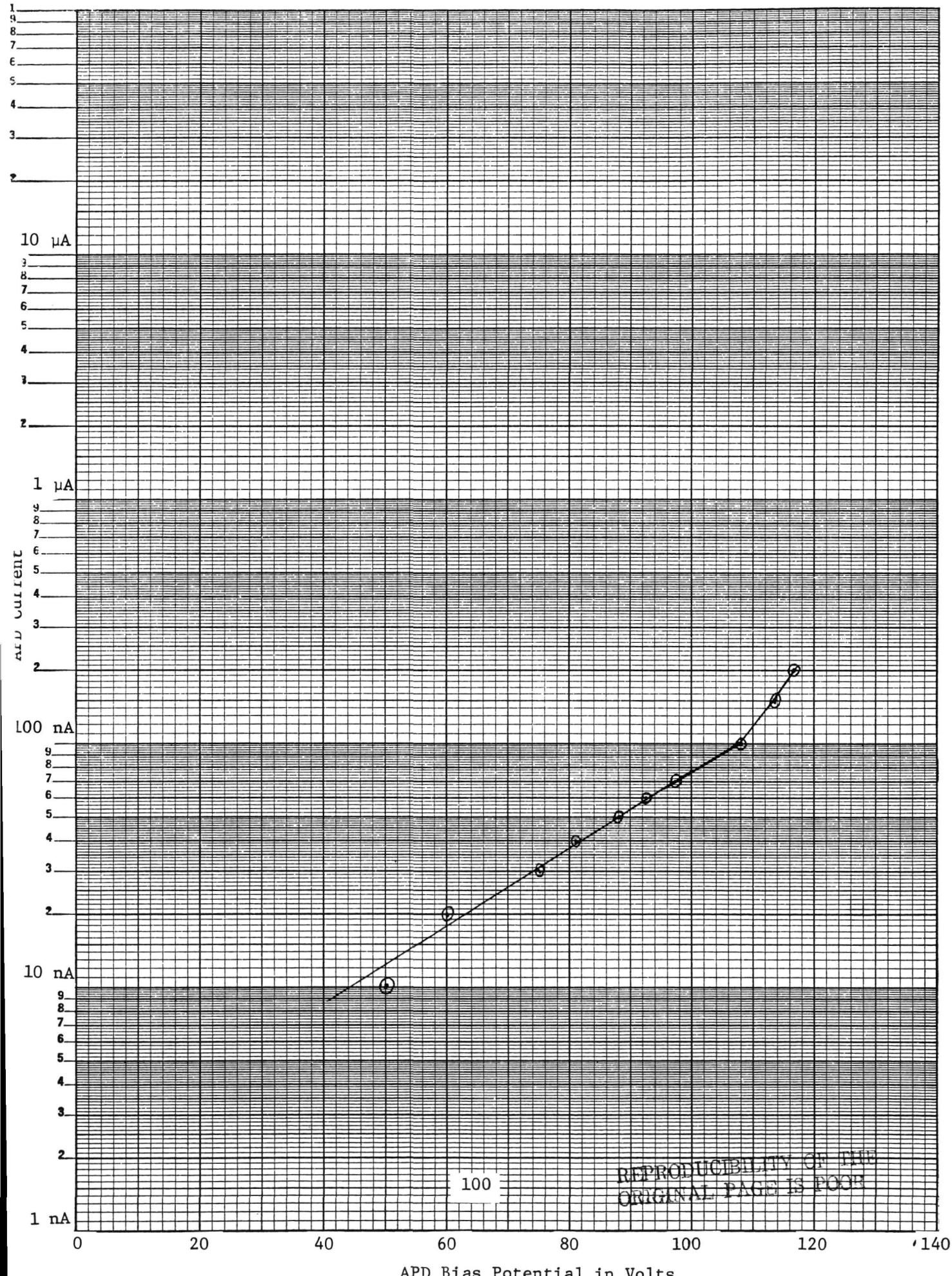

REPRODUCIBILITY OF THE
ORIGINAL PAGE IS POOR

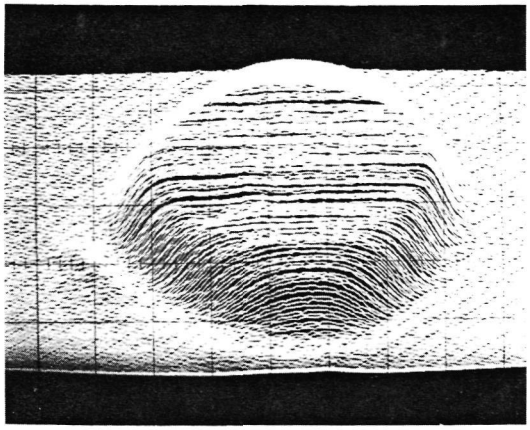

80V

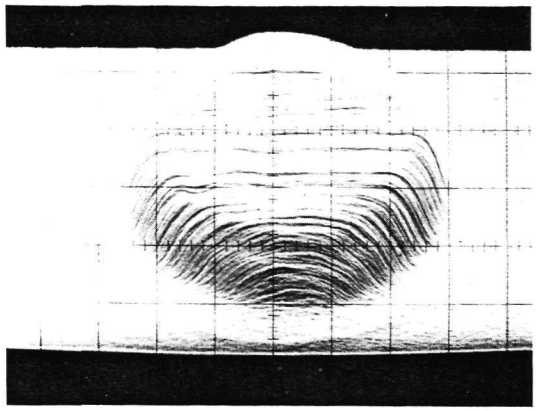

3 μA

0.3 μA

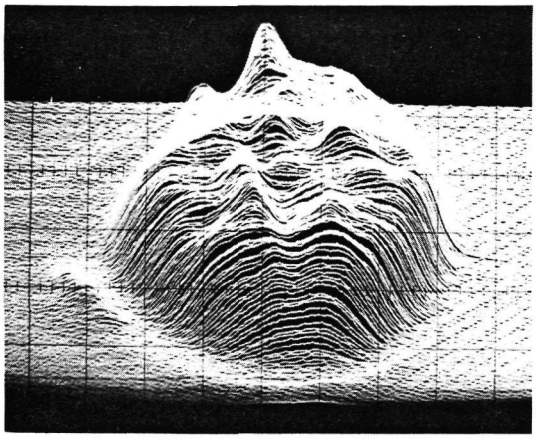

110V

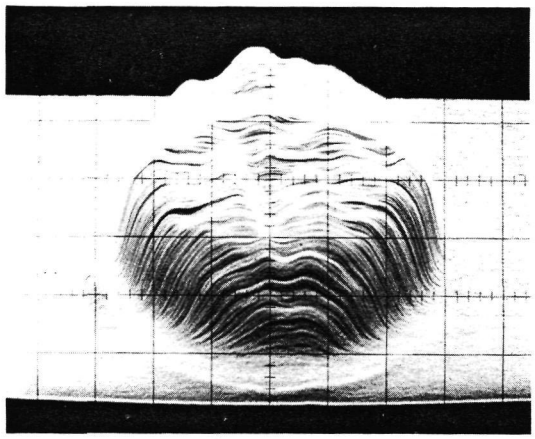

3 μA

0.3 μA

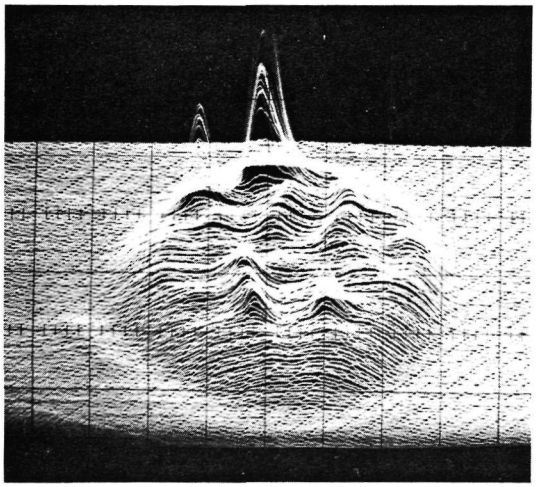

115.1V

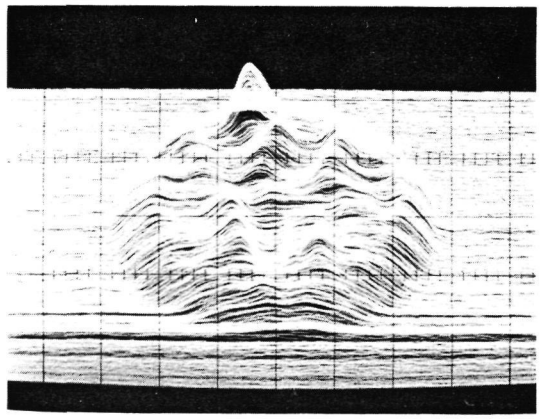

1 μA
dc

0.1 μA
200 MHz

FIGURE 67 ROCKWELL HYBRID DETECTOR M-5 PHOTORESPONSE SCANS

photoresponse at unity gain (80V) was very uniform. At an avalanche gain of 2 to 3 the response became wavy and nonuniform. High gain was experienced by one major hot spot and several minor ones.

Figure 68 shows the output waveform of detector M-5 in response to the 400 Mbps communication system signal. Figure 69 shows the impulse response. Speed of response was somewhat faster than needed to return to the baseline between adjacent transmitted "1" pulses spaced 2.5 ns apart. Overshoot and ringing were observed and yielded a 10% interfering signal at the center of the following bit period. Pulse width at 10% of maximum was 1.8 ns.

Figure 70 shows a plot of noise equivalent input power versus applied APD bias potential. Average performance measured with a blurred spot degraded as noise increased with gain above 115V bias. On a high gain hot spot, however, signal increased faster than noise to yield continued improvement up to 115.9V bias.

4.3.4 Hybrid Detector M-7a.

The quantum efficiency of the GaAsSb APD in hybrid detector M-7a was 96% as measured by the manufacturer.

Figure 71 shows the scanned photoresponse of detector M-7a at unity gain (80V). Scans of the photocurrent and of the 200 MHz component of the photocurrent are shown. Response is uniform.

Figure 72 shows the output waveform of detector M-7a at 200 nA and at 3.3 μA photocurrent. The response was nearly fast enough to return to the baseline between adjacent transmitted "1" pulses spaced 2.5 ns apart. Response was very smooth. A very slight overshoot and ring at 200 nA became a slight undershoot at 3.3 μA. The large signal waveform shows a 30 to 1 modulator extinction ratio at the transmitter.

The noise equivalent input power of detector M-7a at unity gain (80V) was 114.7 nW.

REPRODUCIBILITY OF THE
ORIGINAL PAGE IS POOR

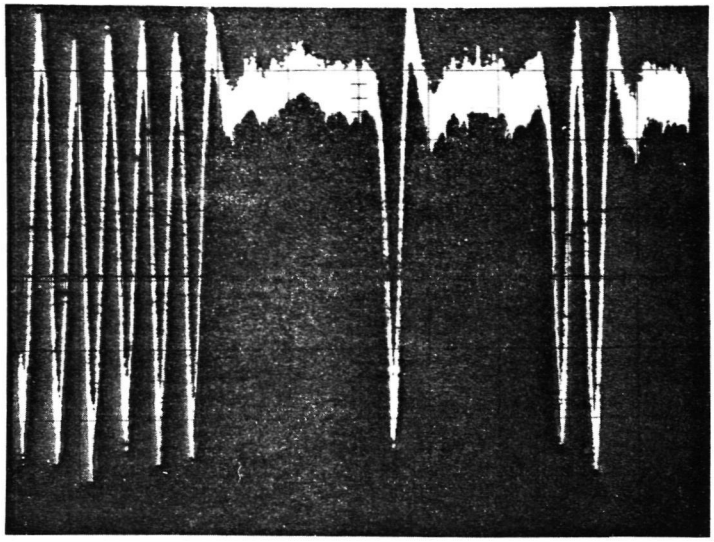

5 nsec/div
i = 0.2 μA

FIGURE 68 ROCKWELL HYBRID DETECTOR M-5 OUTPUT WAVEFORM

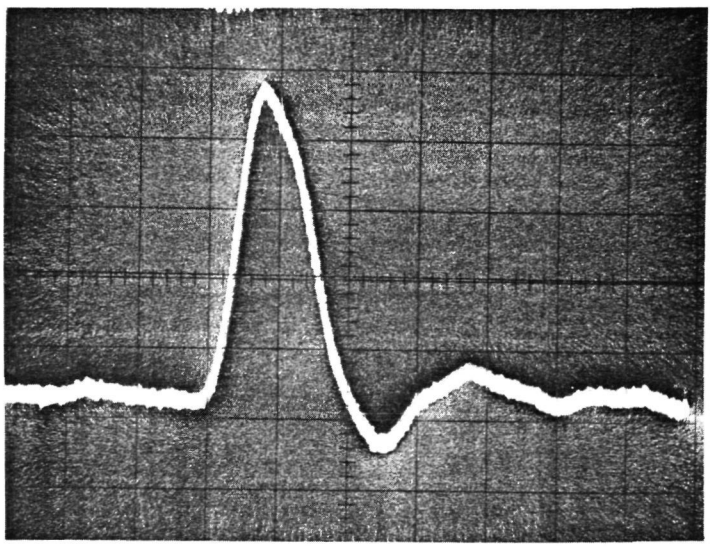

1mV/div
1 nsec/div
i = 2 μA

FIGURE 69 ROCKWELL HYBRID DETECTOR M-5 IMPULSE RESPONSE

FIGURE 70 ROCKWELL HYBRID DETECTOR M-5 NOISE EQUIVALENT INPUT POWER

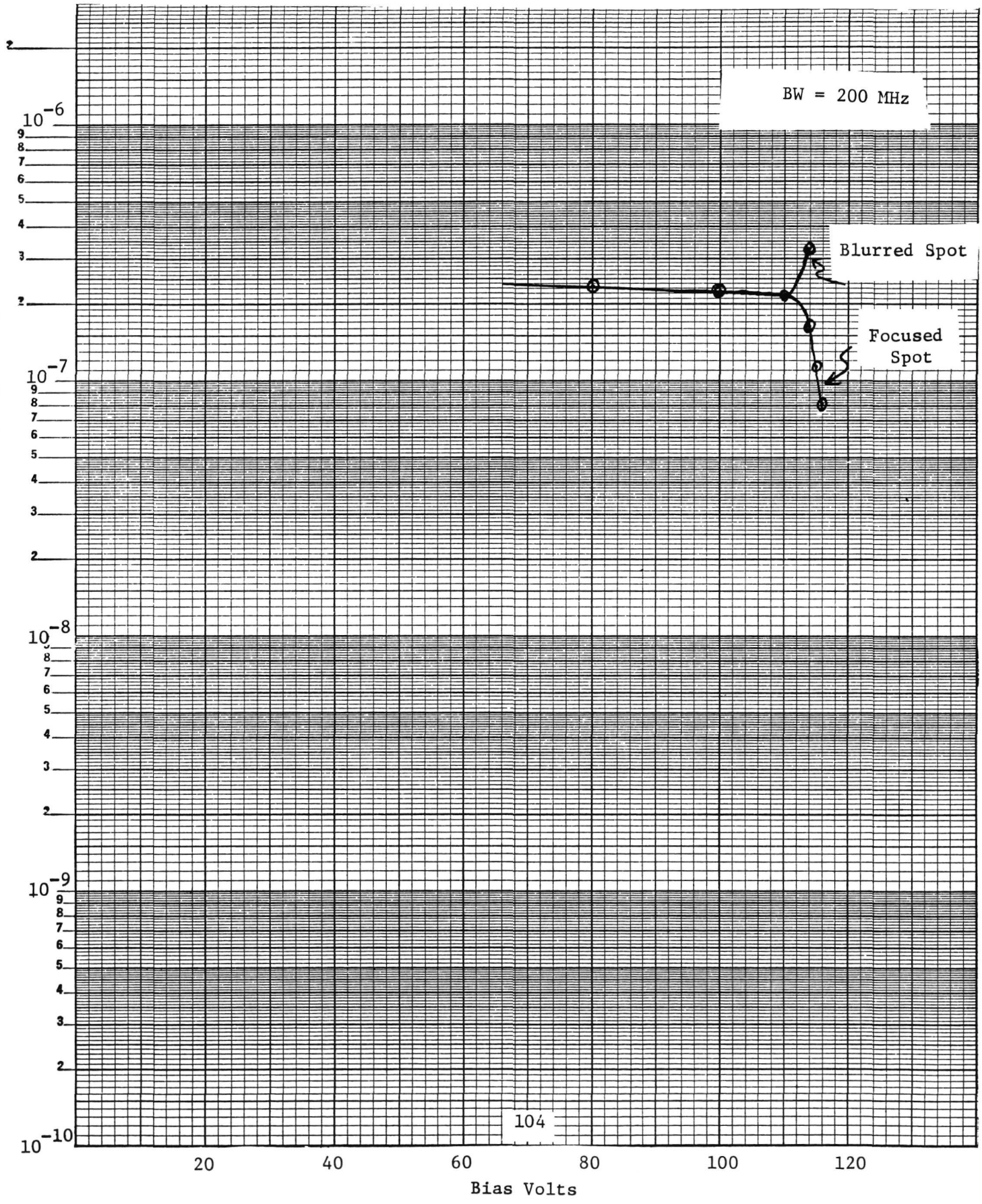

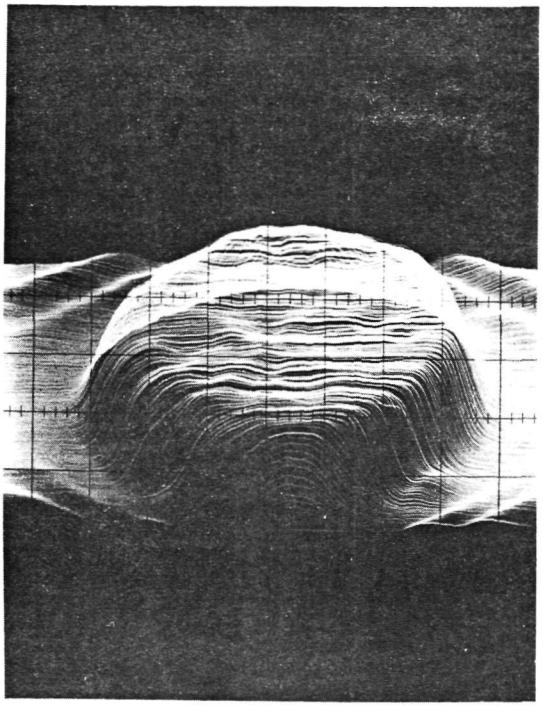

80V
Bias

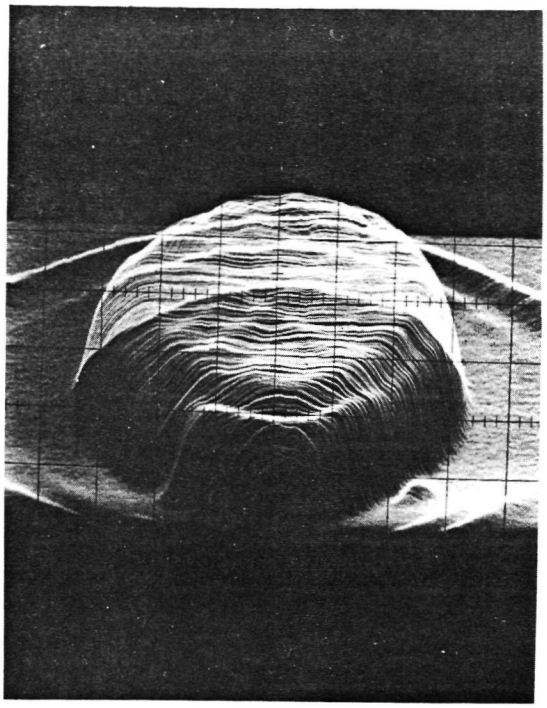

dc (i=2.5 μA)

200 MHz (i=.25 μA)

FIGURE 71 ROCKWELL HYBRID DETECTOR M-7a PHOTORESPONSE SCANS

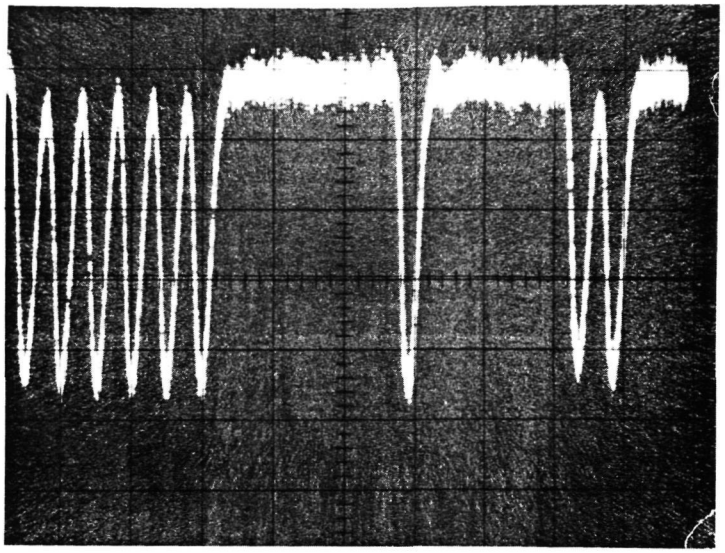

200 nA diode current
5 nsec/div

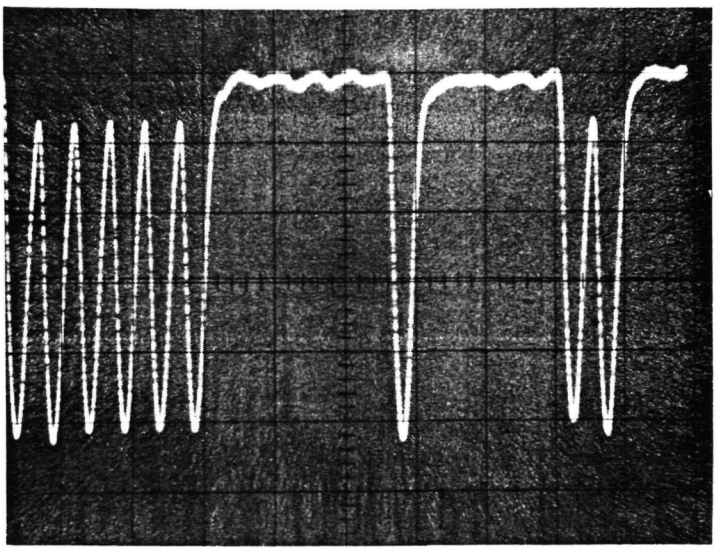

3.3 μA diode current
100 mV/div
5 nsec/div
M-7 into B&H 3002 preamp

FIGURE 72 ROCKWELL HYBRID DETECTOR M-7a OUTPUT WAVEFORM

4.3.5 Hybrid Detector M-7b

The dark current-voltage characteristic of the GaAsSb APD in hybrid detector M-7b is shown in Figure 73. The quantum efficiency was 96% as measured by the manufacturer.

Figure 74 shows the scanned photoresponse of detector M-7b. Scans of the photocurrent and of the 200 MHz component of the photocurrent are shown. Response was uniform at unity gain (80V). At an avalanche gain of 2 to 3 the response was wavy and nonuniform. At high gain, two major hot spots and one lesser hot spot dominated near an edge.

The output waveform is limited by the hybrid preamplifier and is identical to that of M-7a presented above. Figure 75 shows the impulse response of detector M-7b. Ringing at 5 GHz was filtered out by the 3 GHz bandwidth preamp. Rise time (10% to 90%) was 550 ps and fall time (90% to 10%) was 1.1 ns. Pulse width at the base was 2.5 ns.

Figure 76 shows a plot of noise equivalent input power versus applied APD bias potential. A typical spot near the center had a minimum NEIP of 45 nW at optimum bias while the best hot spot had a minimum NEIP of only 5.3 nW. In both cases the signals were tightly focused with a 12 mm/f 2.7 lens with signal filling the aperture.

4.3.6 Hybrid Detector M-8a

Figure 77 shows the output waveforms of hybrid detector M-8a in response to the 400 Mbps communication system signal. Figure 78 shows the impulse response. Speed of response was faster than needed to return to the baseline between adjacent transmitted "1" pulses spaced 2.5 ns apart. Overshoot and ringing appeared to be slight, but some buildup was noticed with the occurrence of several adjacent pulses.

4.3.7 Hybrid Detector M-8b

Hybrid detector M-8b was inoperative as received. Manufacturer's measurements indicated that the pulse response was slightly faster than M-8a

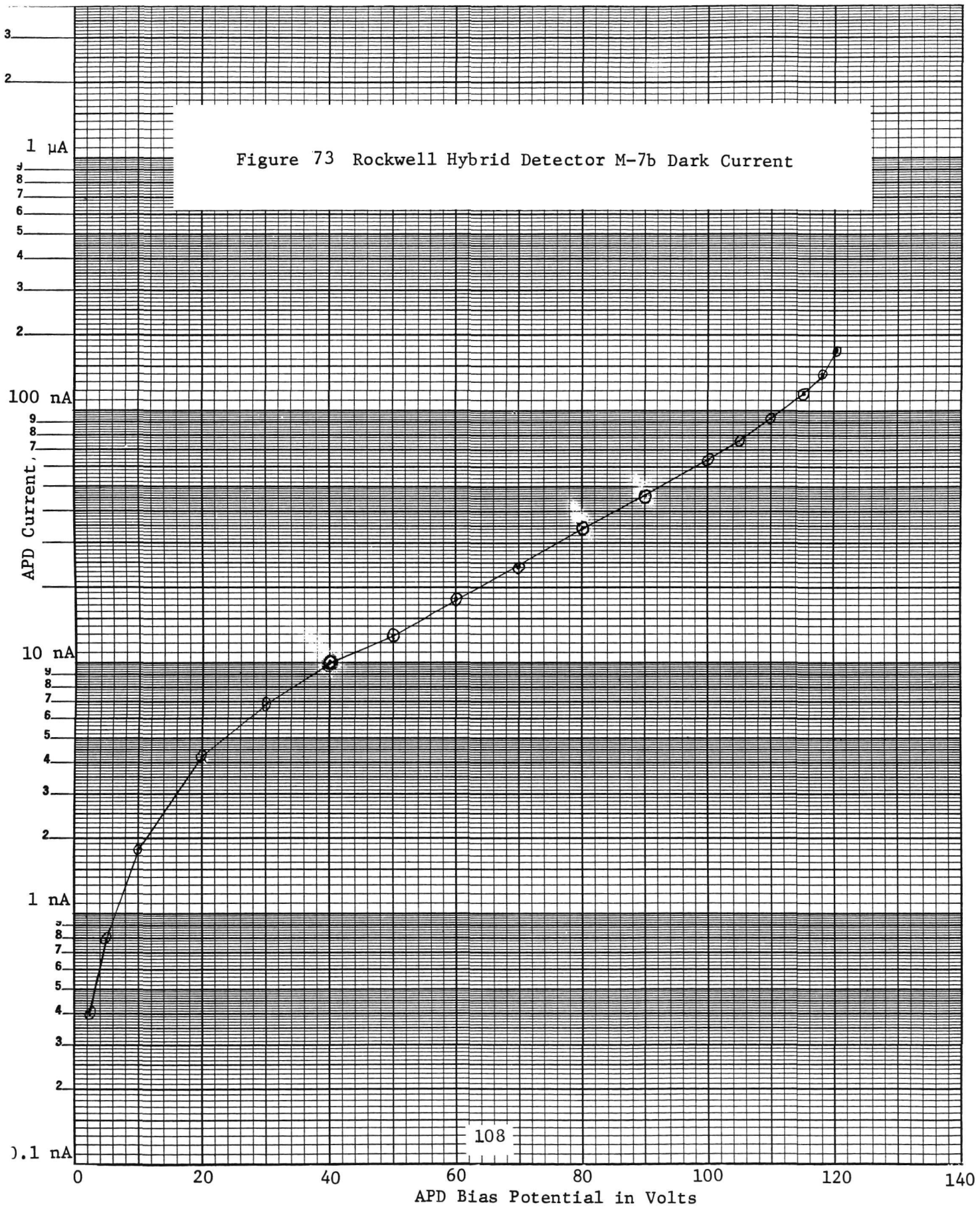

Figure 73 Rockwell Hybrid Detector M-7b Dark Current

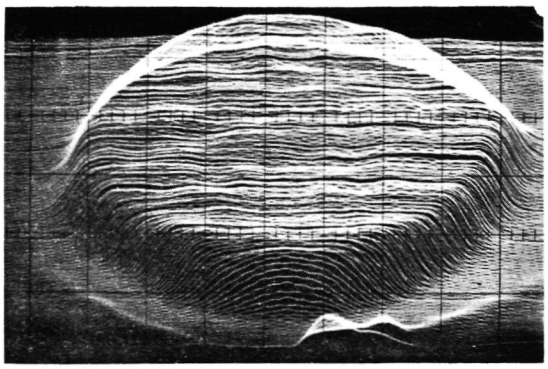

80 V
.36 μW

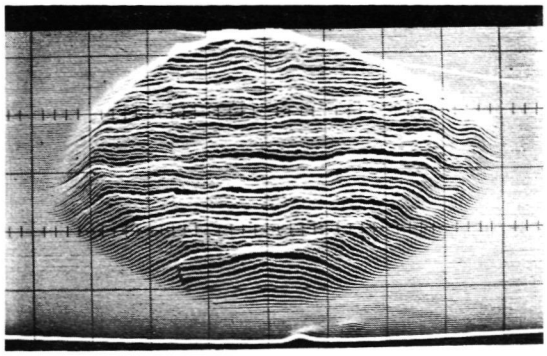

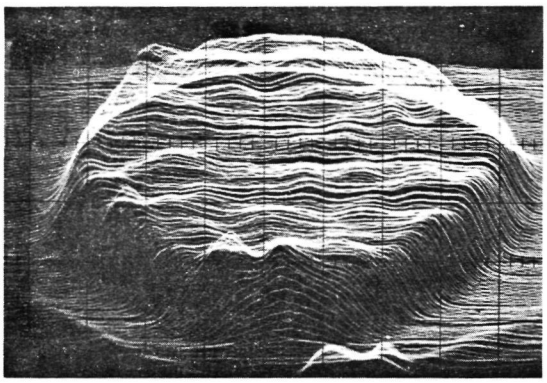

110 V
.36 μW

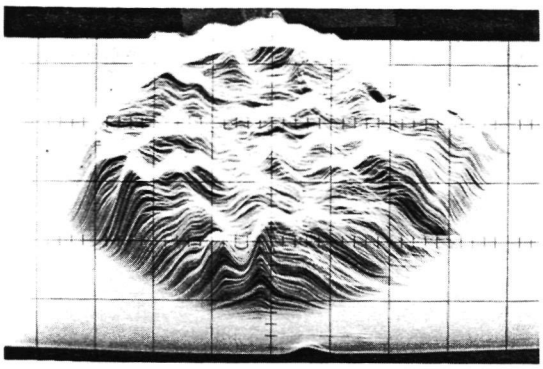

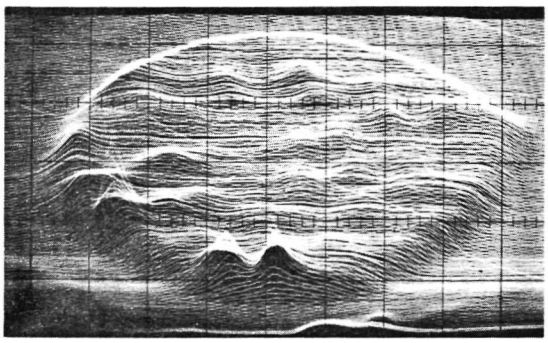

120 V
.12 μW

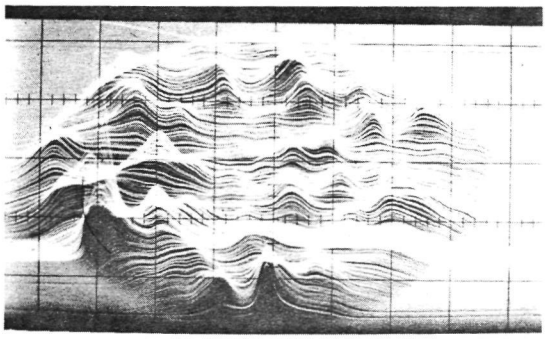

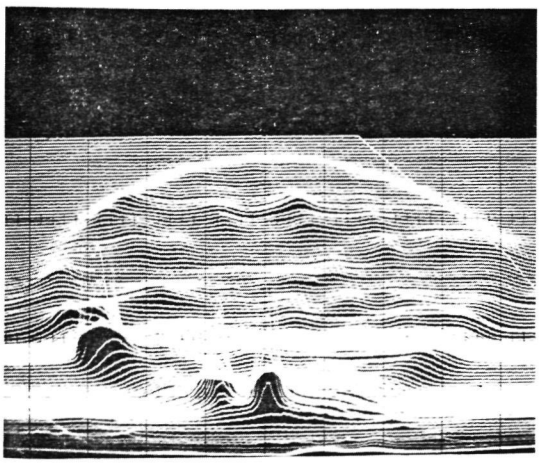

123 V
.12 μW

DC

200 MHz

Figure 74 Rockwell Hybrid Detector M-7b Photoresponse Scans

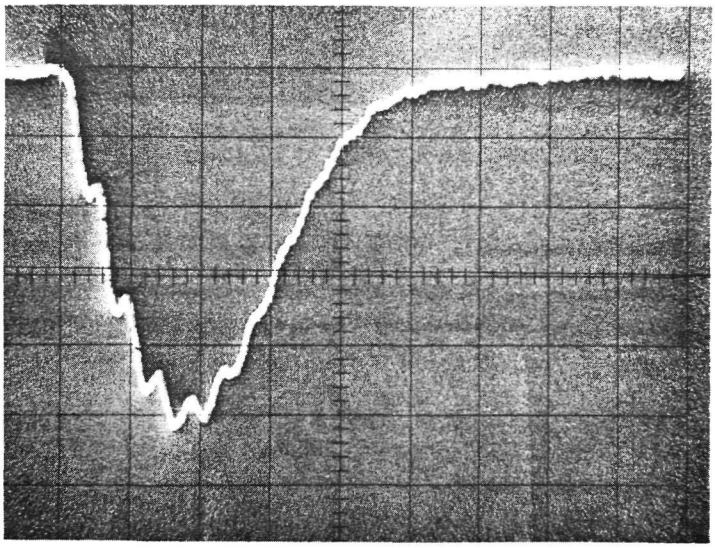

Without Preamp
28 mV/div
8.5 μA

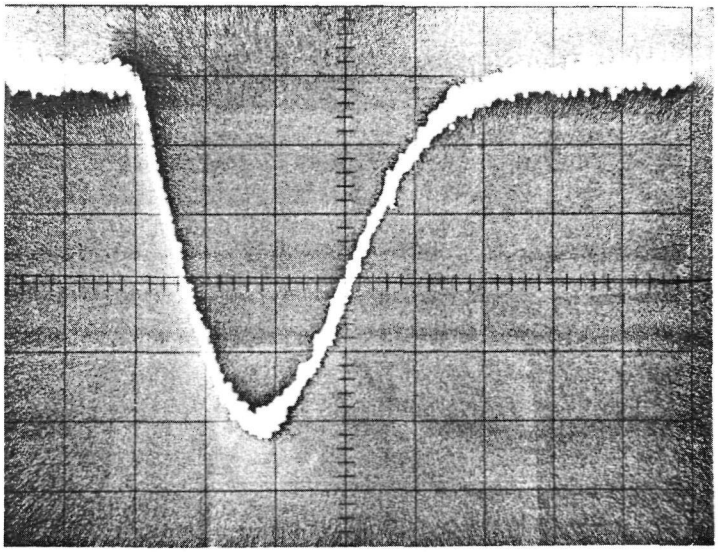

With B&H DC3002
Preamplifier and
3 dB Pad

2.8 mV/div

1 μA

Horizontal 500 ps/div.

Figure 75 Rockwell Hybrid Detector M-7b Impulse Response

FIGURE 76 ROCKWELL HYBRID DETECTOR M-7b NOISE EQUIVALENT INPUT POWER

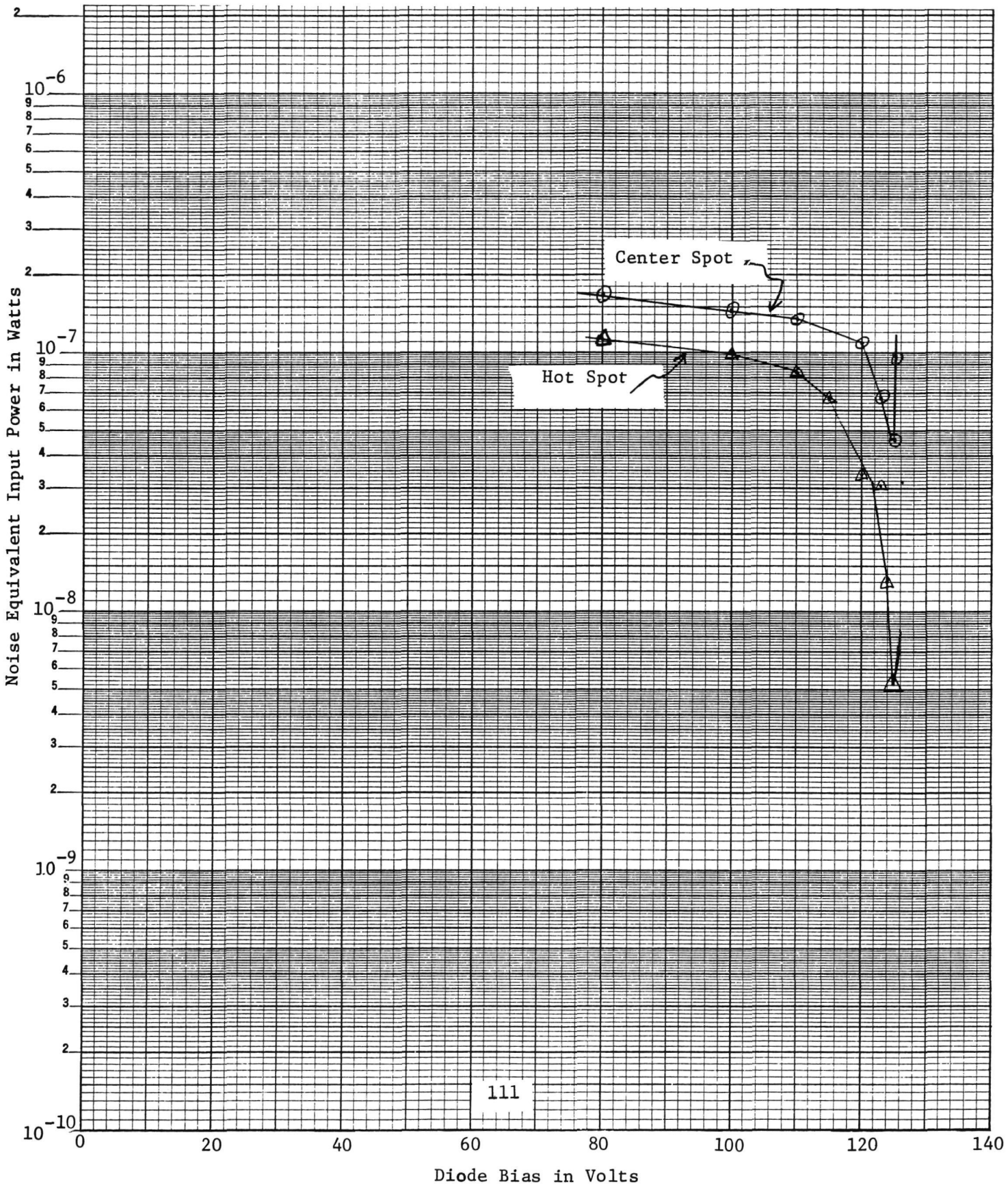

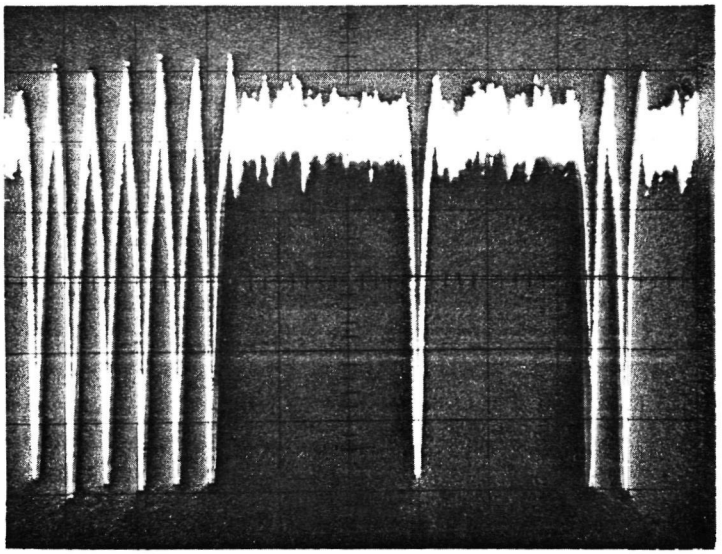

5 ns/div

Figure 77 Rockwell Hybrid Detector M-8a Output Waveform

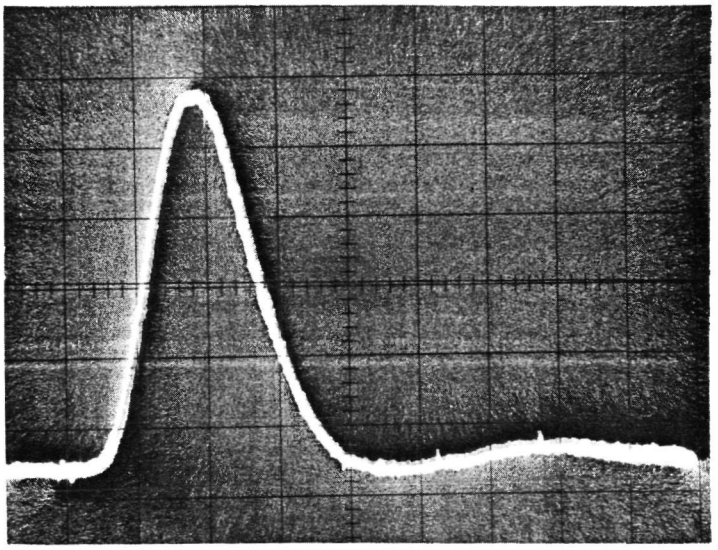

M-8 into B&H 3002 Prea
1 mV/div
0.5 ns/div
i = 1 μA

FIGURE 78 ROCKWELL HYBRID DETECTOR M-8a IMPULSE RESPONSE

REPRODUCIBILITY OF THE
ORIGINAL PAGE IS POOR

with better damping and no overshoot or ringing. Pulse width at 10% of maximum was 1.0 ns. The unit was returned to the manufacturer.

4.4 DISCUSSION OF PERFORMANCE

4.4.1 Avalanche Current Gain

The Rockwell hybrid detector is potentially an excellent detector for high data rate 1.064 μm communications. The 97% quantum efficiency attained by the inverted mesa structure GaAsSb APD is nearly perfect. The MESFET transimpedance preamplifier achieves significant gain. The limiting aspect of the hybrid detector is the poor avalanche gain performance achieved by the photodiode. Even at avalanche gains of 2 to 3 the response becomes nonuniform and gain above 5 is achieved only in a few very small areas. If high uniform avalanche gain could be obtained with this APD, communication system performance would be unsurpassed by any detector with lesser quantum efficiency. Dick Eden of Rockwell attributes the nonuniform avalanche gain performance to mismatches between the lattice constants of adjacent semiconductor layers. Selection of materials to provide better lattice matching in future diodes is expected to alleviate this problem. The performance expected should be superior to that presently achieved when focused on a hot spot.

4.4.2 MESFET 1/f Noise.

The hybrid preamplifiers contribute 1/f noise which decreases to the broadband noise level at about 35 MHz. The noise spectrum of hybrid detector M-7b is shown in Figure 79. The high 1/f noise is due to the recently developed GaAs microwave MESFET transistor, and should decrease as this new technology matures. In all cases, communication system performance was significantly improved by using a high pass filter in the post detection electronics. This consisted of either an Aventek AD-502 preamplifier with 5-500 MHz bandwidth or a series capacitor (.005 μF dc block) in 50 ohm line. The high pass filter could be used in system tests because, with a 63 bit repetitive code, the lowest frequency component was 6.35 MHz.

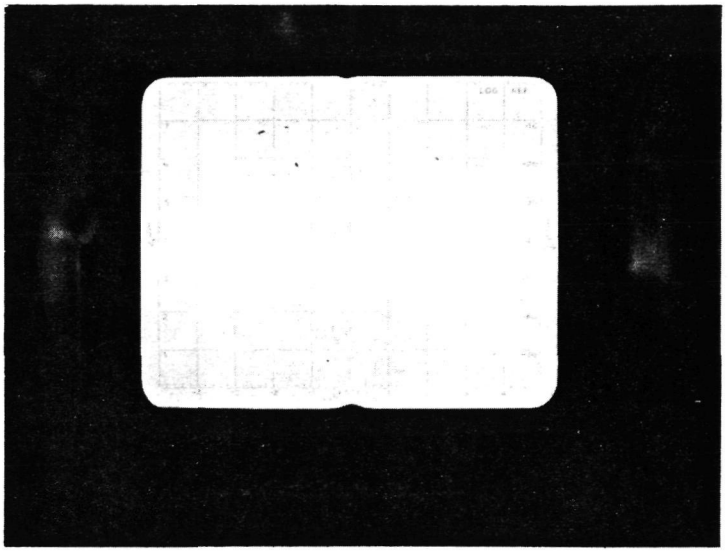

fo = 50 MHz Δf = 10 MHz/div
0 to 100 MHz displayed
Vertical 10 dB/div

FIGURE 79 ROCKWELL HYBRID DETECTOR M-7b NOISE SPECTRUM

REPRODUCIBILITY OF THE
ORIGINAL PAGE IS POOR

4.4.3 Gain and Bandwidth.

The best communication system performance was realized with hybrid detector M-7. This detector had the lowest bandwidth and the highest gain of all the hybrid detectors tested. Both parameters contributed to the superior performance. The 3 dB bandwidth of detector M-7 was 290 MHz, and the impulse response returned to the baseline in 2.5 ns, perfectly matched to the desired bit rate (as were all of the RCA detectors). Detector M-7 was the only hybrid detector to have an extra gain stage between the trans-impedance stage and the output (50 ohm line driver) stage. This extra stage raised the signal level by 13 dB, bringing it well above the noise of the following preamplifier and electromagnetic interference (EMI) from the laser transmitter. The Rockwell hybrid detectors appeared to be more susceptible to EMI than the detectors with high internal current gain mechanisms.

4.4.4 Comparison with Expected Results

In Table VIII are listed the estimated unity gain performance figures for the hybrid detectors. These figures were calculated by Dick Eden of Rockwell using the measured photodiode quantum efficiency, preamplifier noise, and preamplifier bandwidth, assuming the 1/f noise is removed by a high pass filter. In Table IX are listed the corresponding experimentally measured communication system performance figures. For comparison, the estimated and measured figures are summarized in Table X. Good agreement is observed for detectors M-5 and M-7. The poor agreement observed for detector M-4 is attributed to imperfections in the hybrid preamplifier. Note the unusual waveform from detector M-4 in Figure 64.

The quantum efficiency for M-8a measured by Rockwell is 80% of the value measured at MDAC because the photodiode was not properly centered in the input window. The active area was partially apertured during the Rockwell measurements. The estimated signal level for 10^{-6} Bit Error Rate appearing in parentheses is compensated for the increased quantum efficiency.

Rockwell predicted better performance with fast detectors such as M-8 than with slow detectors such as M-7 because their calculations assume a narrow pulse gated threshold detector which samples the detected signal at

its maximum and ignores the noise present at times of lower signal to noise ratio. In other words, post detection gating is assumed. Such gating was not successfully implemented. The threshold detector designed and fabricated for this program incorporated synchronous gating with selectable gate on times of 1.25 ns or 0.5 ns. In the narrower width mode, the threshold detector suffered from degraded threshold resolution, and no case was observed where performance improved at the narrower width.

To our knowledge, high repetion rate narrow pulse gating has not been implemented successfully, though present hybrid technology and GaAs MESFET microwave transistors might allow Rockwell to realize the desired circuitry within their detector package. If the estimated unity gain performance of M-8b could be demonstrated with post detection narrow pulse sampling, this would be the most sensitive approach with low avalanche gain and would be capable of bit rates greater than 1 Gbps.

In the case of M-7 where the detector bandwidth is tailored to the desired bit rate, Rockwell has demonstrated the ability to predict accurate communication system performance.

TABLE X

Rockwell Hybrid Detector Unity Gain Performance Comparison

Detector	Signal for 10^{-6} Bit Error Rate		Comments
	Estimated Photons/Pulse	Measured Photons/Pulse	
M-4	7200	13417	
M-5	6000	6367	
M-7a	4900	5324	Extra Gain Stage
M-7b	4900	5520	Extra Gain Stage
M-8a	8000 (6372)	9989	Quantum Efficiency Error
M-8b	3600	-	Widest Bandwidth, Defective

5. BIT ERROR RATE TESTING

5.1 MEASUREMENT EQUIPMENT

The laser transmitter used for communication system measurements is shown in Figure 80. The Laser Oscillator was a mode locked Nd:YAG laser with a pulse repetition frequency of 400 Mpps. The 1.064 μm laser was typically operated between 90 and 120 mW output with a pulse width of 330 ps at the 10% of maximum points.

A Master Clock Signal for the transmitter was derived from the Reference Timing Detector which sensed the laser radiation leaking through the high reflectivity laser end mirror. The master clock was a voltage controlled crystal oscillator which was phase locked to the detected reference signal.

The Electrooptical Modulator and Drive Electronics transmitted a 400 Mbps pseudorandom (PN) code in a pulse gated binary modulation (PGBM) format. A pulse was passed to transmit a logical "1", and a pulse was blocked to transmit a logical "0". The transmitter waveform is shown in Figure 81. The modulator and associated electronics were specially designed and fabricated for NASA GSFC under contract NAS5-20605 and were delivered at the conclusion of the measurement portion of this detector characterization program.

The modulated laser beam was collimated and transmitted to the receiver test bed. The signal was attenuated with a continuously variable Lambrecht KLOA-5 optical attenuator to a level suitable for measurements. The attenuated optical signal was focused onto the selected detector with a lens mounted on an XYZ translatable platform to provide fine control of spot position on the sensitive detector area.

A block diagram of the receiver and error detection electronics is shown in Figure 82.

The photomultiplier and photodiode detectors which required a dc coupled output were followed by a broadband 2 dB resistive attenuator pad to provide a dc path. The detected signal was then amplified by several wideband preamplifiers and passed through a Weinschel 908-100-4 wideband variable attenuator. The Hewlett Packard 35012 preamplifier had 26 dB gain and inverted the signal. The number of amplifiers used depended on the overall

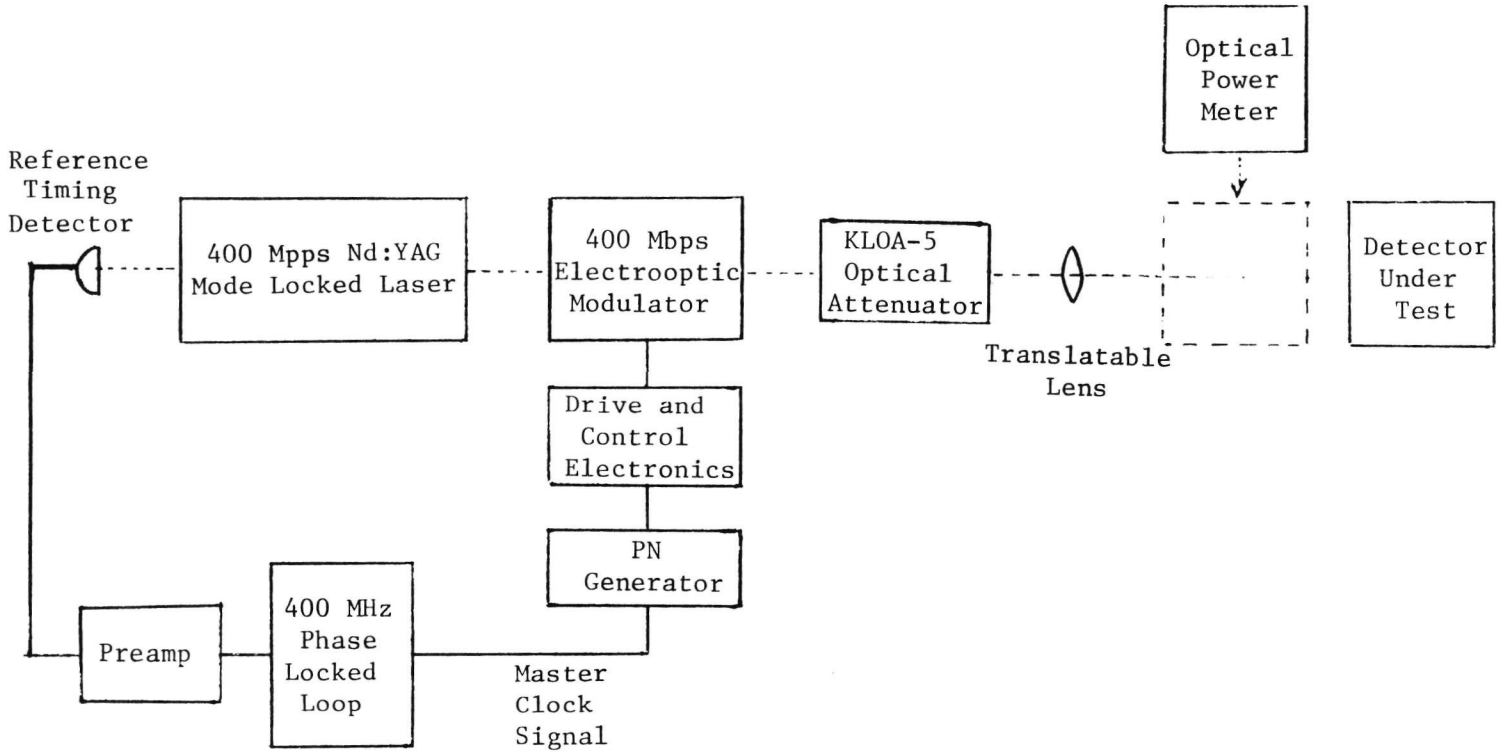

FIGURE 80 COMMUNICATION SYSTEM

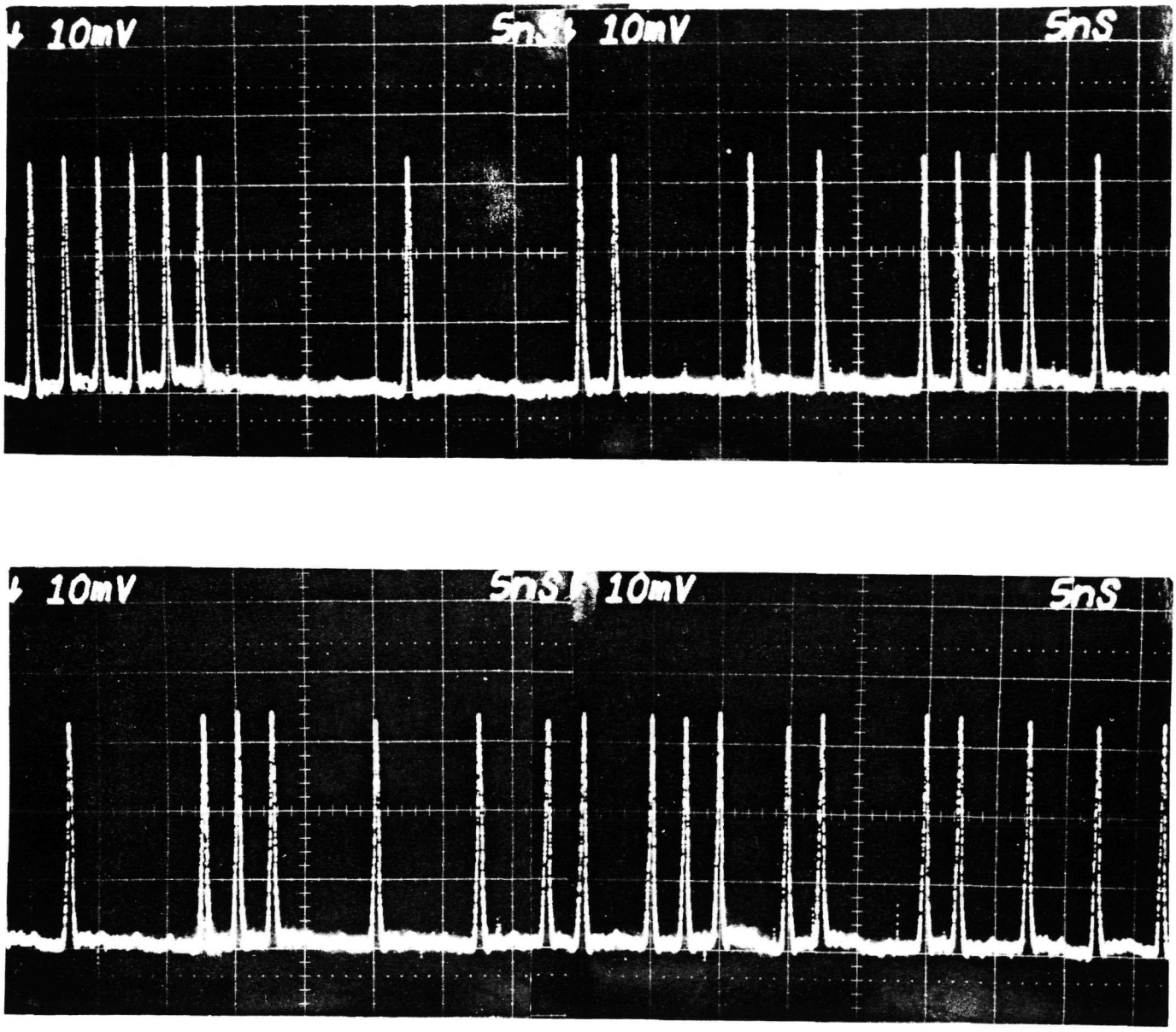

FIGURE 81 63 BIT 400 MBPS PGBM TRANSMITTER WAVEFORM
(p_1 AFTER 1099 HOURS OF CONTINUOUS OPERATION)

Worst Case Extinction Ratio - 30:1

Horizontal Scale - 5ns/div

Vertical Scale - 10mV/div

Detector - Rockwell M8-1D8

FIGURE 82 RECEIVER AND ERROR MEASUREMENT SYSTEM

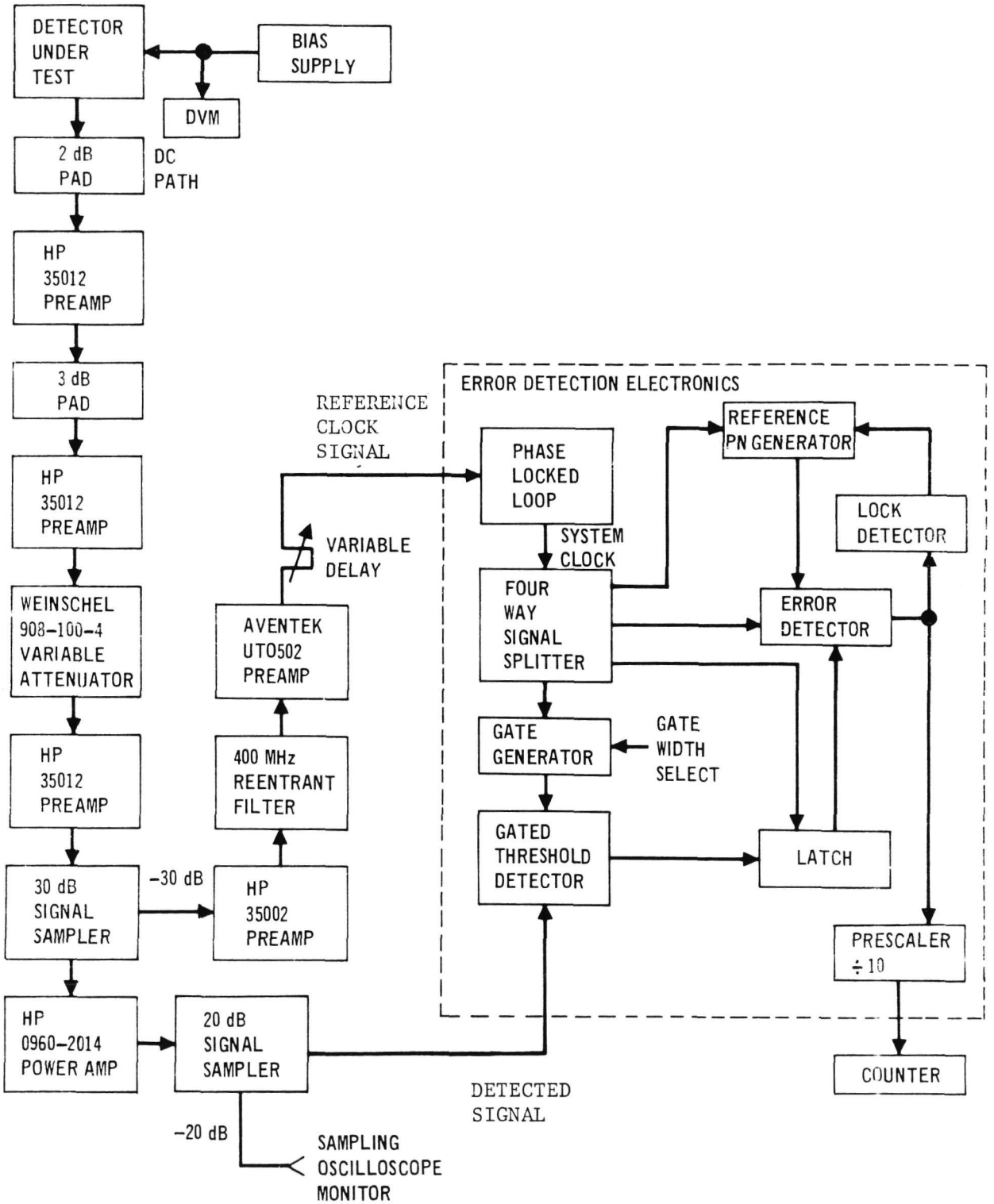

REPRODUCIBILITY OF THE ORIGINAL PAGE IS POOR

gain required and the polarity of the detector output signal. Most detectors had negative going signal pulses, but some had a positive going signal and required an additional inverting preamplifier.

A sample of the detected signal was sensed with a -30 dB broadband nondirectional resistive coupler and was amplified, passed through a selective 400 MHz filter and a trombone delay line before being fed to the Phase Locked Loop in the Error Detection Electronics. The detected signal was fed to the Gated Threshold Detector in the Error Detection Electronics.

The Error Detection Electronics consisted of a PGBM Bit Synchronizer, an Error Detector, a Reference PN Generator, a Lock Detector, and an Error Prescaler. The required data input was a 400 Mbps return to zero (RZ) signal with a 600 millivolt peak-to-peak amplitude. The phase-locked loop reconstructed a clean clock signal for use by the electronics from the filtered signal sample. The variable delay line in the clock input allowed precise alignment of input data and system clock signals.

The PGBM bit synchronizer consisted of a gated threshold detector followed by a data latch and the internal phase locked loop which generated the required clock signals. The gated threshold detector made the decision whether or not the input signal exceeded a threshold value during the time in which it was gated on. The gated threshold detector had internal feedback to latch itself into the detected state until the gate opened again. The output of the threshold detector went to a latch which generated reclocked nonreturn to zero (NRZ) data for the Error Detector. A gate generator was used to shape a sinewave clock into the gate pulse for the threshold detector. Either a narrow (0.5 ns) or wide (1.25 ns) gate width could be selected. The phase locked loop reconstructed a 400 MHz sinewave clock from the filtered data input. This clock signal was split into 4 components to clock the Reference PN Generator, the gate generator, the latch, and the error detector. The correct clock phasing was initially set by precisely determining the lengths of the various clock lines. The threshold detector shown in Figure 83 consisted of five emitter coupled transistor pairs, four of which served as differential amplifiers. The fifth acted as a control switch which gated the threshold

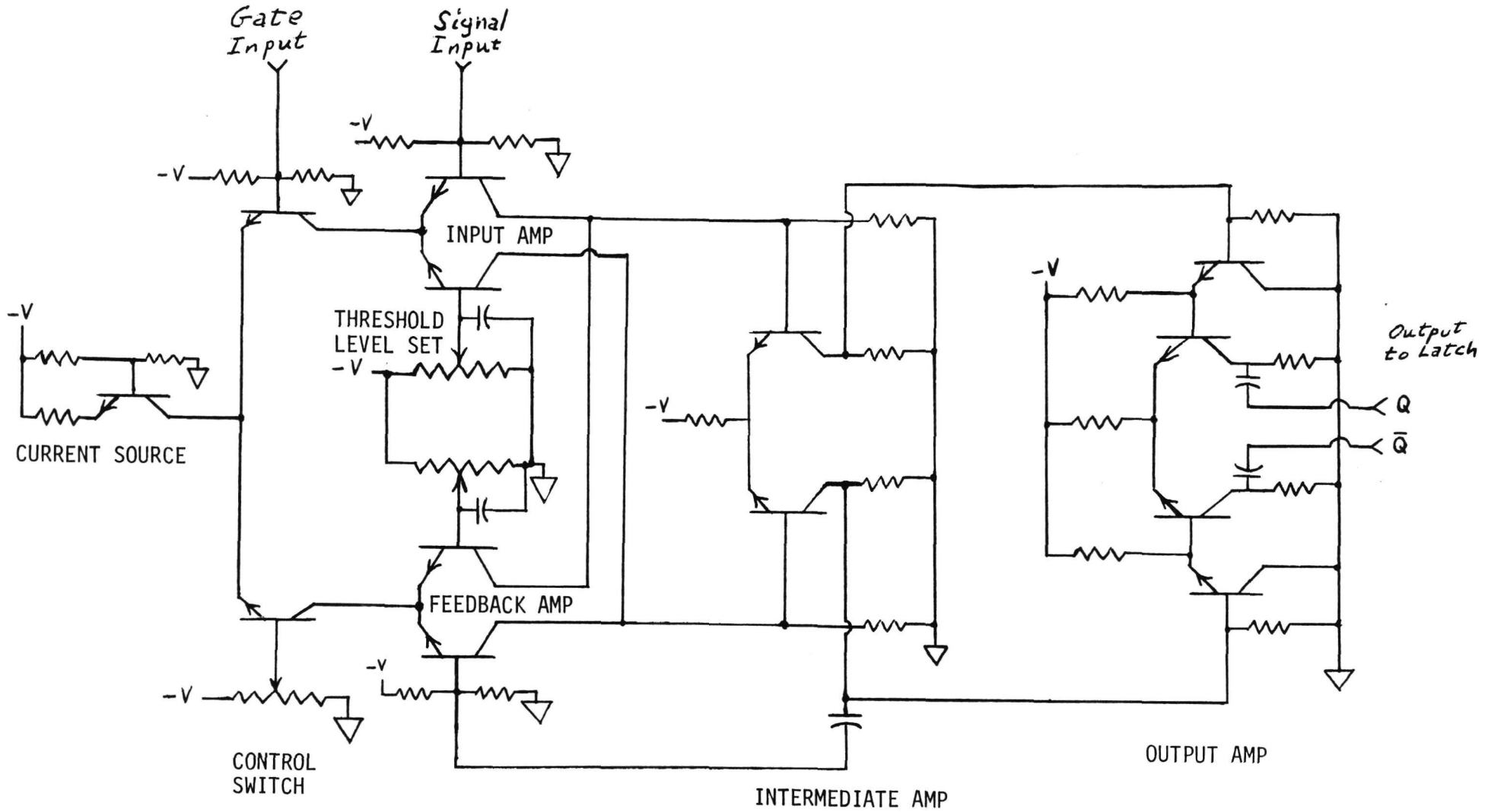

FIGURE 83 GATED HIGH SPEED THRESHOLD DETECTOR CIRCUIT

detector by transferring a current source between the input amplifier and the feedback amplifier. The amplifier enabled by the current source determined which signal drove the intermediate amplifier. When the gating signal was high, the control switch enabled the input amplifier which amplified the input signal relative to the threshold level. Additional gain was supplied by the intermediate amplifier. When the gating signal went low the control switch disabled the input amplifier and enabled the feedback amplifier which was driven from the output of the intermediate amplifier in a positive feedback arrangement which preserved or latched the state of the intermediate amplifier output while the gating signal remained low. While the gating signal was low, the threshold detector ignored the input signal. The output amplifier amplified the intermediate amplifier output to provide a good logic level output for the latch. The two selectable gate widths were approximately 50% and 20% of the 2.5 ns bit time.

The reconstructed data from the Gated Threshold Detector and Latch was compared with the reference data stream from the Reference PN Generator on a bit for bit basis by an exclusive OR gate in the Error Detector. If the two codes were alike in every bit, there was a constant low level out of the exclusive OR gate. When two bits were not alike, the exclusive OR gate went high indicating an error. The output of the exclusive OR gate was AND gated with the clock signal so that multiple sequential errors could be counted. The error signals from this AND gate were divided by ten in the Error Prescaler in order to allow the use of a low frequency counter (<40 MHz) to count the errors.

The six stage delay line type Reference PN Generator was designed to produce a 63 bit pseudorandom code at 400 Mbps. An identical code was used to modulate the laser transmitter. The output of an exclusive OR gate was connected to the D input of a D type flip flop which was clocked at a 400 MHz rate. The output of the flip flop was buffered and passed through two different delay paths which became the two inputs to the exclusive OR gate, thus forming a closed loop feedback generator capable of producing the desired pseudorandom code by proper adjustment of the delay line lengths. A

buffered output of the flip flop formed the Reference PN Generator output. The Reference PN Generator utilized the reset input on the D type flip flop to restart at an all ones sequence.

When the reconstructed pseudorandom code sequence and the reference pseudorandom code sequence were not in phase, a large number of error pulses were generated by the error detector. An integrator in the Lock Detector charged to a level proportional to the rate of occurance of errors. At a preset level, the lock detector reset the local PN Generator which then started at an arbitrary phase (1 of 63 possible states). The presence of a high number of errors repeatedly reset the PN Generator until it started in sequence with the reconstructed code from the Gated Threshold Detector. The number of errors was then much lower, so the PN generator continued to operate locked up in the proper phase. The threshold of error rate required for reset was very high so that error rate data could be taken at low signal levels without loss of lock. Initial acquisition time for lock up was a fraction of a second.

5.2 MEASUREMENT PROCEDURE

Each detector was operated in the measurement setup described above. The signal level into the Gated Threshold Detector was set to approximately 600 mV peak. The threshold detector decision level was initially set at about half this level. The detectors were initially operated at the manufacturer's recommended bias conditions after demonstrating acceptable performance at lower gain (under safer operating conditions). Bit error rate was displayed by a counter on the Error Prescaler output. An audio amplifier connected to this same output provided continuous aural monitoring of errors without constant attention to the counter display.

The threshold detector decision level was varied through its range by a ten turn potentiometer to minimize errors. The variable trombone delay line was adjusted through its range to minimize errors. This adjustment set the relative phase of the signal and the gating pulse in the Gated Threshold Detector. Once the delay was properly set for a particular detector, it required only minor readjustment. The threshold detector decision level required readjustment after any change in operating conditions because the required threshold level depended on the input signal level and the statistics of the noise in the input signal.

Detector operating conditions were then varied in order to achieve 10^{-6} bit error rate with the lowest possible optical signal power. The parameters varied were position of the focused signal spot on the detector photosensitive area and the detector operating bias potentials which controlled the gain and noise characteristics of the various detector types. Also, various input preamplifiers were tried in order to determine the effects of varying bandwidth and noise figure. After each change in a parameter, ths signal attenuator was adjusted to set the signal level into the Gated Threshold Detector to about 600 mV. A portion of this signal was monitored on a sampling oscilloscope to aid in setting the proper level. Then the threshold detector decision level and the trombone delay were iteratively adjusted to minimize errors. The optimum operating conditions were determined for each detector by varying the operating parameters in all possible combinations of ways to achieve minimum

error rate. When the operating conditions were optimized for 10^{-6} bit error rate, a data run was made. Signal level was varied to set the bit error rate to 10^{-3}, 10^{-4}, 10^{-5}, 10^{-6}, 10^{-7}, and 10^{-8}. At each level the attenuator and the threshold detector decision level were reoptimized. Input optical signal power was measured by an EGG 575-22 power meter (which has been determined to be accurate at 1.064 μm by radiometric calibration and by intercomparison with three similar meters in our laboratory). A long focal length lens was used with the larger area detectors (RCA and Varian), and the optical power meter was inserted in front of the detector to measure signal level. A short focal length lens was used with small area detectors (Rockwell) to achieve small spot size, and the optical power meter was inserted behind a pinhole aperture of the same size and in the same position as the active area of the detector under test. This latter technique was recommended by Dick Eden of Rockwell to eliminate extraneous light which passed through the lens but was not focused on the active area of the detector.

The resulting data was plotted as probability of error per bit versus input optical signal power and is commonly called a bit error rate plot.

6. UNIT TESTING

6.1 DARK CURRENT

The dark anode current of the photomultiplier detectors was measured with a Kiethly 414S picoammeter. The cathode was kept dark by a piece of black photographic tape over the window. The photomultiplier was operated at the electrode potentials and current gain recommended by the manufacturer. The measured dark anode current divided by the current gain equals the dark cathode current.

The dark current of the photodiode detectors was measured with a Kiethly 602 floating picoammeter and a variable dc bias supply. The photosensitive area was kept dark by a piece of black photographic tape over the window. Dark diode current was measured as a function of diode bias potential from low gain up through the maximum useable avalanche gain.

The RCA photodiodes were also illuminated with about 0.1 μw of 1.064 μm radiation to illustrate the change in responsivity with increasing bias as the difference between the illuminated and dark current versus voltage curves. The signal level was determined on the basis of the manufacturer's responsivity figures, so these curves cannot be used as an absolute measure of responsivity.

6.2 SCANNING

Scans of detector response were made with the setup shown in Figure 84. A laser beam was raster scanned by two galvanometer driver mirrors with normal axes. The scanning mirror drive signals were the two sawtooth sweep signals from a Tektronix 556 dual beam oscilloscope. A similar raster scan was generated on the oscilloscope CRT by using the same two sweep signals as horizontal and vertical deflection signals; the faster Sweep A drove the horizontal, and the slower Sweep B was applied to one differential input of a plug in vertical preamplifier (1A1). The alternate differential input was the photocurrent from the detector under test in response to the scanned light beam. The slow vertical sweep signal and the detected photocurrent signal were added algebraically so that deviation (up) from the original baseline raster was proportional to the detected signal and therefore to the photoresponse at that point.

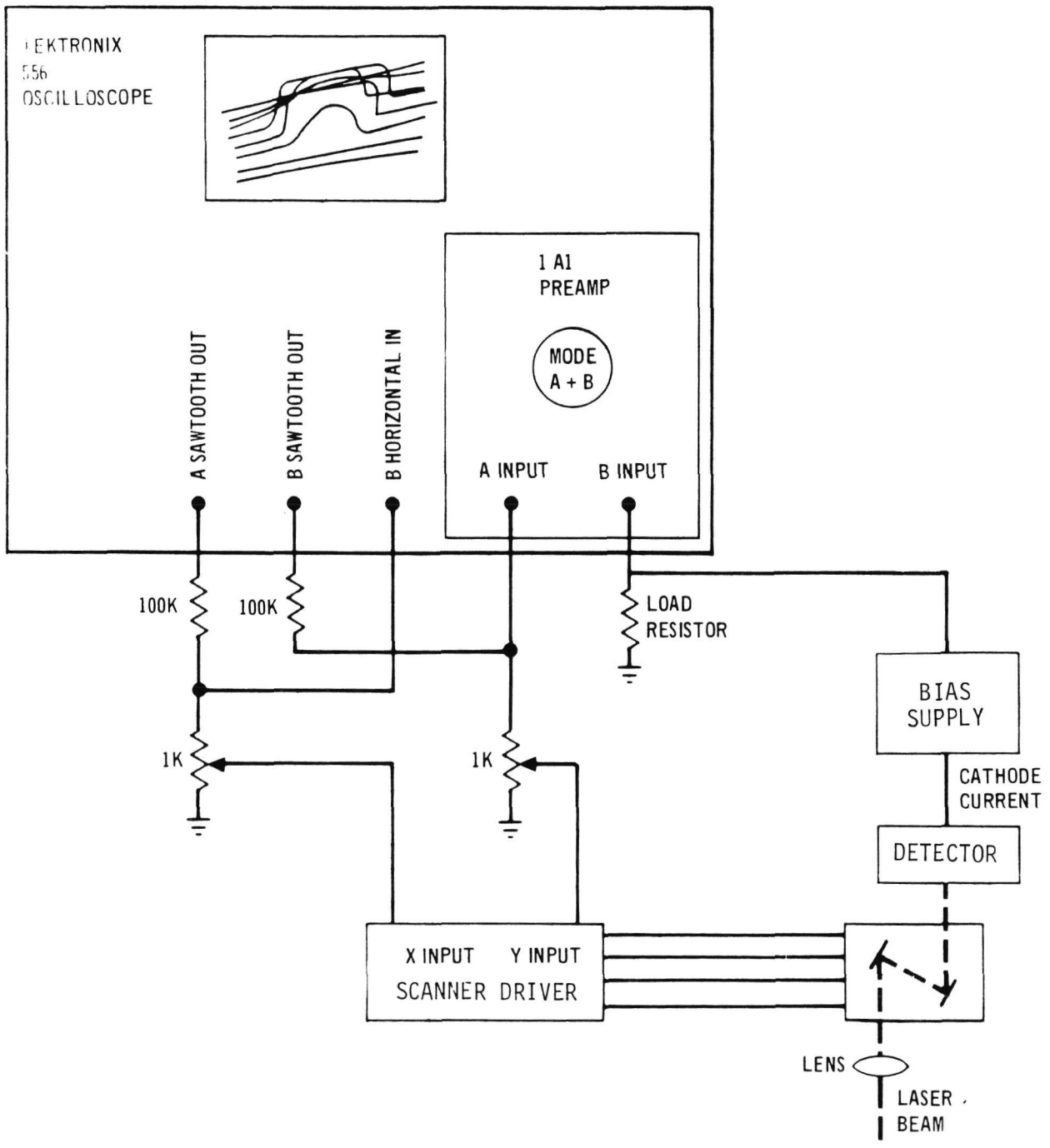

FIGURE 84 PHOTORESPONSE SCANNER

Scans of photomultiplier quantum efficiency were made by monitoring cathode photocurrent with the tube off. Scans of photomultiplier output were made by monitoring anode current. The differences between these two scans showed the variation in electron multiplier gain as a function of input spot position on the photocathodes.

Scans of photodiode response were made monitoring diode photocurrent. At low bias the Rockwell APD had unity gain so that the very uniform quantum efficiency was displayed. At higher bias the photocurrent rose nonuniformly showing the variation in gain as a function of position. At low bias the RCA APD would not operate down to unity gain so that its quantum efficiency could not be observed directly, however at moderate bias and low gain the response was uniform indicating that the quantum efficiency was uniform.

The laser beam to the scanner was amplitude modulated at 200 MHz as required for the noise measurements described below. This did not affect the scans of detector photoresponse or anode response, and it did allow a measure of the detector response at 200 MHz. The detector output signal, taken from the anode of the Varian photomultiplier, the preamplifier of the Rockwell hybrid detector, and the cathode of the RCA APD, was amplified and filtered to extract the 200 MHz component which was then square law detected and applied to the alternate differential input of the oscilloscope preamplifier. The resulting scan showed the photoresponse times the gain at 200 MHz. Any differences between the shape of this scan and the shape of the baseband output scan described above was due to differential variations in frequency response as a function of cathode spot position, though some nonlinearity was observed due to square law detection.*

6.3 OUTPUT WAVEFORMS

The output waveform of each detector was recorded with a Tektronix sampling oscilloscope using an S6 sampling head which had a 30 ps risetime and a virtually perfect 50 ohm termination. Output waveforms were recorded in response to the encoded 400 Mbps transmitter signal. The same portion of the

* A logical extension of this technique has been used in this laboratory to generate a scan showing the variation in time delay through a photomultiplier detector as a function of cathode spot position but was not used on this program.

recurring 63 bit code was recorded in each case. One or more preamplifiers were utilized between the detector and sampling head when required to raise the signal level. The preamplifier type used was the HP 35012 with bandwidth from 0.1 to 1300 MHz in order to preserve the fidelity of the detected waveform.

Several measurements of impulse response were made late in the program to determine accurate waveforms of the various detector type. A narrow pulse mode locked Nd:YAG laser operating at 200 Mpps was used as the signal source to eliminate the intersymbol interference experienced with the closer pulse spacing in the 400 Mpps laser provided for this program. A wider bandwidth preamplifier provided by Dick Eden of Rockwell was used when necessary. The preamplifier type used was the B & H model 3002 which had a bandwidth from dc to 3000 MHz. A 2 dB pad and a 3 dB pad were cascaded between the detector output and the wideband preamplifier input to diminish the adverse effects of poor preamplifier input VSWR. The accuracy of the waveforms derived in this series of measurements was more accurate than of those made earlier. Only the following detectors were available for the improved impulse response measurement: F1, F2, DF1, DF2, HF2 and HF3 from RCA, M4, and M7 from Rockwell, and S/N 031 from Varian. All other waveforms designated impulse response were expanded waveforms of an isolated "1" pulse in the encoded 400 Mbps pulse train.

The waveform of the 200 Mpps mode locked laser used for the improved impulse response measurements is shown in Figure 85 as detected by a Rockwell GaAsSb APD supplied as GFE for a related program.

6.4 NOISE EQUIVALENT INPUT POWER

The noise equivalent input power (NEIP) of a detector is the amount of signal required to double the detector output noise power in a standard bandwidth. For this measurement, each detector was mated with the same low noise preamplifier, an Avantek AD-502 with a 2.2 dB noise figure and a bandwidth from 5 to 500 MHz. The preamplifier output was fed to a 200 MHz low pass filter to set the bandwidth of the measurement and amplified again. The signal ultimately went to a wideband RF power meter. The meter provided a relative reading of detector output power with no signal. Signal was then increased until the power level indicated on the meter increased by 3 dB.

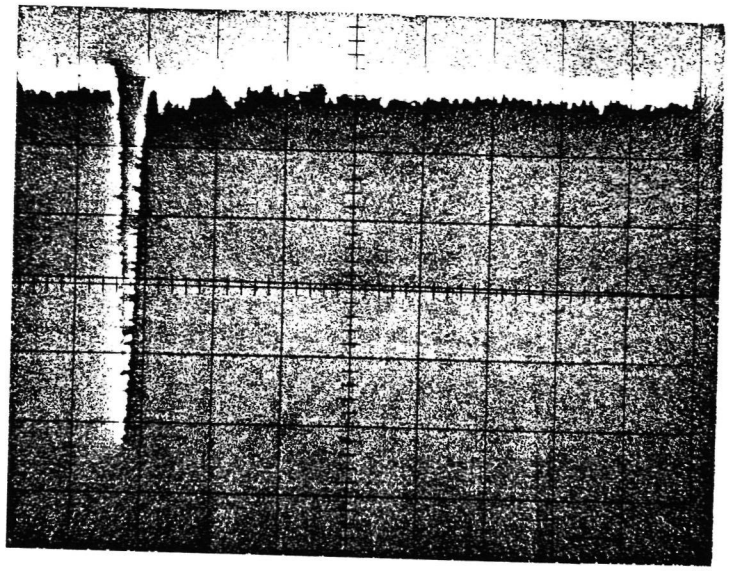

500 ps/div

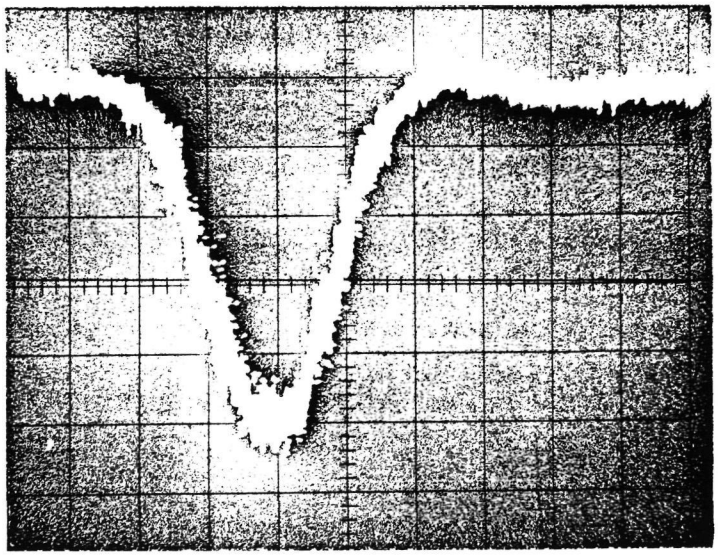

50 ps/div

Detector - Rockwell M8-1D8

Figure 85 Reference Impulse Signal for Response Measurements

A CW optical signal would not serve for this measurement since the major signal component is at dc which is not in the passband of the preamplifiers or the power meter. Therefore the signal was amplitude modulated at 200 MHz, within the passband of the measurement system. The NEIP of each detector was measured in the setup shown in Figure 86. A stable CW Nd:YAG laser beam was passed through an acoustooptic modulator, a quartz block with an acoustic transducer on the side driven at 100 MHz. A standing wave of acoustic energy existed within the block. A portion of the laser output beam which passed through the sound column was Bragg diffracted at an angle to the main beam, which was subsequently trapped. The diffracted beam from the acoustooptic modulator was fully amplitude modulated at twice the drive frequency. The deflection angle depended on the drive frequency, and the fraction of power in the diffracted beam was proportional to the acoustooptic modulator drive power. This technique was selected because the modulation depth was invariant and thus did not need to be measured.

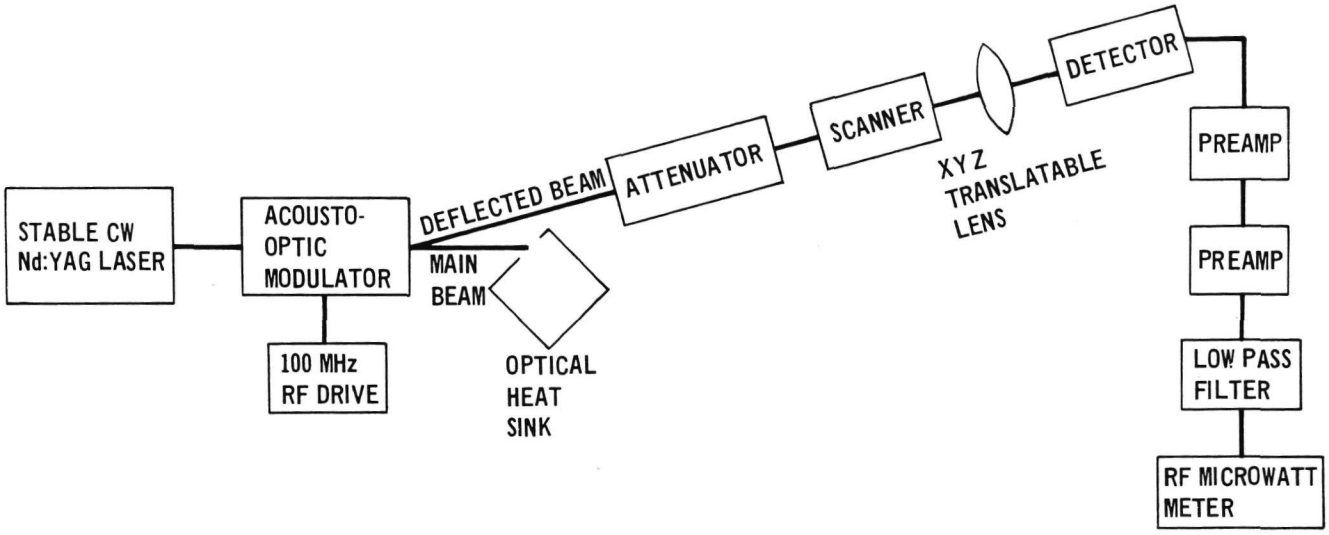

FIGURE 86 1.064 μm NOISE EQUIVALENT INPUT POWER MEASUREMENT

6.5 NOISE EQUIVALENT INPUT POWER VERSUS PHOTOCURRENT

The measurement of dark NEIP described in the proceeding paragraph is a useful figure of merit for detectors used in low average signal level applications such as ranging or acquisition with a dark field of view. However, a communications detector is operated at a relatively high average photocurrent because of the continuous nature of data transmission. Shot noise in the signal is proportional to the square root of the detected photocurrent and is ideally governed by Poisson statistics. A detector with a high internal current gain, such as the Varian PMT or the RCA APD, can amplify the shot noise to a level comparable to or higher than the Gaussian (resistor) noise of the following preamplifier. The noise of the high gain detector is therefore dependent on the input signal level.

Measurements of the NEIP in the presence of background were made for the high gain detectors and plotted as a function of background photocurrent level. A CW background source was used to generate this photocurrent. The results are presented separately in this section because they are of questionable accuracy and of dubious worth.

6.5.1 RCA Avalanche Photodiodes

The NEIP versus background current data for the RCA silicon APD detectors is plotted in Figures 87 through 92. The theoretical limit of performance based on the 200 MHz measurement bandwidth and the bulk dark current appears as a horizontal line in each plot. The theoretical limit of performance based on the 200 MHz measurement bandwidth and the quantum efficiency appears as a line of slope one-half in each plot. The combined limit of theoretical performance appears as a dashed line.

Agreement with experimental data was good for F1 and DF1 and poor for F2 and DF2. The dark NEIP was closely related to the dark bulk leakage current limit for the room temperature detectors. HF2 and HF3 were operated at +80°C and performed well above the limit set by the bulk leakage component of the dark current.

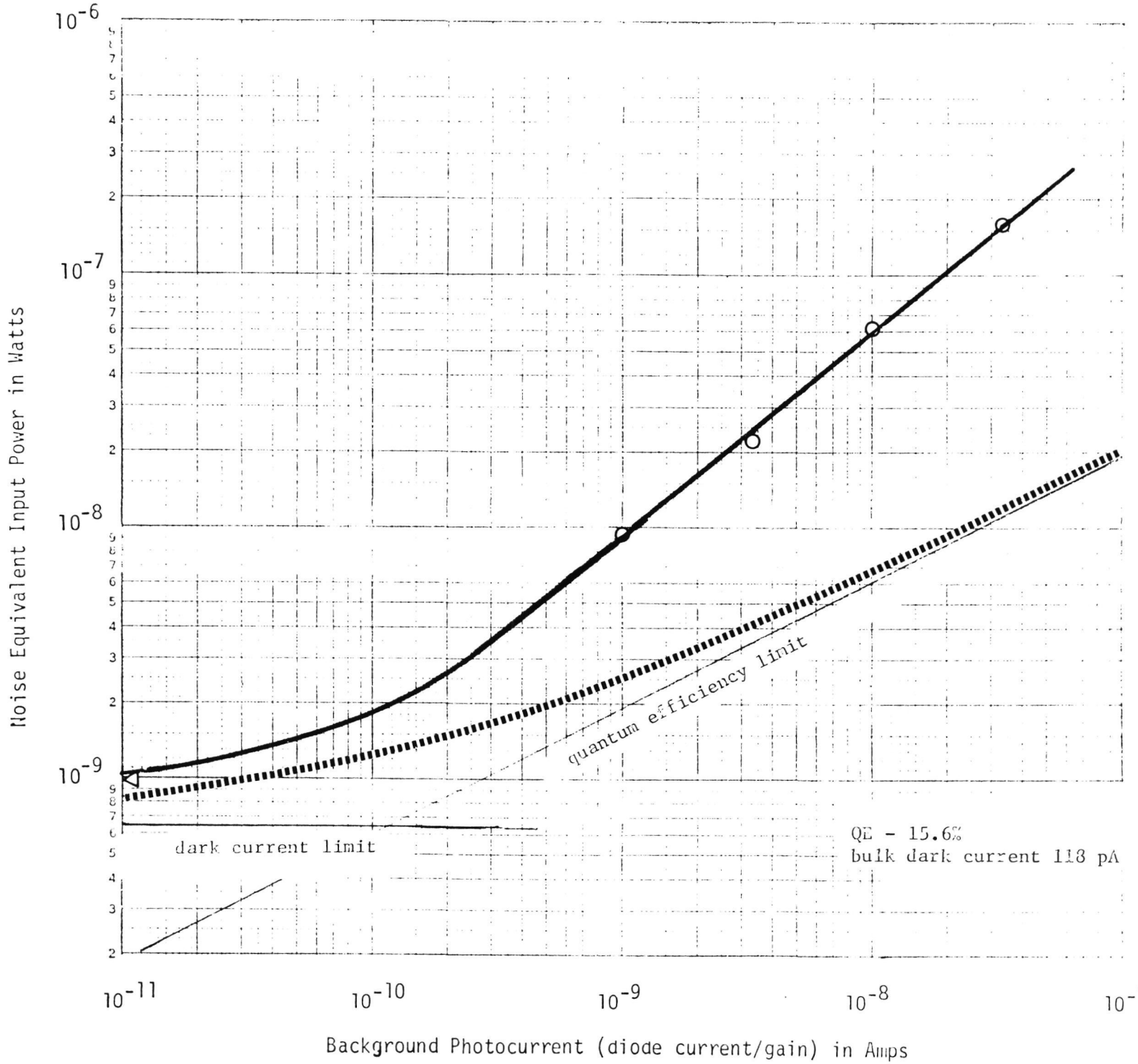

FIGURE 87 RCA SILICON APD F1 NEIP VERSUS BACKGROUND PHOTOCURRENT

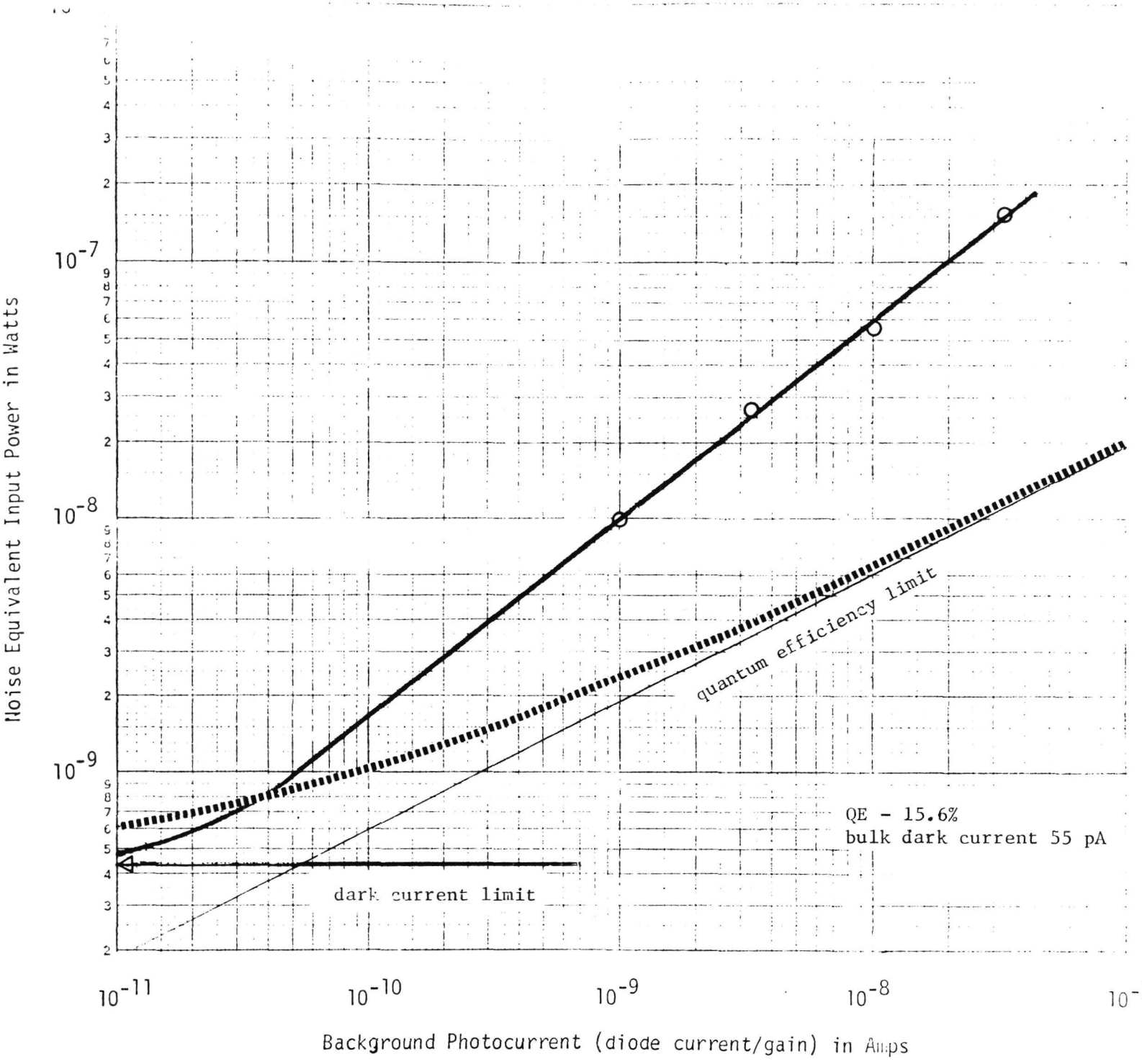

FIGURE 88 RCA SILICON APD F2 NEIP VERSUS BACKGROUND PHOTOCURRENT

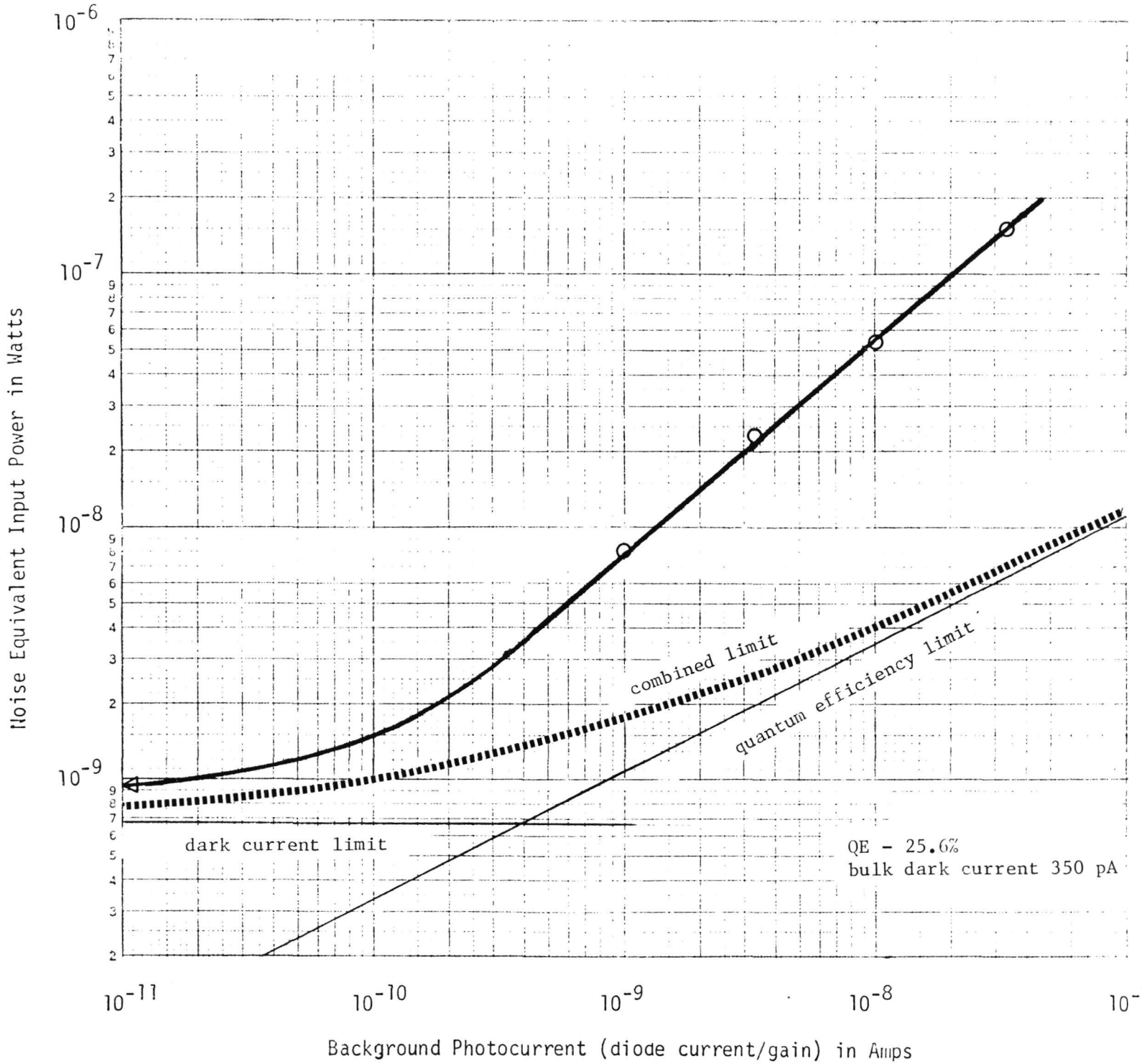

FIGURE 89 RCA SILICON APD DF1 NEIP VERSUS BACKGROUND PHOTOCURRENT

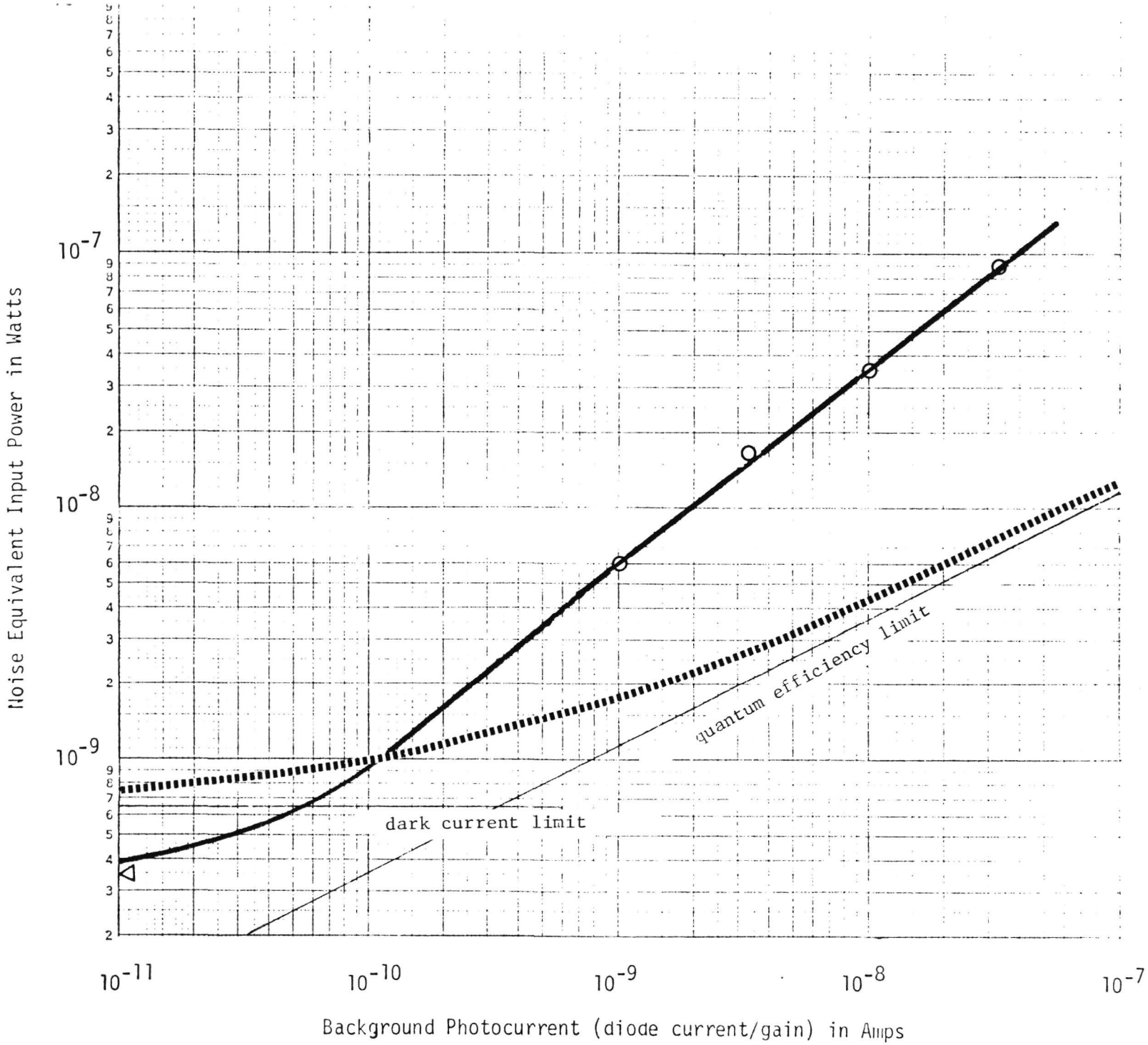

FIGURE 90 RCA SILICON APD DF2 NEIP VERSUS BACKGROUND PHOTOCURRENT

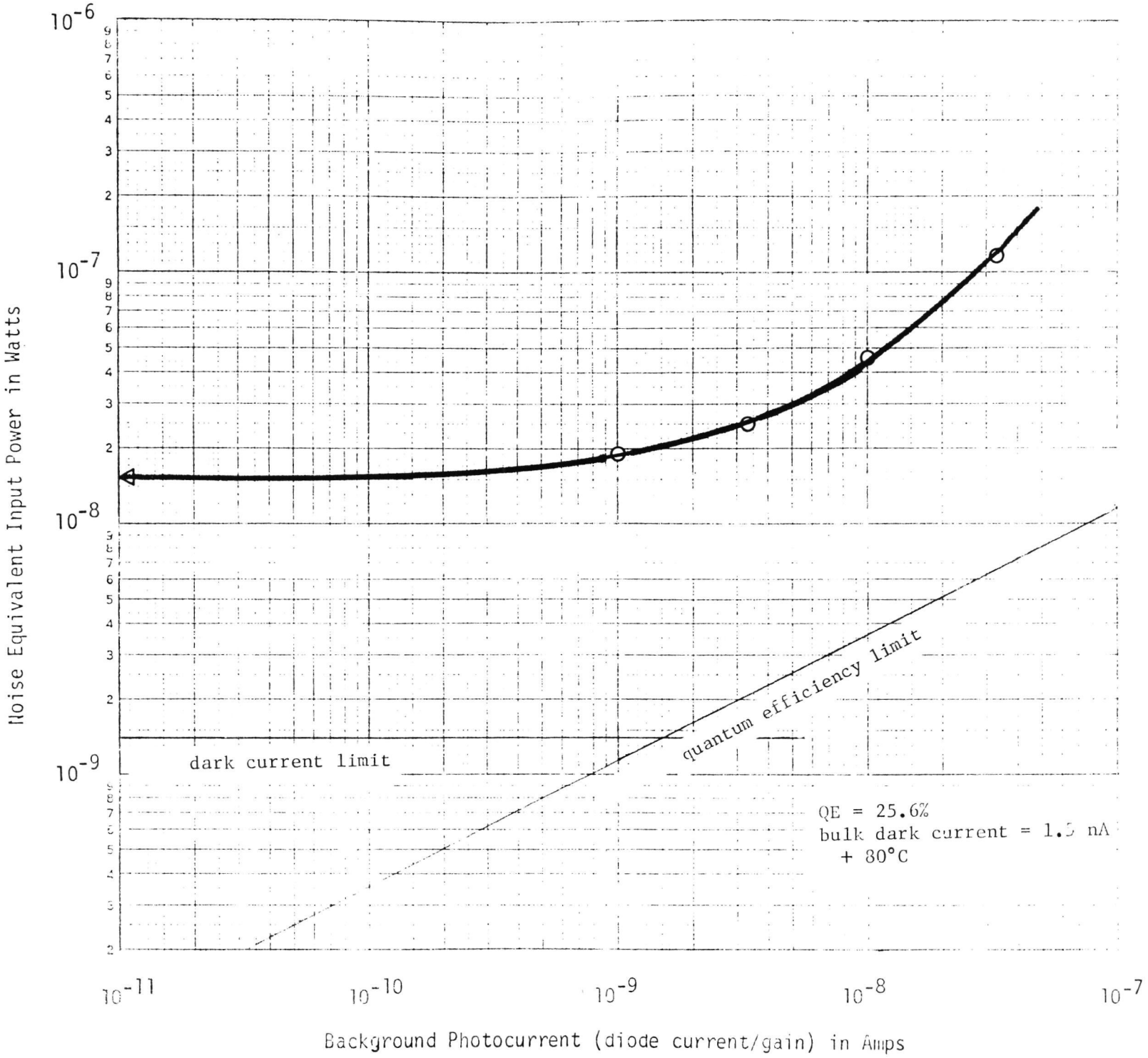

FIGURE 91 RCA SILICON APD HF2 NEIP VERSUS BACKGROUND PHOTOCURRENT

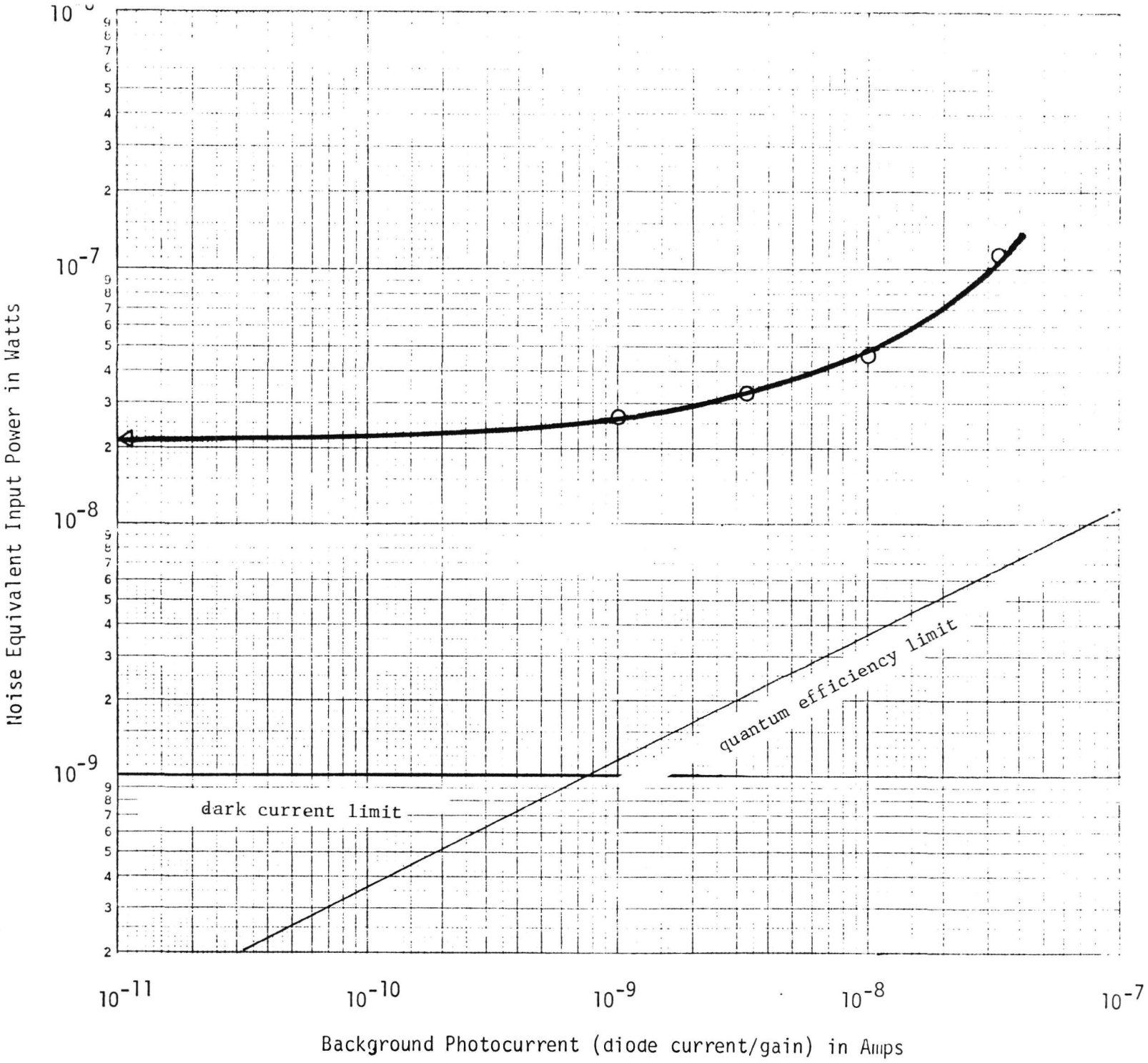

FIGURE 92 RCA SILICON APD HF3 NEIP VERSUS BACKGROUND PHOTOCURRENT

The slope of the curves at high background level is much greater than one-half. The reason for this behavior is not understood.

6.5.2 Varian Photomultipliers

The NEIP versus background photocurrent data for VPM 152A S/N 028 is plotted in Figure 93. The dashed line shows the best theoretical behavior expected on the basis of a 0.017% quantum efficiency, a 0.4 nA dark current, and a 200 MHz measurement bandwidth.

The NEIP versus background photocurrent data for VPM 152A S/N 031 is plotted in Figure 94 at rated gain and at reduced gain. The dashed line shows the best theoretical behavior expected on the basis of a 0.11% quantum efficiency, a 180 pA dark current, and a 200 MHz measurement bandwidth. At higher signal levels, both experimental curves deviate upwards sharply as signal induced noise generation increases due to the increased tube current.

The NEIP versus background photocurrent data for VPM 152A S/N 035 is plotted in Figure 95 at rated gain. The dashed line shows the best theoretical behavior expected on the basis of a 2.17% quantum efficiency, a 6.2 pA dark current, and a 200 MHz measurement bandwidth. As mentioned earlier, the dark NEIP was 500 times higher than expected. There was some unexplained error associated with this set of measurements.

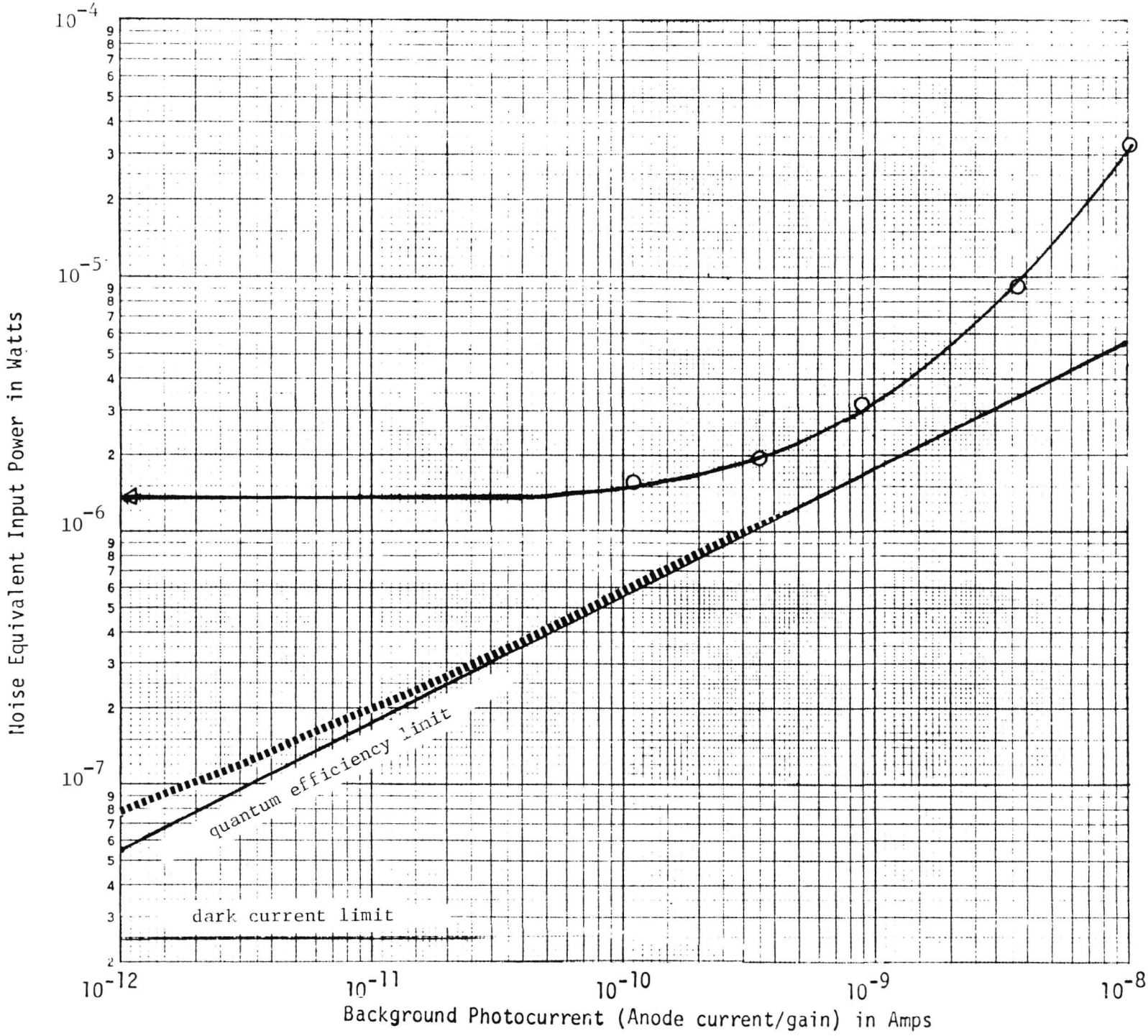

FIGURE 93 VPM 152A S/N 028 NEIP VERSUS BACKGROUND PHOTOCURRENT

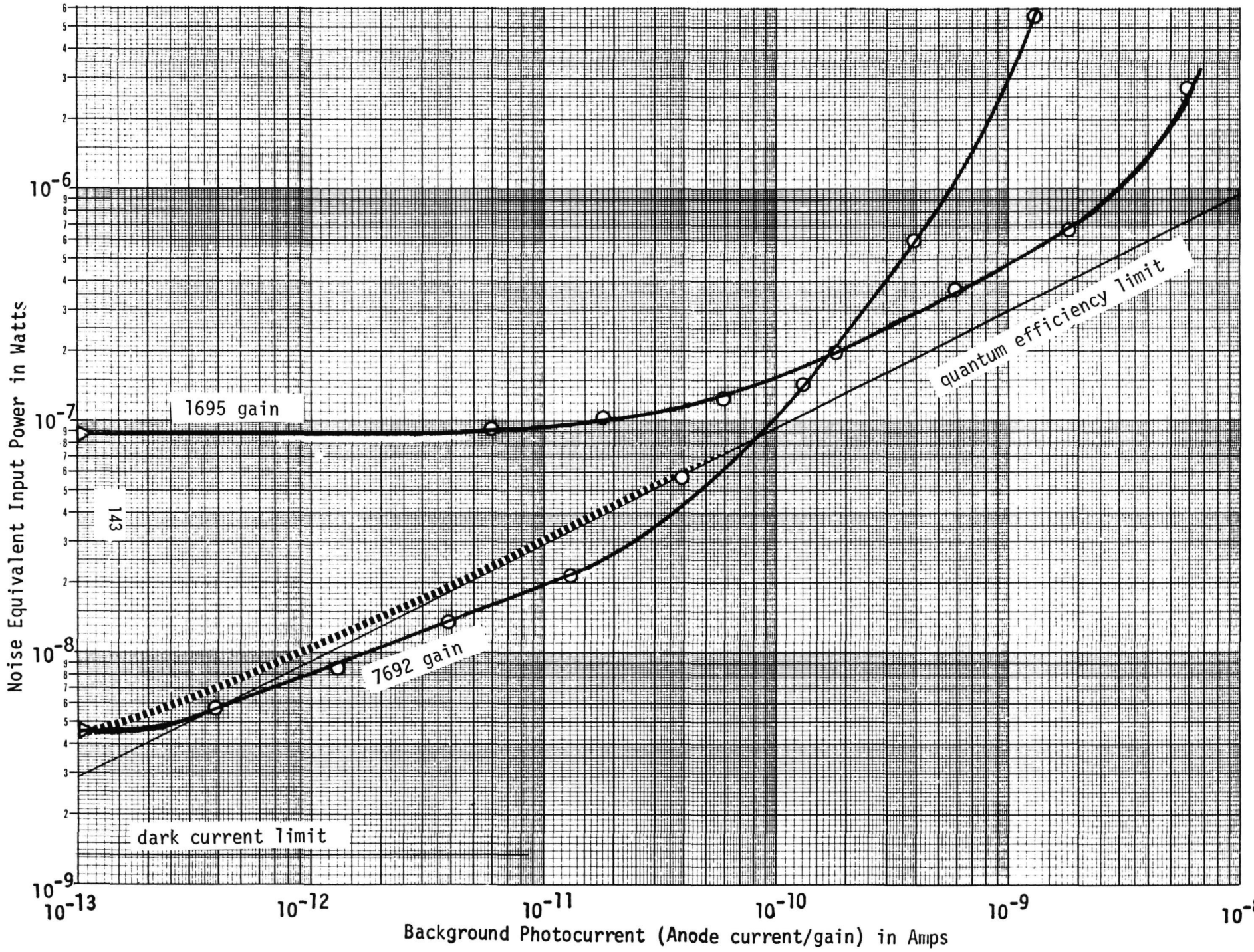

FIGURE 94 VPM 152A S/N 031 NEIP VERSUS PHOTOCURRENT

REPRODUCIBILITY OF THE ORIGINAL PAGE IS POOR

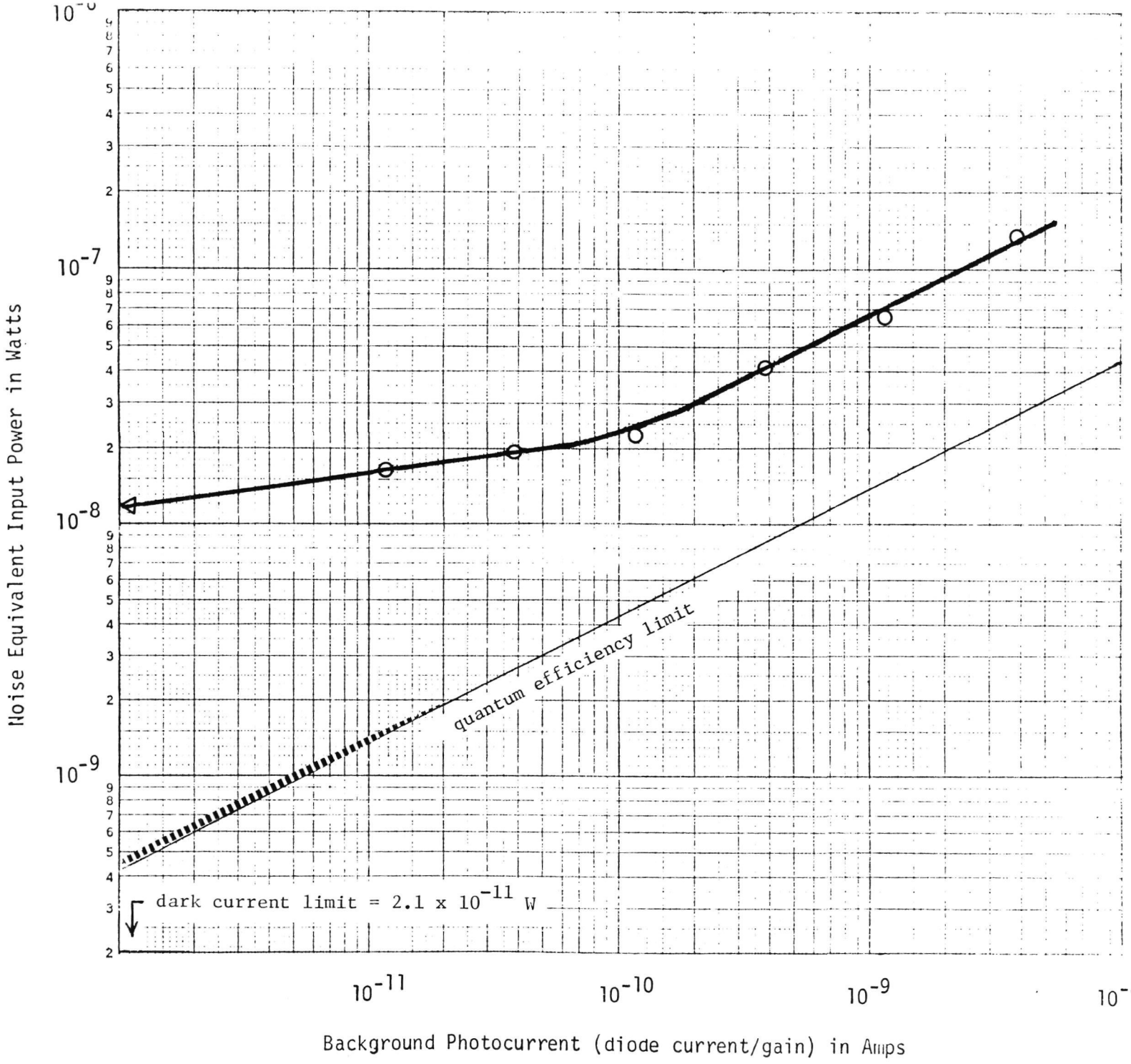

FIGURE 95 VPM 152A S/N 035 NEIP VERSUS BACKGROUND PHOTOCURRENT